

High Pressure NMR -
Single Crystal NMR Investigations
of the High Temperature Superconductor
 $\text{YBa}_2\text{Cu}_3\text{O}_{6+y}$ under Pressure

VON DER FAKULTÄT FÜR PHYSIK UND GEOWISSENSCHAFTEN
DER UNIVERSITÄT LEIPZIG

GENEHMIGTE
DISSERTATION

ZUR ERLANGUNG DES AKADEMISCHEN GRADES
DOCTOR RERUM NATURALIUM
(DR. RER. NAT.)

VORGELEGT VON
M.Sc. CARSTEN KATTINGER
GEBOREN AM 31.05.1990 IN STUTGART

Gutachter:
Prof. Dr. Jürgen Haase
Prof. Dr. Patricia L. Alireza

Tag der Verleihung Leipzig, 19. September 2022

Dedikation

DIESE DISSERTATION IST MEINEN ELTERN BEATRIX UND HERBERT GEWIDMET, DA IHR IMMER AN MICH GLAUBT, MICH UNTERSTÜTZT UND DAMIT DIESE ARBEIT ERMÖGLICHT HABT. IHR SEID FÜR MICH IMMER EIN VORBILD, DAFÜR WAS MAN SCHAFFEN KANN, WENN MAN ES NUR WILL.

CURRICULUM VITAE:

Schulbildung:

- 1996-2000 Grundschule, Jakobschule in Stuttgart
- 2000-2006 Fritz-Leonhard-Realschule in Stuttgart Degerloch
- 2006-2009 Technisches Gymnasium, Max-Eyth-Schule in Stuttgart
allgemeinem Hochschulreife, Schwerpunkt Elektrotechnik und Maschinenbau

Zivildienst:

- 2009-2010 Zivildienst im Katharinenhospital in Stuttgart
Interventionelle-Neuro-Radiologie

Bachelor Studium:

- 2010-2015 Bachelor Studium
- April 2015 Abschluss als Bachelor of Science Physik
Bachelorarbeit an der Universität Stuttgart,
5.Physikalisches Institut, Prof. Dr. Tilman Pfau
"Evanescent Atomic Vapor Spectroscopy"

Master Studium:

- 2015-2016 Beginn des Master of Science in Physik an der Universität Stuttgart
- April 2016 Umzug nach Leipzig und Wechsel der Universität
- Juli 2018 Abschluss als Master of Science (Bewertung "1.9")
Masterarbeit an der Universität Leipzig,
Felix-Bloch-Institut, Prof. Dr. Jürgen Haase
"High Pressure NMR Cell, Measurement on aluminium and properties of the Gasket"

Promotion:

- seit August 2018 Promotion an der Universität Leipzig ,
Felix-Bloch-Institut, Prof. Dr. Jürgen Haase
"High Pressure NMR - Single Crystal NMR Investigations of the High-Temperature-Superconductor $YBa_2Cu_3O_{6+y}$ "

Persönliche Daten:

Name: Carsten Kattinger
Adresse: Erdmannstraße 10, 04229 Leipzig
E-Mail: Carsten.Kattinger@Outlook.de
Geb. Datum: 31.05.1990 in Stuttgart

Publikationen:

Carsten Kattinger, Robin Guehne, Stefan Tsankov, Michael Jurkutat, Andreas Erb, and Juergen Haase, *Moissanite anvil cell single crystal NMR at pressures of up to 4.4 GPa*, Review of Scientific Instruments 92, 113901, (2021)
<https://doi.org/10.1063/5.0065736>

Michael Jurkutat, Carsten Kattinger, Stefan Tsankov, Richard Reznicek, Andreas Erb and Jürgen Haase, *How pressure enhances the critical temperature for high temperature superconductivity in $YBa_2Cu_3O_{6+y}$* , arXiv cond-mat.supr-con 2109.10157, (2021), (under review)
<https://arxiv.org/abs/2109.10157>

Robin Guehne, Carsten Kattinger, Marko Bertmer, Simon Welzmler, Oliver Oeckler and Jürgen Haase, *NMR study of $AgInTe_2$ at normal and high pressure*, arXiv cond-mat., 2201.13116, (2022), (under review)
<https://arxiv.org/abs/2201.13116>

Selbständigkeitserklärung:

Die hier vorliegende Arbeit wurde in der Zeit der Anstellung am Insitut für Experimentelle Physik II, dem Felix-Bloch-Institut an der Universität Leipzig vom 01.08.2018 - 31.10.2021, unter der Betreuung von Prof. Dr. Jürgen Haase, angefertigt.

Hiermit erkläre ich, dass die vorliegende Dissertation selbständig und ohne unerlaubte fremde Hilfe angefertigt wurde. Sämtlichen genutzten und zitierten Quellen sind nach bestem Wissen und Gewissen kenntlich gemacht und im Literaturverzeichnis aufgeführt. Alle Grafiken und Materialien an denen auch andere Mitarbeiter bei der Ideengebung und oder Schaffung beteiligen waren sind als diese gekennzeichnet. Von folgenden Personen wurde bei der Auswahl und Auswertung des Material so wie bei der Herstellung des Manuskripts Unterstützungsleistungen erhalten: Dr. Michael Jurkutat, Dr. Robin Gühne, Stefan Tsankov. Es waren keine weiteren Person bei der geistigen Herstellung der vorliegenden Arbeit beteiligt. Es wurde keine Leistung eines Promotionsberaters, oder sonstige geldwert Leistungen für Arbeiten die im Zusammenhang mit dem Inhalt der vorgelegten Dissertation stehen, in Anspruch genommen. Weder im Inland noch im Ausland wurde die vorgelegte Arbeit, oder Teile daraus, in gleicher oder ähnlicher Form, einer anderen Prüfungsbehörde, zum Zweck einer Promotion oder eines anderen Prüfungsverfahrens, vorgelegt. Es haben zuvor keine Promotionsversuche statt gefunden.

Unterschrift

Leipzig, den October 18, 2022

REFERAT

In dieser Arbeit wurde die Kupferoxidebene des Hochtemperatur - Supraleiters Yttrium-Barium-Kupferoxid ($\text{YBa}_2\text{Cu}_3\text{O}_{6+y}$) mit Hilfe von Kernmagnetischer-Resonanz (NMR - nucleus magnetic resonance) unter Drücken von bis zu 4.4 GPa untersucht. Es wurden 2 dieser Druckzellen gebaut, sie enthielten verschieden stark dotierte Einkristalle. Die Änderungen der Ladungsverteilungen in der Kupferoxidebene abhängig von der Dotierung und vom Druck lagen hierbei im Fokus der Untersuchungen.

Motivation dieser Arbeit war es $\text{YBa}_2\text{Cu}_3\text{O}_{6+y}$ Einkristalle bei höheren Drücken als zuvor mit NMR zu untersuchen. Dabei wurde der alte Rekord von 1.8 GPa (Steven Reichardt 2018) auf 4.4 GPa erhöht (aktuelle Arbeit).

Da sich die Probenkammer in einer Druckzelle stark verformt, muss die Unversehrtheit der Kristalle an jedem Druckpunkt überprüft werden. Dies wurde unter anderem mit Bildern, welche mit dem Mikroskop durch die transparenten Anvils gemacht wurden, überprüft, als auch durch aufwendige Höhenmessungen der Probenkammer mit speziellen Mikroskopen in Verbindung mit einem Piezo-gesteuertem Probenstisch. Durch die exakte Vermessung und Positionierung der Einkristalle auf dem Anvil konnte in Verbindung mit den Höhen- und Durchmesser-messungen sichergestellt werden, dass sich der Kristall unter hydrostatischen Druckbedingungen befindet und nicht linear entlang der Zellenachse komprimiert wird, was zu einem Brechen oder einer Veränderung der Orientierung führen könnte. Eine allgemeine Erkenntnis konnte dabei gewonnen werden, über die Stabilität, insbesondere der Höhe der Probenkammer, welche zunimmt mit dem Durchmesser des Culets. Dies ist entgegen des allgemeinen Prinzipes der Miniaturisierung zum Erreichen höherer Drücke, für die Planung der Zellenarchitektur für Einkristallmessungen in NMR-Anvilzellen aber wichtig.

Weiterhin mussten auch andere wichtige Parameter für NMR Messungen erfüllt werden. Die Architektur der Mikrospule welche in der Probenkammer um den Kristall gelegt wurde, mussten um den Füllfaktor zu maximieren an die Dimensionen der Kristalls angepasst werden. Dazu wurde eine Methode entwickelt um elliptische Mikrospulen von Hand zu wickeln, darin wurden die flachen Kristalle aufrecht platziert. Damit konnte das Signal auf eine annehmbare Intensität gebracht werden um in endlicher Zeit Messungen realisieren zu können. Mit den Messungen an Yttrium-Barium-Kupferoxid Einkristallen unter Druck konnte gezeigt werden, dass mit steigendem Druck sowohl die zunehmende Dotierung der Kupferoxidebene die Position am Sauerstoffatom bevorzugt, als auch eine Ladungsumverteilung in der Kupferoxidebene induziert wird.

Weiterhin wurden NMR-Messungen am Indium Kern des Thermoelektrika Silber-Indium-Tellurid unter Druck durchgeführt. 5 verschiedenen Druckzellen wurden gebaut und bei Drücken bis zu 10 GPa wurde gemessen. Bis 2.5 GPa konnten Spektren aufgezeichnet werden die einen Anstieg des elektrischen Feldgradienten nahelegten. Dieser Anstieg konnte mit Nutationsexperimenten bestätigt werden. Die Echo-Experimente bei 4 GPa und 5 GPa wiesen einen starken Signalverlust auf und legten eine Quadropolaufspaltung des Zentralübergangs zweiter Ordnung nahe. Über 5 GPa wurde kein Signal mehr gefunden. Nach dem Ablassen des Drucks zurück zu Umgebungsbedingungen wurde wieder ein Signal bei der ursprünglichen Frequenz gemessen.

ABSTRACT

In this work the CuO_2 -plane of the high temperature superconductor yttrium-barium-copper-oxide ($\text{YBa}_2\text{Cu}_3\text{O}_{6+y}$) is investigated by nuclear magnetic resonance (NMR) under pressures up to 4.4 GPa. Two high pressure NMR cells were built and filled with differently doped single crystals. The changes of the charge distribution in the CuO_2 - plane depending on doping and depending on pressure were the focus of the investigations.

The motivation of this work was to extend the NMR measurements of $\text{YBa}_2\text{Cu}_3\text{O}_{6+y}$ single crystals in NMR anvil cells with pressures not achieved before. The old record (from Steven Reichardt 2018) of $\text{YBa}_2\text{Cu}_3\text{O}_{6+y}$ single crystals up to 1.8 GPa was increased to 4.4 GPa with this work.

Due to the large deformation of the sample chamber, the integrity of a single crystal has to be checked at every pressure point. This was done by pictures, shot through the transparent anvils as well as height measurements of the sample chamber with a special microscope combined with a piezo controlled table. The exact measurements of the position of the single crystals as well as the height and diameter measurements assured that the single crystal is still in hydrostatic conditions or if it is tilted or pressurized linearly. A general cognizance about the stability of the sample chamber was acquired, especially about the stability of the height, which increases with the diameter of the culet. This is contrary to the general principle of miniaturization to reach higher pressures, if single crystals are of interest. The aim here is to have a stable sample chamber for good measuring conditions for NMR under pressure. Further, other expectations for the parameters of a NMR experiment had to be fulfilled as well. The architecture of a microcoil, which is placed around the crystal in the chamber, had to match the flat crystal shape to increase the filling factor and with this the signal to noise ratio (SNR) of the probe. For this, a method to wind elliptical micro coils by hand under the microscope was developed. Thereby signal intensity could be increased to an acceptable value which allowed more rapid measurements.

With the measurements on $\text{YBa}_2\text{Cu}_3\text{O}_{6+y}$ single crystals under pressure it was shown that increasing pressure increase the hole doping in the CuO_2 -plane. Furthermore a redistribution of the charges in the CuO_2 -plane occurs.

In a second part of this thesis ^{115}In NMR measurements on the thermoelectric AgInTe_2 under pressure up to 10 GPa in 5 different cells were performed.

Up to 2.5 GPa spectra were recorded which could be explained by an increase of the quadrupole frequency. This increase was verified by a power dependent nutation spectroscopy experiment. The echo experiments of pressures between 3 GPa and 5 GPa showed a high signal loss and pointed to an increasing disorder and a second order affected central transition of a powder spectrum. No signal was found above 5 GPa despite elaborate searches in particular for a possible metallic component. After the pressure release a signal was found again at ambient conditions frequency.

Contents

CURRICULUM VITAE:	i
REFERAT	iv
ABSTRACT	vi
0 INTRODUCTION	1
0.1 Introduction	2
0.2 Motivation	3
1 THEORETICAL BASICS	5
1.1 Nuclear Magnetic Resonance (NMR)	6
1.1.1 Quantum Mechanical Description of Spin States	6
1.1.2 Perturbation of the Hamiltonian	7
Dipolar Coupling: \mathcal{H}_D	7
Magnetic Hyperfine Coupling: \mathcal{H}_{HF}	8
Quadrupolar Coupling: \mathcal{H}_Q	8
1.1.3 Occupation of Spin States and Curie Temperature	9
1.1.4 Excitation and Relaxation	10
1.1.5 Bloch Equation, T1 und T2	11
1.1.6 Free induction decay(FID):	12
1.1.7 Nutation experiment:	12
1.1.8 Nutations Spectroscopy:	13
1.2 NMR Setup	14
1.2.1 microcoil	15
Noise and Signal to Noise Ratio	16
1.3 Pressure as Parameter	17
1.3.1 State of the Art, History of Technical Realization	18
1.3.2 Diamond Anvil Cell	19
1.3.3 Basic Architecture	20
Outer Structure, Cell Bodies	21
Inner Structure	22
1.3.4 Theory of the Gasket	23
Working Regime For Single Crystals	25
1.3.5 Pressure Medium	25
Compressability of Liquids	26
1.3.6 Measure the Pressure	27

1.4	NMR under Pressure	28
1.4.1	High Pressure NMR and State of the Art	28
1.4.2	Effects of Pressure to a NMR Experiment	30
2	SAMPLES	31
2.1	Yttrium-Barium-Copper-Oxide	32
2.1.1	Discovery	32
2.1.2	Crystal Structure	33
2.1.3	Material properties, NMR	34
2.1.4	Syntheses and Oxygen Exchange	35
2.1.5	Electronic Phase diagram and Superconducting Dome dependencies	36
2.1.6	Pressure dependence of T_c	38
2.1.7	selected YBCO investigations	38
2.1.8	YBCO NMR under Pressure	40
2.2	Silver-Indium-Telluride	42
2.2.1	Material properties, NMR	42
2.2.2	Crystal Structure	42
2.2.3	Phase transitions	43
3	EXPERIMENTAL	45
3.1	Spectrometer and Magnet	46
3.2	Evaluation of the Measured Signals	46
3.3	Micro Electronics	47
3.3.1	Improvements of the Set Up	47
	Guide Pins made from Silver	47
	Grounding Plate	48
	Twisted Legs	49
3.3.2	Special Coil design	49
	Elliptical coils	49
3.3.3	New coil for the Y-6.50 cell (MC-2 Beta cell)	51
	Double wound microcoils	52
3.4	Summary of the Chapter	53
4	SAMPLE CHAMBER MONITORING FOR SINGLE CRYSTAL NMR IN HIGH PRESSURE CELLS	55
4.1	Necessity of Sample Chamber Monitoring	56
4.2	Measurements	57
4.2.1	Measure the Height of a Sample Chamber	57
4.2.2	How to measure the Diameter	59
4.2.3	Results of the height and diameter measurements	60
	Y-6.85 Cell (AlphaCell) and Y-6.5 Cell (BetaCell)	60
4.2.4	Volume Determination, Compressability of Parafin Oil	63

4.3	error consideration	64
4.4	Discussion	65
5	SINGLE CRYSTAL NMR OF $\text{YBa}_2\text{Cu}_3\text{O}_{6+y}$ UP TO 4.4 GPa	67
5.1	Doping Level and the Critical Temperature	68
5.1.1	T_c measurement	68
	Y-6.85 (MC-2 Alpha cell)	70
	Y-6.50 (MC-2 Beta cell)	71
5.1.2	Comparison to the Literature	72
5.2	Orientation of the Single Crystal	73
5.2.1	Quadrupole Frequencies pressure dependency	75
5.2.2	Charges in the CuO_2 -plane under Pressure	77
5.3	Discussion	81
6	SILVER-INDIUM-TELLURIDE NMR UNDER PRESSURE	83
6.1	Introduction	84
6.2	Sample	85
6.3	Pressures Cells	85
6.3.1	Signal to Noise Ratio	86
6.4	Measurments	87
6.4.1	FID of Silver-Indium-Telluride at 11.7 T	87
6.4.2	Spectrum	88
6.4.3	Nutation Spectroscopy	90
6.4.4	Second Order Effect and Signal Loss Above 5GPa	93
6.4.5	T_1 measurements	95
6.4.6	Shifts	96
6.5	Discussion	97
7	SUMMARY AND OUTLOOK	99
7.1	Summary	100
7.1.1	Sample Chamber Monitoring for Single Crystal NMR	100
7.1.2	Single Crystal NMR of $\text{YBa}_2\text{Cu}_3\text{O}_{6+y}$ up to 4.4 GPa	101
7.1.3	Silver-Indium-Tellurid NMR Under Pressure	102
7.2	Conclusion and Outlook	103
	APPENDIX A APPENDIX	107
A.1	Spectra	108
	Y-6.85 Cell	108
	Y-6.5 Cell	113
	REFERENCES	127

Listing of figures

1.1	Energetic States Scheme	7
1.2	NMR circuit	14
1.3	Anvil Cell Structure	19
1.4	Leipzig Anvil Cells (LAC)	20
1.5	Used LAC cells	21
1.6	NMR Anvil Cell Inner Structure	22
1.7	Theory of the Gasket	24
2.1	YBCO Crystal structure	33
2.2	Doping dependent Phase diagram	36
2.3	T_c -dependence domes	37
2.4	NMR Phase diagram of selected cuprates	39
2.5	Closing the Pseudogap	40
2.6	AgInTe Crystal structure	43
3.1	Picture of the grounding plate	48
3.2	Coils with twisted legs	49
3.3	Pictures of the preparation of elliptical coil	50
3.4	Cylindrical coil vs. elliptical coil	51
3.5	Double wound coils	52
4.1	Crystal between two anvils	56
4.2	Reference edges of an anvil	57
4.3	Concept of height measurements	58
4.4	Pictures of the anvils under the microscope	59
4.5	Height and radius measurements	60
4.6	$(r_0 - r_g(p))/h(p)$, cell parameters depending on pressure	61
4.7	Volume of Y-6.85 cell and Y-6.50 cell	63
5.1	Temperature response of the circuit	68
5.2	Derivative of the temperature dependent center frequency Y-6.85	70
5.3	Derivative of the temperature dependent center frequency Y-6.5	71
5.4	Pressure dependence of the critical temperature	72
5.5	Sketch of the crystal on the culet surface	73
5.6	Orientation dependency of the ^{63}Cu Central transition	74
5.7	Quadrupole frequencies, pressure dependency	75
5.8	Planar Charges	77
5.9	Movements in the $2n_{\text{O}}-n_{\text{Cu}}$ -plane	79

5.10	$2n_{\text{O}}-n_{\text{Cu}}$ -plane	80
6.1	Picture of a cross cell	85
6.2	Spectra of AgInTe_2 ; ambient	87
6.3	Spectra of AgInTe_2 , pressure dependent	88
6.4	Indium nutation spectroscopy, pressure dependent	90
6.5	Indium spectrum at 4 GPa with simulation	93
6.6	Second order affected spectra of AgInTe_2	94
6.7	T_1 measurement of Indium, pressure dependent	95
6.8	Shifts of AgInTe_2 , pressure dependent	96
A.1	Oxygen spectrum ^{17}O , ab $\parallel B_0$ at ambient conditions	108
A.2	Oxygen spectrum ^{17}O , ab $\parallel B_0$ at 28 kBar	108
A.3	Oxygen spectrum ^{17}O , ab $\parallel B_0$ at 44 kBar	109
A.4	Oxygen spectrum ^{17}O , c $\parallel B_0$ at ambient conditions	109
A.5	Oxygen spectrum ^{17}O , c $\parallel B_0$ at 28 kBar	110
A.6	Oxygen spectrum ^{17}O , c $\parallel B_0$ at 44 kBar	110
A.7	Oxygen spectrum ^{17}O , c $\parallel B_0$ temperature dependence	111
A.8	Copper spectrum ^{63}Cu , c $\parallel B_0$ at various pressures	112
A.9	Oxygen spectrum, c B ambient conditions	113
A.10	Oxygen spectrum, c $\parallel B_0$ at 4 kBar	113

“The task is not to see what has never been seen before, but to think what has never been thought before about what you see everyday.”

Erwin Schrödinger

0

Introduction

In this dissertation, at the front page of every chapter, a short text about the content and structure is given.

This first chapter is an introduction to the field in physics of this dissertation, further the motivation for this work is formulated.

0.1 INTRODUCTION

High Pressure NMR is a powerful probe for all phenomena that also influence the interactions of a bulk of nuclei under pressure¹. The change of the strength of the different interactions of the nuclei can give us information about the nucleus surrounding and with this about the interactions in the crystal structure. Pressure can change the surrounding, for example, very weakly by changing the nuclear distances by compression, or enormously, by changing the crystal structure by a phase transition. The interaction between the nuclei and the surrounding electrons can give us information about the band structure and the density of states.²

The used high pressure NMR technique, based on a microcoil in the sample chamber of an anvil cell was realized in 2009 by P. Alireza³ from the Cambridge University in cooperation with the University of Leipzig, where the NMR measurements were made.

Till today, different types of anvil cells are invented and designed in Leipzig⁴. Which allowed NMR measurements at different powdered samples under pressures up to 20.2 GPa⁵. As gasket material, copper-beryllium (CuBe) was used, due to its low magnetic susceptibility and high strength.

For the investigation of Yttrium-Barium-Copper-Oxid ($\text{YBa}_2\text{Cu}_3\text{O}_{6+y}$) single crystals under pressure, a specialized set up was needed. Steven Reichardt⁶ put a micro crystal on the top of an anvil and fixed it with epoxy resin. The gasket and the microcoil was added, the chamber was filled with paraffin oil and closed. The orientation of the crystal in the B field was done by the observable resonance frequency dependence of the central transition of the copper nuclei due to second order quadrupole effects.

Small crystals give small signal of course but it was possible to depict the whole copper and oxygen spectra at pressures up to 1.8 GPa⁶.

The biggest problem for a single crystal in an anvil cell is the deformation of the sample chamber while pressure is increased. The single crystal is considered to be in hydrostatic conditions as long the height of the sample chamber is higher then the crystal height and the limits for the pressure medium, in this case paraffin oil, are fulfilled. From the point when the height of the sample chamber goes below the height of the crystal, the crystal is squeezed along the cell's z-axis, changes it's alignment or is even broken. To solve these problems and realize the measurements at higher pressures then before was a central part of this work.

0.2 MOTIVATION

The pressure phenomenology of the high temperature superconductors was investigated with different methods^{7,8}. But the open questions about the effect of pressure to the charge distribution in the CuO_2 -plane remained unanswered in the past. NMR as method allows a qualitative measurement of these charges, but high pressure combined with NMR is a very challenging task. The fact that the signal intensity depends on the number of nuclei in the receiver coil and the idea of a miniaturization of the setup to increase the pressure oppose each other. A compromise had to be found. The setup with a microcoil inside the sample chamber increases the signal strength but also set limits due to the deformation of the chamber.

The first attempt, which provided a full set of data of a micro single crystal of $\text{YBa}_2\text{Cu}_3\text{O}_{6+y}$ under pressure by Steven Reichardt^{9,6} unfortunately reached only 1.8 GPa. The connection wire to the coil broke when they compressed it further.

The motivation of this work is to extend the achievable pressures for $\text{YBa}_2\text{Cu}_3\text{O}_{6+y}$ single crystals NMR investigation with the used high pressure NMR anvil cell. The limit is set by the deformation of chamber, or more precise by the height decrease. The anvil cell could break the single crystal if the height reduction of the sample chamber is to large. To reach higher pressures and make these investigations possible, a technique for the observation of the live sample chambers dimensions at every pressure was needed. Different approaches were considered, the most promising, based on the relative comparison of two marked references on the anvils was realized.

The signal intensity of such a small single crystal is challenging. To optimize the Signal different ideas of coil architectures and changes at the cells were tested.

My motivation for this work was the challenging mixture of 2 experimental techniques, the complex electronically NMR setup and especially the micro electronics of a NMR anvil cell, soldered and build by hand under a microscope, combined with not clear theoretical approaches to the very interesting field of cuprate superconductivity.

“Quantum theory provides us with a striking illustration of the fact that we can fully understand a connection though we can only speak of it in images and parables.”

Werner Heisenberg

1

Theoretical Basics

This chapter is written to repeat some theoretical aspects need for this thesis.

First, an introduction to nuclear magnetic resonance (NMR) is presented, followed by the used NMR and microcoil setup. Then the parameter pressure is introduced and discussed. How to achieve such conditions as well as which influence on experiments it can have. A state of the art is given here. Further the deformation of the gasket is described theoretically. A second state of the art focusing on NMR under pressure is given in this chapter as well.

1.1 NUCLEAR MAGNETIC RESONANCE (NMR)

A short conclusion of the relevant basics of nuclear magnetic resonance (NMR) is presented here, based on the books from C.P. Slichter², from D. Freude and J. Haase¹⁰ as well as other important books^{11,12,13}

1.1.1 QUANTUM MECHANICAL DESCRIPTION OF SPIN STATES

The quantum mechanical vector operator \mathbf{I} describes the angular momentum I of the nucleus. The vector operator \mathbf{I} can be written in cartesian coordinates with it's components $\hat{I}_{x,y,z}$, which are operators as well. \mathbf{I}^2 commutates with \hat{I}_z . The common set of eigenvectors $|Im\rangle$ gives the corresponding eigenvalues:

$$\mathbf{I}^2 |Im\rangle = I(I + 1) |Im\rangle \quad \text{and} \quad \hat{I}_z |Im\rangle = m |Im\rangle \quad (1.1)$$

with $I = 0, \frac{1}{2}, 1, \frac{3}{2}, 2, \dots$ and $m = -I, -I + 1, \dots, 0, \dots, I - 1, I$.

The interaction of the magnetic moment of the nucleus with an external magnetic field can be described by the Zeeman Hamiltonian:

$$\mathcal{H}_Z = -\boldsymbol{\mu}\mathbf{B} = -\hbar\gamma\mathbf{I}\mathbf{B} \quad (1.2)$$

$\boldsymbol{\mu} = \hbar\gamma\mathbf{I}$ is the magnetic moment of the nucleus, γ is the isotope specific gyro magnetic ratio.

By assuming the static B_0 field exclusive in z-direction, $\mathbf{B} = (0,0,B_0)$, the Hamiltonian can be simplified to $\mathcal{H}_Z = -\hbar\gamma B_0 I_z$. The eigenvalues are given by $E_m = -m\hbar\gamma B_0$. While $\Delta E = \hbar\gamma B_0$ gives the energy difference between the states. The spin precesses in the B_0 field with the Larmor frequency $\omega_{Larmor} = \omega_L = \gamma B$, which is the resonance condition for the excitation of a transition between the states. A energetic scheme proportional to ω is presented in Fig. 1.1.

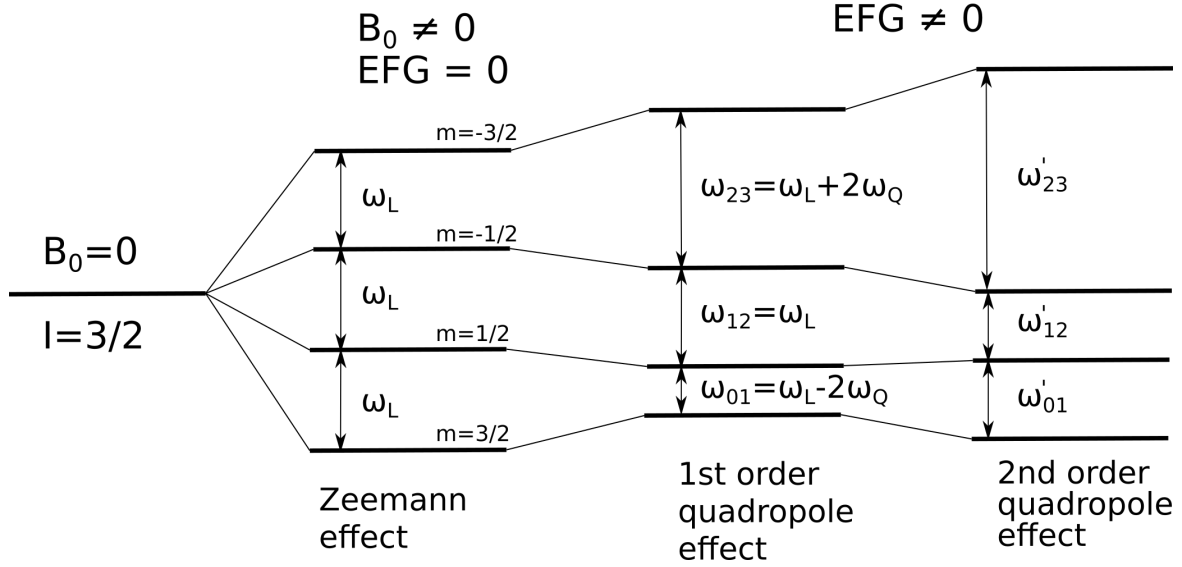


Figure 1.1: **Energetic States Scheme:** A energetic scheme is presented here for the Zeeman interaction as well as for quadrupole interaction of first and second order of a nucleus with $I = 3/2$

1.1.2 PERTUBATION OF THE HAMILTONIAN

We are interested in a dominating Zeeman Hamiltonian. Other interactions are considered as perturbations of \mathcal{H}_z . Some important interaction for this thesis are discussed below:

DIPOLAR COUPLING: \mathcal{H}_D

Dipolar coupling describes the interaction between two magnetic moments of two nuclear spins $\boldsymbol{\mu}_1 = \gamma_1 \hbar \mathbf{I}_1$ and $\boldsymbol{\mu}_2 = \gamma_2 \hbar \mathbf{I}_2$ with a distance of r .

$$\mathcal{H}_D = \gamma_1 \gamma_2 \hbar^2 \mathbf{I}_1 \left[\frac{\mathbf{I}_2}{r^3} - 3 \frac{r(\mathbf{I}_2 r)}{r^5} \right] \quad (1.3)$$

The dipolar coupling causes a B_0 independent broadening of the resonance lines.

MAGNETIC HYPERFINE COUPLING: \mathcal{H}_{HF}

This coupling describes the magnetic interactions of the nuclear spin with the surrounding electrons. There are different contributions in the magnetic hyperfine Hamiltonian

$$\mathcal{H}_{HF} = 2\gamma\hbar\mu_B\mathbf{I} \left[\frac{\hat{l}}{r^3} - \frac{\hat{s}}{r^3} + 3\frac{r(r\hat{s})}{r^5} + \frac{8}{3}\pi\hat{s}\delta(r) \right] \quad (1.4)$$

μ_B is the Bohr magneton, \hat{l} is the orbital and \hat{s} is the spin angular momentum operators of the electron.

The surrounding electrons change the local magnetic field at the nucleus, which causes a difference between the Lamor frequency ν_L of the undisturbed nuclei and measured resonance frequency ν_0 of the hyperfine coupled nucleus in a lattice.

QUADRUPOLE COUPLING: \mathcal{H}_Q

If $I \geq 1$ the electronic hyperfine coupling has to be considered. The interaction between the quadrupole moment Q and the electric field gradient (EFG) causes a energetically difference between the energy levels which causes a spitting of the resonance lines.

The Hamiltonian can be described as followed. (X, Y, Z give the principle axes of the tensor V_{ij} describing the EFG if $|V_{ZZ}| \geq |V_{YY}| \geq |V_{XX}|$)

$$\mathcal{H}_Q = \frac{e^2qQ}{4I(2I-1)} \left[3I_Z^2 - I(I+1) + \frac{1}{2}\eta(I_+^2 + I_-^2) \right] \quad (1.5)$$

the asymmetry parameter $\eta = (V_{XX} - V_{YY})/(V_{ZZ})$ can take the values between 0 and 1 ($\eta \in [0,1]$). Further, the ladder operators are given as $I_{\pm} = I_x \pm iI_y$.

In this work the application of this formula will be limited to the case of $\mathcal{H}_Q \ll \mathcal{H}_Z$ further only half integer spins are investigated. Copper ^{63,65}Cu with a spin of 3/2, Oxygen ¹⁷O with a spin of 5/2 and ^{113,115}In with a spin of 9/2.

The quadrupole frequency ν_Q is given by

$$\nu_Q = \frac{3e^2qQ}{2I(2I-1)h} \quad (1.6)$$

The formula¹⁰ for the orientation dependency of the ^{63}Cu central transition affected by second order effects used in sec. 5.2 for the fit in Fig. 5.6 is given here:

$$\nu_{-1/2,1/2} - \nu_L = \frac{\nu_Q^2}{6\nu_L} \left[I(I+1) - \frac{3}{4} \right] \left[\frac{1}{5} \left(1 + \frac{\eta^2}{3} + g(\alpha, \beta, \eta) \right) \right] \quad (1.7)$$

$\nu_{-1/2,1/2}$ is the transition frequency, ν_L is the Larmor frequency, ν_Q is the quadrupole frequency, I the spin quantum number, $g(\alpha, \beta, \eta)$ is the orientation term, dependent on the alpha and beta angles as well as the symmetry of the EFG. A detailed description of all terms is given in the literature¹⁰.

1.1.3 OCCUPATION OF SPIN STATES AND CURIE TEMPERATURE

A macroscopic magnetization of a sample is given by a sum over all quantum mechanic magnetic moments in their stationary spin states per volume V .

$$\vec{M}_0 = \sum_i^N \frac{\vec{\mu}_i}{V} \quad (1.8)$$

where \vec{M}_0 is the magnetization of the sample, i is the number of the specific moment $\vec{\mu}_i$, N is the total number of the moments.

The net magnetization $\langle M_z \rangle$ along the external B_0 field is a result of the slightly unbalance of parallel and anti parallel contributions of the states, due to occupation differences. The magnetization at the temperature T is given by the Curie law:

$$\langle M_z \rangle = \frac{N\gamma\hbar^2 I(I+1)}{3k_B T V} B_0 \quad (1.9)$$

The Boltzmann distribution can describe the population p_m , in the level with the energy E_m , while $p_m \propto \exp\left(\frac{-E_m}{k_B T}\right)$. The ratio $\frac{p_{m+1}}{p_m}$ gives the difference relation of the populations of two neighboring states depending on the temperature in thermal equilibrium, if the high temperature approximation ($k_B T \gg \gamma\hbar B_0$) is fulfilled.

$$\frac{p_{m+1}}{p_m} = \exp\left(\frac{\gamma\hbar B_0}{k_B T}\right) \quad (1.10)$$

A change of this magnetization needs an external manipulation, from RF pulses, after which it relaxes.

1.1.4 EXCITATION AND RELAXATION

The B_1 field of the excitation coil must have an alignment which is not parallel or anti parallel to the external B_0 field. The ideal orientation for excitation includes a right angle between B_0 and B_1 . B_1 can be calculated by the following formula:

$$B_1 = \sqrt{\frac{\mu_0 P Q}{2\omega V_{coil}}} \quad (1.11)$$

where P is the applied power of the pulse, Q is the quality factor of the circuit, ω is the frequency of the pulse and V_{coil} is the volume of the coil.

It is possible to flip the macroscopic magnetization by an angle θ , if a radio frequency pulse (RF pulse) is applied. The angle θ is influenced by the field strength B_1 , by the gyro magnetic ratio γ of the isotope and by the time τ of the pulse.

$$\theta = \gamma B_1 \tau = \gamma \tau \sqrt{\frac{\mu_0 P Q}{2\omega V_{coil}}} \quad (1.12)$$

The most interesting angles are of course π and $\pi/2$. By setting an angle the time can be estimated:

$$\tau_{\pi/2} = \frac{\pi}{\gamma} \sqrt{\frac{\omega V_{coil}}{2\mu_0 P Q}} \quad (1.13)$$

While B_1 is applied on resonance the spins nutate around the axis of the coil's B field. After the excitation with an $\pi/2$ pulse the magnetization precesses in the \hat{x} - \hat{y} -plane. A precessing magnetic moment in a coil leads to Faraday Induction. So the same coil can be used for the excitation and for the detection of the signal. After the excitation spins decay back to the thermal equilibrium. This can be described macroscopic by the Bloch equations.

1.1.5 BLOCH EQUATION, T1 UND T2

Felix Bloch published in 1946 the so called Bloch equations. These equations are a set of differential equations which describe the magnetization vector \vec{M} in the 3 dimensional space. This vector describes classically the change of the magnetization by time if its deflected from the alignment in an external B field.

$$\frac{d\vec{M}}{dt} = \gamma(\vec{M} \times \vec{B}_0) - \frac{M_x\hat{x} + M_y\hat{y}}{T_2} - \frac{(M_z - M_0)\hat{z}}{T_1} \quad (1.14)$$

The magnetic field \vec{B}_0 causes an angular momentum to the magnetization $\gamma(\vec{M} \times \vec{B}_0)$. The second and the third parts $(\frac{M_x\hat{x} + M_y\hat{y}}{T_2}, \frac{(M_z - M_0)\hat{z}}{T_1})$ are responsible for the exponential decay of the magnetization by time. T_1 and T_2 are the exponential decay coefficients. If $\vec{B}_0 \parallel \hat{z}$, T_1 describes the decay of the \hat{z} -component of the magnetization, while T_2 describes the decay in the \hat{x} - \hat{y} -plane.

T_1 describes the relaxation in \hat{z} -direction. It is called the longitudinal relaxation, longitudinal to the external B_0 field. Here the energetic decay is described, were the spins flip until thermal equilibrium is reached. The energy in this relaxation mode is given to the lattice, which results in a heating of the sample. Due to the small energies of these spin flips the thermal heating effects can be neglected.

T_2 describes the relaxation in the \hat{x} - \hat{y} -plane it is called the transverse relaxation. This relaxation mode is based on the phase relation of the different spins. Different interaction can contribute to this mode, for example the dipolar interaction or field inhomogeneities. In case of a pressure dependence of interactions or resonances, a pressure gradient in the chamber of the anvil cell could cause a additional dephasing. For an uniform distribution of all phases the magnetization in the \hat{x} - \hat{y} -plane decays to zero. T_2 is in general smaller then T_1 , which means the dephasing is a faster mode then the reaching of the thermal equilibrium.

1.1.6 FREE INDUCTION DECAY(FID):

The free induction decay (FID) describes the signal after a deflection of the magnetization from the alignment along the external magnetic field B_0 , by a radio frequency pulse (RF pulse). The \hat{x} - \hat{y} -components of the rotating magnetization in the coil induce the measured voltage. By using the rotating frame, which sets the perspective to the excitation/resonance frequency, the alternating part can be compensated and only an exponential decay remains.

1.1.7 NUTATION EXPERIMENT:

A nutation experiment is done to determine the $\pi/2$ pulse. It is the first experiment one checks for a new sample, based on a single pulse with the power P and the duration time τ . The formula (1.12) in sec . 1.1.4, gives the rotation angle of the macroscopic magnetization $\langle M_0 \rangle$ if a pulse is applied.

A variation of one parameter, power or time, while holding the other, allows a determination. The measured intensity in the coil will have a maximum for a $\pi/2$ pulse and decrease for larger angle again. Some systems can also be inverted or completely rotated. The nutation follows an exponentially damped *sine*-functions.

Small inhomogeneities in the surrounding of the nuclei cause small differences in the Larmor frequencies ω_L , Which leads to a small bandwidth where the pulse parameters vary. For small angles the variation of the excitation is small but for large rotation angles these small discrepancies sum up, while getting more nuclei out of phase which can not contribute to the signal anymore. This leads to a damped signal.

1.1.8 NUTATIONS SPECTROSCOPY:

The response of a solid state quadrupole spin system to a RF pulse is strongly dependent on the relation between the RF-pulse and the strength of the quadrupole coupling. The ratio ω_Q/ω_{RF} tells if the spectra is selective or non selective excited.

If $\omega_Q \ll \omega_{RF}$ the excitation is called non selective. In this case the quadrupole interaction can be neglected during the excitation and the spin system acts like a spin 1/2.

If $\omega_Q \gg \omega_{RF}$ is applied the excitation is called selective. For powders only the the central transition is accessible this way. The compare between the measured intensities and frequencies and a simulation, allows a determination of ω_Q by the variation of ω_{RF} . The relation of the intensities are given by^{10,14}:

$$I_{selective} = \frac{I_{non}}{I + 1/2} \quad (1.15)$$

while the relation of the frequencies are given by:

$$\omega_{RF,selective} = (I + 1/2)\omega_{RF,non} \quad (1.16)$$

In the case of ^{115}In , ($I = 9/2$), the relations go to $I_{selective} = I_{non}/5$ and $\omega_{RF,selective} = 5 \cdot \omega_{RF,non}$. For more details about the mathematical descriptions as well as simulations please see literature^{10,14}.

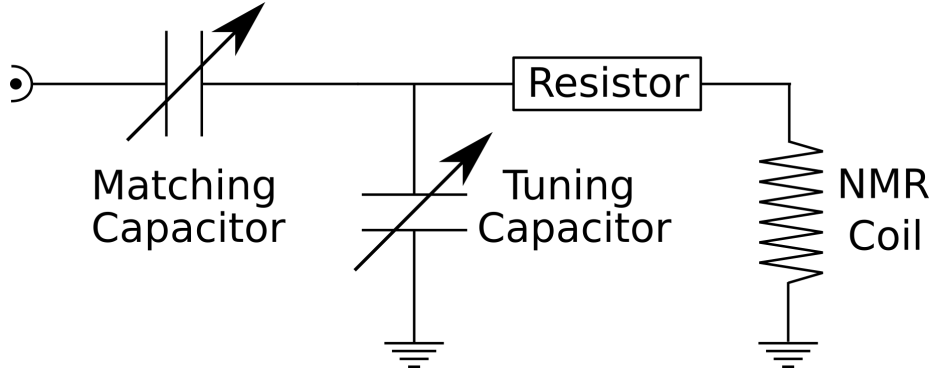


Figure 1.2: **Basic NMR circuit:** Here the basic circuit diagram is shown, the resonance frequency is set by the tuning capacitor. The matching capacitor is used to match the circuit to $Z = 50 \Omega$ to realize a signal transmission free from reflections and standing waves

1.2 NMR SETUP

A typical NMR experiment needs beside a strong static B_0 field a tune able resonance circuit. Such a circuit consists basically of an inductive element like coil with it's inductance L and a capacitive element like a capacitor with it's capacity C . The resonance frequency is then given by:

$$f = \frac{1}{\sqrt{L \cdot (C_1 + C_2)}} \quad (1.17)$$

The approach which we use for NMR experiments is based on two adjustable capacitors and a coil (see Fig 1.2). The tuning capacitor C_{tune} is used to tune the circuit to the resonance frequency and is grounded parallel to the coil. The matching capacitor is needed to match the circuits impedance Z to the 50Ω of the signal detection line to realize a signal transmission free from reflections and standing waves.

Every resonance circuit is categorized by the quality factor Q .

$$Q = 2\pi \frac{W}{V} \quad (1.18)$$

This ratio of the maximum stored energy (W) and the dissipated energy per cycle (V) of the system gives information about the damping. The energy oscillates between the magnetic field (in the coil) and the electric field (in the capacitor), the system is damped by the real part resistance of the used electrical elements and the wires, symbolized and put together as R .

Measure the Q-factor:

In the daily routine the Q-factor is measured with the help of a network analyzer. If the circuit is tuned and matched to the resonance frequency ω_0 , two frequencies are defined ω_1 and ω_2 , above and below ω_0 , as the frequency were the intensity is -7 dB damped in compare to the zero line. Q can be calculated using the followed equation:

$$Q = \frac{\omega_0}{\omega_1 - \omega_2} \quad (1.19)$$

1.2.1 MICROCOIL

It was shown in [15,16,17](#), high resolution NMR with wide line excitation of broad NMR signals is possible using a microcoil setup. The advantage to a regular sized coil is obvious. The much smaller volume of a microcoil leads to a much bigger Radio Frequency (RF) field strength:

$$B_1 = \sqrt{\frac{\mu_0 Q P}{2\omega V_{coil}}} \quad (1.20)$$

μ_0 is the vacuum permeability, Q the quality factor, P is the applied power, ω gives the resonance frequency.

The inductance of a flat solenoid microcoil, which was used in the high pressure NMR cells, can be calculated by the following formula¹⁸:

$$L[nH] = \frac{21.8N^2 d_{coil}}{1 + 2.2 \frac{l_{coil}}{d_{coil}}} \quad (1.21)$$

The number of turns of the coil is given by N , d_{coil} in $[cm]$ is the diameter and l_{coil} in $[cm]$ gives the length of the coil. This formula would be valid for an empty coil.

The inductance of a coil filled with a sample would be influenced by the susceptibility χ_m of the sample,

$$L_\rho = L(1 + \rho\chi_m) \quad (1.22)$$

with ρ as filling factor.

The relation between the magnetic susceptibility and the inductance of the coil can be used to observe the transition of a material to the superconducting state by observing the change of the inductance. If this coil is connected to a circuit the resonance frequency changes over a temperature range.

For more information about the determination of the critical temperature by this method please check sec. 5.1.1

NOISE AND SIGNAL TO NOISE RATIO

For our NMR experiments we concern mostly thermal (Johnson) noise. It was described by Nyquist^{19,20}

$$U_{noise} = \sqrt{4Rk_B T \Delta f} \quad (1.23)$$

R denotes the resistance, k_B is the Boltzmann's constant, T the temperature and Δf the frequency bandwidth. In our case we use a micro silver wire (Goodfellow Cambridge Ltd), with a diameter of $25 \mu\text{m}$ and an insulation of $5 \mu\text{m}$ to wind the coil. This coil is considered to be the main source of thermal noise.

A typical value of thermal noise voltage of a NMR cell at room temperature is $V_{thermal} = 0.23 \mu\text{V}$. The quality of a signal is described by the "Signal to Noise Ratio" (SNR)²¹.

$$SNR = \frac{P_{induced}}{P_{noise}} = \frac{U_{induced}^2}{U_{noise}^2} \quad \text{with} \quad U_{induced} = \rho N_{coil} A_{coil} \omega_0 \mu_0 M_0 \quad (1.24)$$

The induced voltage, by the nuclei in the coil can be calculated by: ρ as filling factor, N_{coil} as the winding of the coil and M_0 is the magnetization given by:

$$M_0 = \frac{N_{nuclei}}{V} \cdot \frac{\gamma_n^2 \hbar^2 I(I+1) B_0}{3k_B T} \quad (1.25)$$

Here $\frac{N_{nuclei}}{V}$ are the number of spins per volume, γ_n is the gyro magnetic ratio. Low filling factors $\rho \approx 0.1$ for microcoils containing small single crystals is assumed. A typical voltage value for the signal is around $U_{induced} \approx 2 \text{ nV}$. This leads to $SNR \ll 1$.

The repetition of a NMR experiment increases the SNR . While the $U_{induced}$ grows linear by repetition, U_{noise} grows proportional to the square root, due to the normal distribution of a random process.

1.3 PRESSURE AS PARAMETER

In this section different effects of pressure on matter are considered and discussed to get a picture of pressure as parameter in physical experiments. The description in this section goes back to the publication "The Chemical Imagination at Work in *Very Tight Places*" by W. Grochala, J. Feng, R. Hoffmann and N. Ashcroft in the year 2007²².

For microscopic application, the common definition of pressure (eq. 1.26), can be interpreted as energy per volume.

$$p = \frac{F}{A} = \frac{Energy}{Volume} \quad (1.26)$$

The consideration of pressure as energy density allows a thinking of the relations between the energy differences between the states in a system and the influence of the surrounding. While temperature changes the occupation of levels, described by the Boltzmann distribution, pressure changes the levels it's self. Four effects, which pressure can induce in solids, dependent on the length/energy scales, in order to increase the energy density, are mentioned here:

- I** The penetration of the repulsive region of inter molecular potentials (Van der Waals potential). This results in elastic and plastic deformations of the crystal shape with a large volume decrease.
- II** Electric transitions as well as phase transitions occur. The coordination is increased. This means the number of direct neighboring atoms increased by changing the structure of matter.
- III** The distance of the nuclei decreases which affects the covalent bonds. More electrons contribute to the bond, which increases the electron density. The increasing overlap of orbitals can lead to a formation of a band structure.
- IV** Strong effect on the band structure occur. By decreasing the distance further, the overlap of the orbitals increase which can lead to a decrease in the band gap. For the highest pressures the band gap is closed the density of states increase rapid, which leads to insulator metal transitions.

Of course the effects strongly depend on the individual atoms, structures and materials.

1.3.1 STATE OF THE ART, HISTORY OF TECHNICAL REALIZATION

To realize such extreme conditions technically, a lot of 'know how' about materials is needed. P.W. Bridgman²³ is known as the Inventor of the anvil cells. He developed a cell architecture of two opposed anvils and a gasket in between, which are pressed together by an outer structure that applies the force. Bridgman used tungsten carbide anvils, and measured for different materials the electric resistance and the compressibility^{23,24}, up to a few gigapascal [GPa].

The basic principle remains the same, but single crystal diamonds are used as anvils for their much higher strength, which today allows to achieve much high pressures with out breaking.

However some important developments in the field shall be referenced here:

The usage of the diamonds as anvil by C. Weir²⁵ and A.v. Valkenburg²⁶ in 1959, possible due to quality improvements of diamonds, harder materials²⁷ and further technical progress, extended the pressure range immensely up to the megabar [Mbar] regime^{28,29,30}. In 1972^{31,32} R. Forman introduced the ruby luminescence method to measure the pressure optically with a laser through the transparent anvils (see 1.3.6). Nowadays this method is extended up to 150 GPa³³. K. Goettel³⁴ and W. Moss³⁵ introduced beveled anvils as standard starting in 1985 for more stability which further increased the reachable pressures. In 2015 the record pressure of 750 GPa was measured in a DAC by L. Dubrovinsky³⁶.

One of the most impressive works in the last few years, with an eye on high pressure and superconductivity, was the work from the M. Eremets group³⁷. They showed 'Superconductivity at 250 K in lanthanum hydride under high pressures'. Lanthanum hydride LaH_{10} show superconductivity, predicted by BCS theory. High frequency phonons allow a strong electron-phonon coupling combined by the pressures induced high density of states, the superconducting state was achieved at ≈ 160 GPa³⁷. The isotope effect as well as the Meissner effect confirmed the superconductivity near room temperature.

1.3.2 DIAMOND ANVIL CELL

The basic idea of an anvil cell was introduced by P. W. Bridgman in 1905. In 1946 he received the Noble Prize in physics for his work in the field of high pressure physics, about the electric conductivity of metals and crystal structures under pressure. Bridgman used tungsten carbide anvils, a stainless steel gasket and a lever arm device to apply the force²⁴.

A lot of changes from this early approach led to the actual "Diamond Anvil Cell" (DAC) technique^{30,38,39,40,41,42}.

A "Diamond Anvil Cell" is a high pressure device, build of two opposing diamond anvils and a gasket with hole in between. To transform uniaxial pressure into hydrostatic pressure a pressure transmitting medium is needed, such as Helium, Argon, Xenon, paraffin oil or a mixture of methanol and ethanol (4:1) are common. The pressure transmitting medium is filled to the sample chamber which is created by the gasket hole and the two opposing anvils. Due to the optical transparent anvils an optical access to the chamber is possible.

The outer structure applies the force on the anvils, which focuses the force on the tip area. A miniaturization of the anvil tips, and with this the contact *Area*, follows the simple relation to increase the pressure.

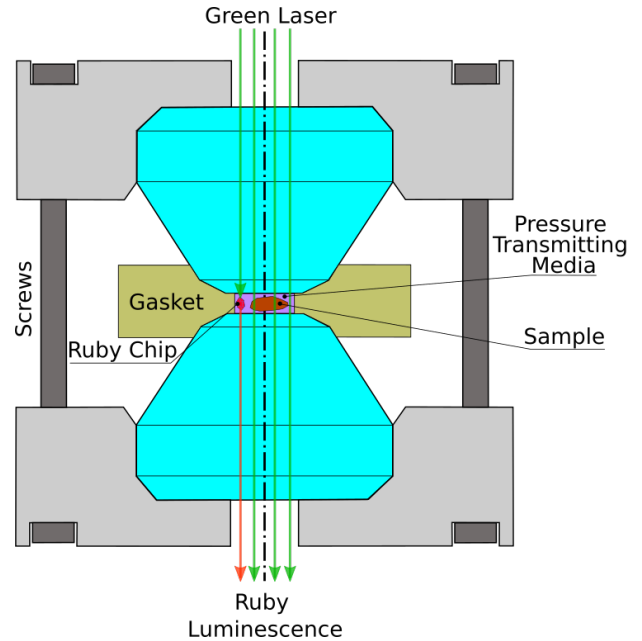


Figure 1.3: **Anvil Cell Structure:**

The basic structure of a diamond anvil cell. One can see the outer structure to apply the force on the anvils and the gasket. Between the anvils, inside the sample chamber a ruby chip and the sample is placed, surrounded by a pressure transmitting media

1.3.3 BASIC ARCHITECTURE

In 2003 P. Alireza⁴³ build a cell containing a microcoil inside the pressure chamber to do susceptibility measurements under pressure. This approach was used by T. Meissner³ et. al. to do high pressure NMR experiments in Leipzig in 2009. Later a serial of "Leipzig Anvil Cells" (LAC) were designed by T. Meier^{4,44}. The detailed manual for the preparation of a NMR anvil cell is given else were⁴⁵. In this thesis only moissanite (6H-SiC)⁴⁶ anvils, and for the gasket copper beryllium (CuBe, alloy 25^{47,48}), was used.



Figure 1.4: **Leipzig Anvil Cells (LAC):** This picture of the Leipzig Anvil Cells was taken and published by T. Meier for his thesis⁴⁴ in Leipzig between 2010 and 2016

In this actual work the LAC-TM1 and LAC-TM2 designs were used for NMR measurements under pressure.

In general a DAC consist of three main components: the piston, the shell and a movable backing plate. The piston is the movable part in the set up and holds an anvil. The shell holds the other anvil and is important to guide and stabilize the piston while pressure is applied. Pressing the piston in the shell presses the anvils together and generates between the tips of the anvils the aimed extreme conditions. The movable backing plate is located in the shell to be able to align the shell's anvil in respect to the piston anvil.

OUTER STRUCTURE, CELL BODIES

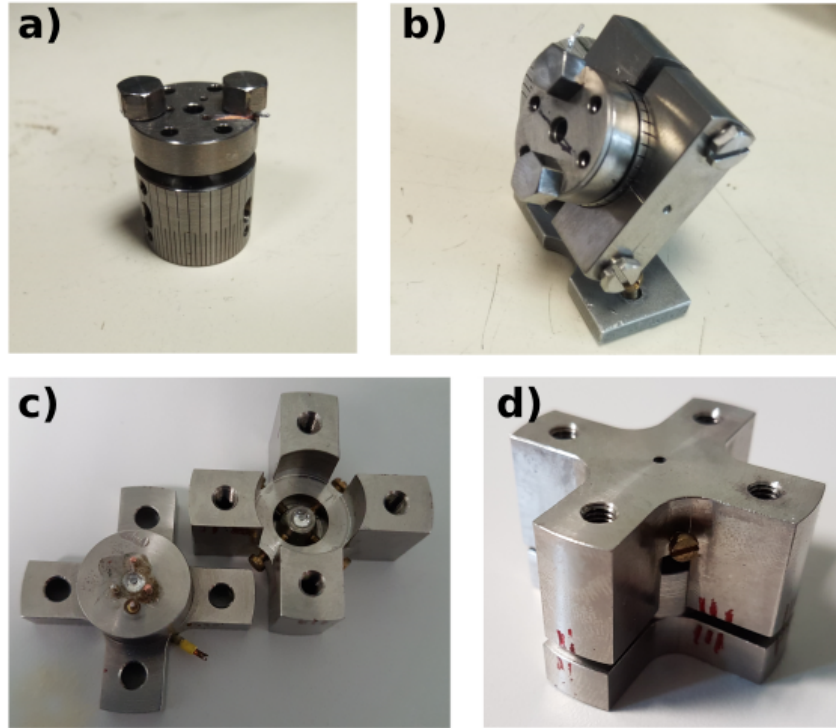


Figure 1.5: **Used LAC cells:** This picture shows the used TM1 and TM2 cells **a)**: closed cylinder cell, one can see the two screws and the angle marks on the cell body of 5° distance, **b)** a cylinder cell in the one axis goniometer, **c)**: open cross cell, **d)**: closed cross cell

The cell body, also described as outer structure, is important to apply force which is guided through the structure to the tips of the anvils. Our cell bodies are made from the Ti64, *grade23* alloy⁴⁹. The Ti64, *grade23* alloy is ideal for our uses due to its high strength and low magnetic susceptibility. The main difference between the TM1 and the TM2 design is the outer structure.

The **TM1** cell is a cylindrical cell (see Fig. 1.4 and Fig. 1.5 **a**) which fits in a goniometer that also acts as ground contact on the probehead (see Fig. 1.5 **b**). This allows orientation dependent measurements for single crystals. The TM1 cell was used for the single crystal investigations of $\text{YB}_2\text{Cu}_3\text{O}_{6+y}$. To apply pressure to the TM1 cell a hydraulic press is needed. Two screws are used to hold the pressure. The pressure limit of this cell type is around $p_{max} \approx 12$ GPa, due to the thin screws. Optical access is possible by two holes on the top and on the bottom along the cylindrical z-axis. Additionally 3 equally distributed holes are in radial direction in the \hat{x} - \hat{y} -plane.

The **TM2** cell is a so called cross cell (see Fig. 1.4 and Fig. 1.5 **d** and **c**). It is designed to reach higher pressures $p_{max} > 25$ GPa. The pressure is applied by tighten up the four screws simultaneously. The four thick titanium screws can hold much more load then the two screws of the TM1 cell. It can be grounded by a small ground contact which do not allow any changes of orientation. Which is the reason why these cells can only be used for powdered samples or nano crystalline samples. AgInTe₂ powder was investigated in these cells. Optical access is possible by the two holes, one at the top and one at the bottom and the openings at the sides.

INNER STRUCTURE

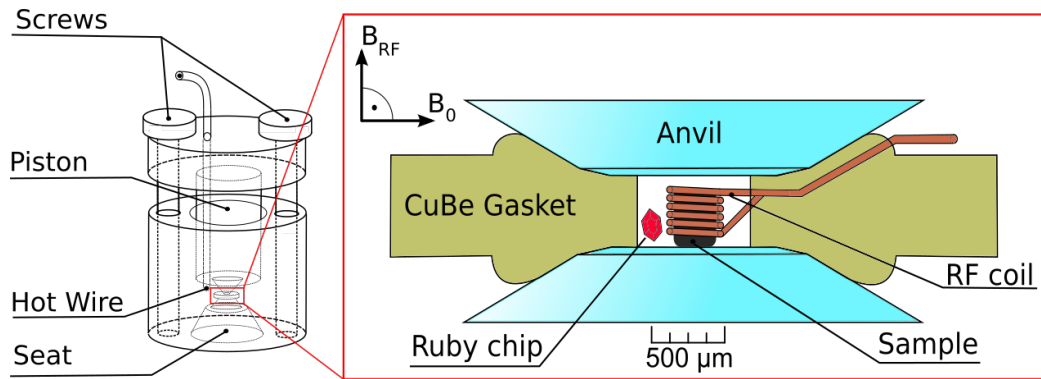


Figure 1.6: **NMR Anvil Cell Inner Structure:** Here the basic set up of the used NMR anvil cells is shown, the RF coil inside the sample chamber contains the sample, the ruby chip is placed to measure the pressure.

The inner structure is the characteristic element of a Diamond Anvil Cell. It contains the seats where the anvils are placed. These seats are important for the alignment of the anvils as well as for the transfer of the force to the tip. The seat in the shell part is movable by three small screws, which allow the positioning in respect to the piston counter part. On the piston part, three guide pins are distributed around the anvil to hold the gasket loose, to allow movements to prevent breaking. The piston also contains the hot wire which is strongly insulated from the grounded cell body. The preparation of the gasket including the microcoil and the contact to the hot wire is done on the piston part. In Fig. 1.6 the inner set up is depicted.

1.3.4 THEORY OF THE GASKET

In 1989, D. J. Dunstan published the "Theory of the gasket in diamond anvil high pressure cells"⁵⁰, which describes the deformation of the gasket with a hole between two anvils. In 1998 M. Eremets³⁹ supplied a larger scaled discussion on the gasket behavior.

D. J. Dunstan described the deformation of the gasket based on the plasticity theory of the continuum mechanic. In Fig. 1.7 the graphics from 1989 by D. J. Dunstan⁵⁰ are shown. Fig. 1.7 **a)** pictures the geometrical relations of the parameters. r_0 gives the radius of the culets, r_g gives the radius of the hole in the center of the gasket, t_0 gives the initial thickness of the gasket before the pre indentation, t gives the actual thickness of the gasket.

He separated the pressure scale in a DAC experiment into two different pressure regimes. At low pressures the "thin" gasket regime and at higher pressure the "thick" gasket regime. The "thin" regime is defined by a reduction of the radius while the height stays almost constant. For small radii r slightly above r_g the gasket flows in negative radial direction, which decreases r_g . The gasket at the outer edge near r_0 flows in positive radial direction. This predicts a radius r_s in between, $r_g < r_s < r_0$, with no favoring flow direction, which is called stationary. Here the largest value for the normal strength occurs $\sigma_n(r_s) > \sigma_n(r \neq r_s)$. The radius r_s of stationary flow behavior depends on the height t and the normal strength σ_n . While t stays almost constant in this regime r_s decreases with increasing the normal strength σ_n . In Fig. 1.7 **b)** the dependence of the normal stress σ_n/k is plotted as a function of radius r/r_0 . One can see a decrease of r/r_0 from a to d with increasing σ_n/k . In Fig. 1.7 **c)** the "thin" regime is denoted below the dashed and the dotted horizontal lines.

The regime transition is reached when r_s reaches the value of r_g ($r_s = r_g$). Now the whole gasket flows in positive radial direction, this is called the "thick" regime. It is defined by a decreasing height and an increasing radius. In Fig. 1.7 **b)** this is shown by e to g where the radius increases dramatically. g denotes the finale state, the material is quickly pushed out of the area between the anvils. In Fig. 1.7 **c)** the solid line (massive support: $n = 0$) and the chain dotted curve (massive support: $n = 3$) denote the normalized thickness t/r_0 . The intersection with the dotted or dashed curve denote the regime change. From this point the height will decrease described by the curve.

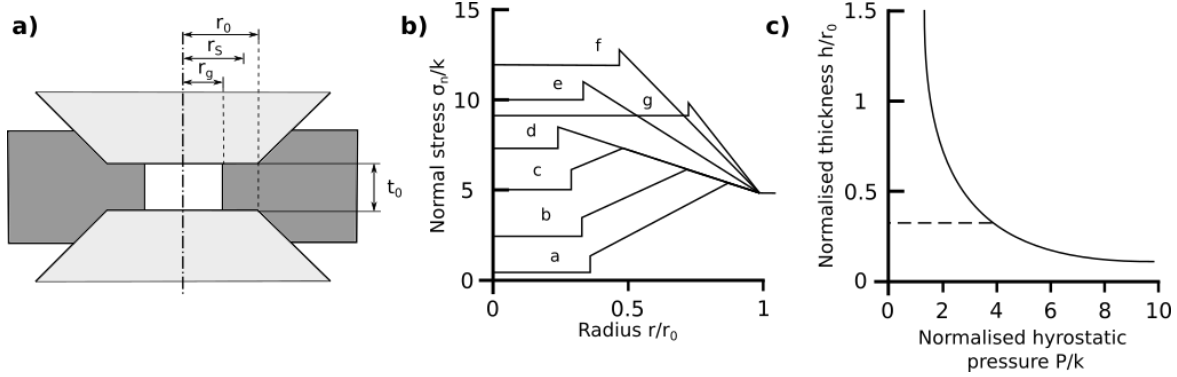


Figure 1.7: **Theory of the Gasket** graphics are a sketch from graphics made by D. J. Dunstan⁵⁰ **a)**: r_0 is the radius of the culets, r_g is the radius of the hole, t_0 gives the initial thickness of the gasket before the preindentation, t gives the actual thickness of the gasket, d is the size of the gasket plate. **b)**: the normal stress σ_n/k is plotted as a function of radius. One can see the radius decreases from $a-d$ by while the load is increased. From e to f and g the radius increases much. Between d and e the regime changes from "thin" to the "thick" regime. In the thin regime the radius decreases in the thick regime it increases. g illustrated a unstable region **c)**: gives the decay of the height due to pressure, the solid line and the dash dotted line is a plot of equation (1.29) for different values of massive support. The dashed line and the dotted line symbolize the initial constant height in the thin gasket regime.⁵⁰

D.J. Dunstan⁵⁰ introduced the following formulas for his description, shown in 1.7 **b)** and **c)**:

$$\sigma_n = (n + 1)k + \frac{2k}{\sqrt{3}} \left(\frac{r_0}{t} - \frac{r}{t} \right), \quad r_g \leq r \leq r_0 \quad (1.27)$$

$$\sigma_n = nk + \frac{2k}{\sqrt{3}} \left(\frac{r_0}{t} - \frac{r_g}{t} \right), \quad r < r_g \quad (1.28)$$

and for the height reduction in the thick gasket regime shown in 1.7 **c)** the following formula:

$$t_{max} = \frac{2k}{\sqrt{3}(p - nk)} \quad (1.29)$$

Considering (1.28), the ratio of $\frac{r_0 - r_g}{t}$ seems to be a characteristic ratio for the behavior of the gasket under pressure. This ratio is calculated for all cells at every pressure to observe their behavior (Fig. 4.6 in sec. 4.2.3)

For more details about the theoretical description and the derivation see the cited paper⁵⁰ by D.J. Dunstan, or the book³⁹ by M. Eremets.

WORKING REGIME FOR SINGLE CRYSTALS

Single crystals in a DAC need a special treatment. The observation of the chambers dimensions are necessary to make sure that the crystal is not pressurized uniaxially. The deformation of the gasket is important to observe while pressure is increased. Due to the fact that the crystal is enclosed by a coil the relative small radial changes in the "thin" gasket regime do not disturb the alignment or the condition of the crystal.

This means the ideal regime for single crystal measurements is the "thin" gasket regime. Here one can observe a small reduction of the chamber diameter and an almost constant height. This allows good measurements under good conditions.

In the "thick" gasket regime the diameter increases while the height is reduced proportional to $\propto 1/p$ (eq. 1.29) (see Fig. 1.7 c). This leads to a maximal pressure, limited by the reduced gasket height, shortly before the crystal is squeezed uniaxially by the two touching anvils. To extend the working range of pressure as far as possible, it is important to have an eye on the ratios above. Furthermore a chamber monitoring is needed to prevent an uniaxially squeezing, tilting or breaking of the crystal caused by the approximate anvils.

1.3.5 PRESSURE MEDIUM

Hydrostatic conditions in the sample chamber can be achieved by adding a pressure transmitting medium. Different types of liquids and gases can be used^{38,39}. Gases for example Helium, Argon, Xenon and liquids like paraffin oil or a mixture of methanol and ethanol are common. N. Tateiwa^{51,52} found a ratio of (4:1) of methanol and ethanol to be almost perfect hydrostatic up to 10 GPa.

For our uses in a NMR Anvil Cell paraffin oil is the most attractive pressure medium. Alcohols could dissolve the epoxy resin or the cold temperature varnish which are used to stabilize the micro RF coil. Paraffin oil is a good pressure transmitting medium up to 9 GPa. Around ≈ 9 GPa paraffin oil has a glass transition (amorphization)^{51,52,53} which do not allow the use of it as hydrostatic pressure medium at higher pressures.

In NMR non hydrostatic conditions or pressure gradients would increase the linewidth of a pressure sensitive transition⁵².

COMPRESSABILITY OF LIQUIDS

The relation between pressure and the density of matter is described as compressability. In the following section a short introduction to the compressability of liquids is shown based on the book from D. Will⁵⁴.

For hydraulic uses the model based on incompressible liquids is often used. But for high pressures the volume reduction is not negligible. Especially for the pressure ranges of a DAC, the reduction of the volume of the sample chamber is a parameter which has a big influence on the planing of the experiments

The volume reduction depending on pressure can be described by the following formula:

$$\kappa = -\frac{1}{V} \frac{\Delta V}{\Delta p} \quad (1.30)$$

ΔV denotes the change of the volume, V is the actual volume, Δp is the corresponding pressure difference and κ is the bulk modulus of the liquid.

In general the relation $\Delta V/V = f(p)$ is not a linear function in p , which means the bulk modulus is not constant, and pressure dependent⁵⁴.

By assuming the Δ as continuous, a function can be derived by integration:

$$V(p) = V_i \cdot \exp(-\kappa \cdot p) \quad (1.31)$$

V_i is the initial volume, this formula is used as fit function for the volume reduction of the anvil cell's chamber, discussed in sec. 4.2.4.

For air free mineral oils, which paraffin oil is, the bulk modulus is given in literature with $\kappa = 1.4 - 1.6 \cdot 10^4$ bar⁵⁴.

1.3.6 MEASURE THE PRESSURE

To measure the pressure, different approaches had been used in the past. First, a pressure sensitive system is needed which can easily be read out by a simple measurement. Then the change of the sensitive part of the system has to be gauged under the application of pressure. In this subsection different gauged pressure scales are introduced. In our daily routine with anvil cells the ruby scale was used.

P.W. Bridgman used for the first high pressure experiments resistance measurements. Later he used the freezing pressure of liquid mercury²³. P.W. Bridgman used tungsten carbide anvils which did not allow an optical access to the high pressure chamber. In 1972 G. Piermarini⁴⁰ introduced the ruby scale. This became possible by using optical transparent diamonds as anvils and a ruby chip. Ruby has two pressure sensitive optical transitions the so called R_1 and the R_2 line. At ambient conditions $R_1 = 694.25$ nm and $R_2 = 692.86$ nm. H.K. Mao⁴¹ and P.M. Bell³⁰ extended the calibrations⁵⁵:

$$P[GP a] = n \frac{1904}{B} \left[\left(1 + \frac{\delta\lambda[nm]}{\lambda_0[nm]} \right)^B - 1 \right] \quad (1.32)$$

With λ_0 as wavelength of the R_1 line at ambient conditions, and $\delta\lambda$ its corresponding position under pressure. $B = 7.655$ is a numerical coefficient which is valid for hydrostatic conditions. $B = 5$ for quasi and non hydrostatic conditions.

In 1992 J. Yen⁵⁶ investigated the temperature dependence of the pressure dependent R_1 and R_2 line and allowed with this also pressure measurements at low temperatures. In 2007 the calibration was extended by I. Silvera³³ up to 150 GPa. Nowadays the 'Ruby Scale' technique is the most common in the middle to high pressure regimes.

In the year 2010 K. Kitagawa⁴² introduced the Knight shift of the nuclear quadrupole resonance (NQR) of Cu_2O of metallic tin as pressure gauge and provided temperature and pressure dependent data up to 10 GPa.

An new approach was made by A. Podlesnyak⁵⁷ in 2018, using $\text{SrB}_4\text{O}_7:\text{Sm}^{2+}$ as pressure sensor. The big advantage of the *Sr*-borate 0-0 line is the temperature independence of the wavelength. Unfortunately these investigation reached only pressures up to 2 GPa.

1.4 NMR UNDER PRESSURE

In this section NMR in an anvil cell is considered. A state of the art is presented as well as a short discussion which influence pressure as parameter can have to a NMR experiment.

1.4.1 HIGH PRESSURE NMR AND STATE OF THE ART

High pressure NMR is a powerful probe to investigate interactions of nuclei depending on varied energy densities^{3,17,45}. Unfortunately the principle of miniaturization generates difficulties in the sensitivity. M. Conradi^{58,59,60,61} discussed, various approaches of high pressure NMR. Faraday induction in a coil depends strongly on the filling factor, precisely on the number of rotating dipoles or nuclei contained in the coil's volume V_{coil} . A bad filling factor is the result of winding the coils around the anvils. The small sample in the anvil cell's chamber in such a design is only a small fraction of the volume of the coil.

In general, a compromise between a large sample space and the maximum pressure influences the planing of such an experiment. Different architectures of anvil cells were tested in the past. An example, a piston cylinder type cell⁶² (up to 4 GPa) and a Bridgeman type cell^{63,64} (over 10 GPa) differ in sample size by a factor of 10^3 .

I. Silvera⁶⁵ and M. Pravica come up with the idea to use a split gasket as a single loop resonator in 1998. ^1H NMR spectra of molecular hydrogen were recorded at 12.8 GPa and 20 K. Even with the low Q factor of the used split rhenium gasket they reached a SNR of about 10 after 1500 scans.

To increase the filling factor also other approaches were realized. A saddle shaped coil around the anvils is a combination of two coils, split on two opposed sides of the sample. This was used in a large number of studies^{66,67,68}. Later, the SNR of a solenoid coil was compared to a saddle shaped coil with equal radii by T. Okuchi¹⁷ in 2005, with the result, the SNR of a solenoid coil is up to three times larger. A. Webb¹⁵ presented in 1999 a multiple microcoil arrangement. One and two dimensional spectra of 1-butanol, galactose, fructose and other molecules were recorded simultaneously. It was possible to reduce the SNR from the coils by 50%, using a switch set up instead of a single microcoil with a conventional receiver chain. In 2001 D.A. Seeber¹⁶ designed a set of different microcoils. They varied the lead lengths, turn spacing and the resistance, to investigate the effects on the SNR performance. In their smallest microcoil they reached an impressive SNR of ≈ 0.1 .

Bulk sensitive high pressure experiments in an anvil cell like NMR, AC susceptibility⁴³ or Haas van Alphen⁶⁹ measurements need a high filling factor for a good SNR. In 2003 P. Alireza placed a microcoil inside the sample chamber between the anvils to do AC susceptibility measurements⁴³. In the year 2009 this new approach, with a microcoil placed inside, was tested in NMR experiments^{3,70}. A cooperation of the Cambridge University and the University of Leipzig led to NMR measurement under high pressure.

A microcoil with a diameter of 300 μm enclosed the sample. The microcoil was connected by the legs of the coil, which were placed in carved channels in the gasket sealed by epoxy resin. A coil directly around the sample in the high pressure chamber increased the SNR dramatically in comparison to the older approaches with coils outside. In Japan in 2010, K. Kitagawa and H. Gotou⁷¹ presented a comparable NMR cell design. Their sample space of a modified Bridgeman type cell had a large volume of 7 mm³. Further, an apparatus to fill the sample chamber with argon as pressure medium and an optical entrance by a glass fiber were part of their cell design. A two axis goniometer, controlled mechanically, allowed a precise alignment of single crystals. They introduced a pressure gauge depending on NQR measurements of copper oxides to measure pressures up to 9 GPa. In 2014 M. Takigawa and K. Kitagawa⁷² used this NMR cell design to investigate the phase diagram and the superconductivity of a single crystal of NaFeAs up to 7.3 GPa. They recorded a rapid reduction of the transition temperatures by increasing pressure. In 2015 J. Haase and T. Meier⁷³ achieved a NMR experiment up to 30 GPa. The composite gasket technique was used, it combines the CuBe gasket with a nano crystalline powder (c-BN, diamond, $\alpha\text{-Al}_2\text{O}_3$) surrounded with epoxy resin for more stability. In 2017 T. Meier⁷⁴ used the old approach with a saddle shaped coil around the anvils combined with Lenz lenses^{75,76} placed on the culets to focus the magnetic flux to the sample chamber. They reported NMR data at pressures up to 72 GPa.

1.4.2 EFFECTS OF PRESSURE TO A NMR EXPERIMENT

Pressure can have different effects on a solid state NMR experiment. While temperature changes the the population of levels, pressure influence the chemical as well as the electronic structure. In the following some possible occurring effects on an NMR experiment under pressure are presented.

The Knight shift² is a shift of the resonance frequency due to the interaction of the nuclei with the conduction electrons. By increasing the density of states at the Fermi edge the amount of conducting electrons and with this, the conductivity increases^{23,77}, which affects the Knight shift, as well.

The quadrupole splitting^{2,13}, is a splitting of transition lines due to a field gradient at the nucleus (sec. 1.1.2). Pressure can change field gradient and with this the splitting.

A phase transitions, which can occur by the application of pressure^{23,24,78,44}, can change the complete surrounding of the nuclei. For example an insulator metal transition is clearly observable by a jump in the resonance frequency caused by an incipient Knight shift⁴⁴. A phase change of the complete crystal structure for example, can change the linewidth slightly or even broaden it significantly.

*“The good thing about science is that it’s true
whether or not you believe in it.”*

Neil deGrasse Tyson

2

Samples

In this chapter the investigated samples, Yttrium-Barium-Copper-Oxid ($\text{YBa}_2\text{Cu}_3\text{O}_{6+y}$) and Silver-Indium-Telluride (AgInTe_2) are introduced. The crystal structure, the NMR relevant parameters, the preparation, and a short historical and scientific text is given.

2.1 YTTRIUM-BARIUM-COPPER-OXIDE

Yttrium-Barium-Copper-Oxide also called $\text{YBa}_2\text{Cu}_3\text{O}_{6+y}$ or YBCO is a cuprate superconductor with a critical temperature ($T_c \approx 92\text{ K}$) above the boiling temperature of liquid nitrogen ($T_b = 77\text{ K}$). In this thesis is focused on $\text{YBa}_2\text{Cu}_3\text{O}_{6+y}$, other YBCO mixtures like $\text{YBa}_2\text{Cu}_4\text{O}_8$ or $\text{Y}_2\text{Ba}_4\text{Cu}_7\text{O}_y$ are not considered in this work.

2.1.1 DISCOVERY

G. Bednorz and K. Müller⁷⁹ discovered in 1986 at the IBM in Zürich that some copper oxides show a relative high critical temperature for superconductivity. Lanthanum-Barium-Copper-Oxides showed a $T_c = 35\text{ K}$. In 1987 Bednorz and Müller won the Noble Prize in physics⁸⁰.

In 1987⁸¹ a team from the University of Alabama in Huntsville and the University of Houston discovered YBCO with a critical temperature ($T_c \approx 92\text{ K}$) above the boiling temperature of liquid nitrogen ($T_b = 77\text{ K}$). The so called black phase⁸² was found at the Carnegie Institution of Washington and is today known as $\text{YBa}_2\text{Cu}_3\text{O}_{6+y}$.

The most remarkable thing here is the high critical temperature in this ceramic. The BSC-theory can not explain the cooper pair building above temperature around $\approx 40\text{ K}$, due to the high thermal energy of the lattice vibrations which should impede the cooper-pair-building⁸³.

Till today a giant number of investigations^{7,8,82,84} of these superconducting ceramics had been done, but still a lot of questions remain unanswered.

2.1.2 CRYSTAL STRUCTURE

YBCO crystallizes into a layered defect perovskite structure⁸⁵. A plane of square planar CuO_4 units define the boundary of each layer. The unit cell of YBCO is symmetric along the \hat{c} -axis around the yttrium atom, which is enclosed by two CuO_2 -planes. The Yttrium-Copper-Oxide plane section is enclosed by two BaO-plane and the CuO-chains above and below. The lengths of the crystal axis are $|\vec{a}| = 3.82\text{\AA}$, $|\vec{b}| = 3.89\text{\AA}$ $|\vec{c}| = 11.68\text{\AA}$. A sketch of the unit cell is shown in Fig. 2.1 a).

The CuO_2 -plane is the common feature of all high-temperature superconductors which allows the assumption that this plane is a necessary puzzle piece of cuprate superconductivity⁷, while the CuO-chains could act as charge reservoir⁸⁶. A large anisotropy in conductivity is observed, along the \hat{a} - \hat{b} -plane it is about 10 times larger than along the \hat{c} -axis⁸.

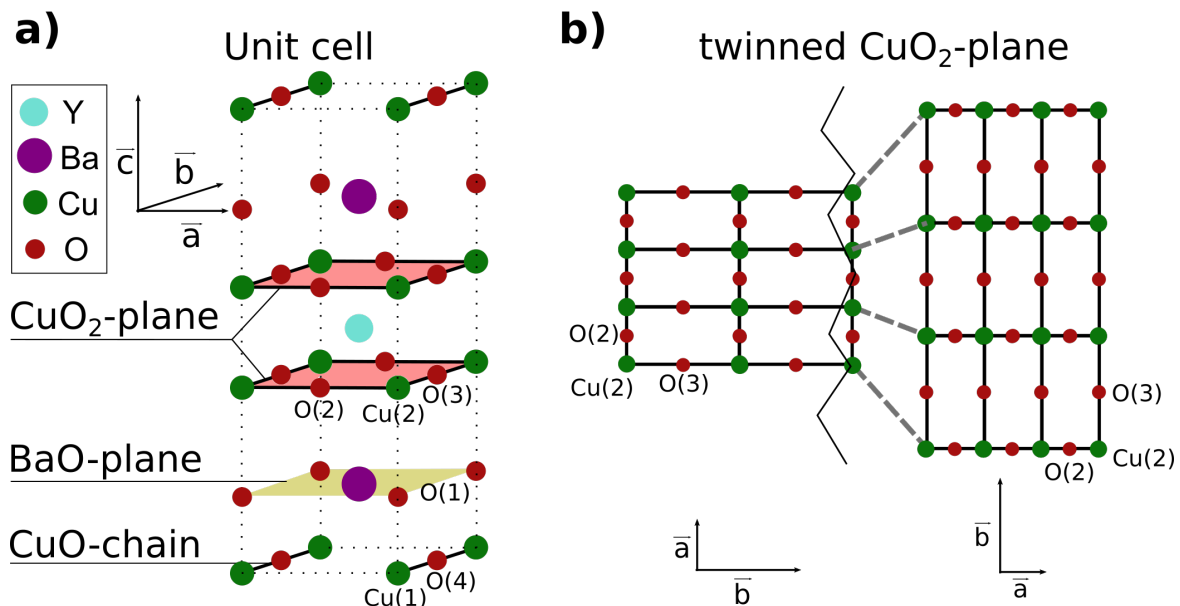


Figure 2.1: **YBCO Crystal structure:** a) A sketch of the crystal structure of $\text{YBa}_2\text{Cu}_3\text{O}_{6+y}$, marked are the different planes as well as the different copper and oxygen positions in the unit cell⁸⁵. b) A sketch of a twinned crystal, which occurs in YBCO crystals along the \hat{a} - \hat{b} -plane.

The designation of the different oxygen and copper positions:

- O(1): apex oxygen, oxygen position in BaO-plane
- O(2): oxygen position in the CuO₂-plane, bond along the \vec{a} -axis
- O(3): oxygen position in the CuO₂-plane, bond along the \vec{b} -axis
- O(4): oxygen position in the CuO chain
- Cu(1): copper position in the CuO-chain
- Cu(2): copper position in the CuO₂-plane

In Fig.2.1 b) a sketch of the twinned orthohombic CuO₂-plane is shown. This feature occurs in the synthesis process of YBCO. The boundaries in between can be identified by polarized light, and are called twinning lines. These lines are used to find the orientation of the crystals under the microscope. The \hat{c} -axis is perpendicular to the CuO₂-plan and to the surface were the twinning lines optically occur^{7,9}.

2.1.3 MATERIAL PROPERTIES, NMR

The NMR relevant properties of the nuclei are shown in tab. 2.1. NMR experiments were only done at the copper (⁶³Cu, ⁶⁵Cu) and oxygen (¹⁷O) isotopes. YBCO is a good candidate for NMR investigations due to narrow NMR lines and clear spectra⁸⁶.

	spin I	γ (10^7 rad/sT)	NA (%)
⁸⁹ Y	1/2	-1.316	100
¹³⁵ Ba	3/2	2.677	6.59
¹³⁷ Ba	3/2	2.992	11.23
⁶³ Cu	3/2	7.112	69.15
⁶⁵ Cu	3/2	7.604	30.85
¹⁷ O	5/2	-3.628	0.038

Table 2.1: Properties of the NMR active Yittrium, Barium, Copper and Oxygen isotopes⁸⁷

2.1.4 SYNTHESSES AND OXYGEN EXCHANGE

A basic synthesis of YBCO can be done easily, but for high quality crystals a lot of experience is needed. An oven that reaches and holds a temperature of $T = 900^\circ\text{C}$ is required. Yttrium nitrate, Barium nitrate, Copper nitrate and Oxalic acid are needed for the chemical reaction at these temperatures⁸⁸. The superconducting properties of $\text{YBa}_2\text{Cu}_3\text{O}_{6+y}$ crystals depend strongly on the oxygen content which is varied with y . Chemical doping with oxygen has an influence on the hole and electron doping in the CuO_2 -plane.

The high quality YBCO single crystals used in this thesis were grown and annealed in a BaZrO_3 crucibles. A more precise description is given by A. Erb⁸⁹ who made the high quality crystals used in this thesis.

Fully oxygenated ($y=0$) single crystals, twinned in $\hat{a}-\hat{b}$ -plane, were placed under elevated temperatures in an $^{17}\text{O}_2$ atmosphere for an isotope exchange. An exchange rate of about 25% was reached⁹. The doping content was adjusted by an annealing of the crystals to the desired chain oxygen content. Later the crystal was cut along the crystal axis into small micro-crystals which fit in a NMR anvil cells.

2.1.5 ELECTRONIC PHASE DIAGRAM AND SUPERCONDUCTING DOME DEPENDENCIES

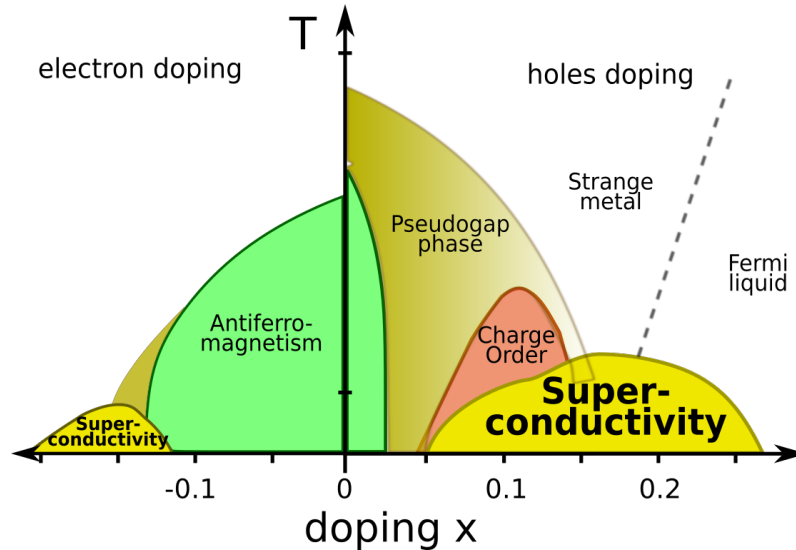


Figure 2.2: **Doping dependent Phase diagram:** The variation of the chemical doping content x in cuprate superconductors results in different electronic phases. The focus in this thesis is on the right side, for hole doped samples.

It is possible to dope cuprate superconductors chemically and vary with this the charge content in the CuO_2 -plane. High-Temperature-Superconductors (HTS) can be hole or electron doped, the variable x gives the average planar chemical doping level deduced by the stoichiometry. For example by Lanthanum-Strontium-Copper-Oxide (LSCO) with the stoichiometry $\text{La}_{2-x}\text{Sr}_x\text{CuO}_4$. In the case of YBCO, the oxygen doping in the plane can not be deduced just by the stoichiometry, y is used here.

However, the variation of x shows different electronic phases, which are believed to occur in all cuprates. The electronic phase diagram is given in Fig. 2.2. The undoped YBCO is an insulator with an antiferromagnetic ground state. Two superconducting domes are shown, colored in yellow, one for electron doping ($x < 0$) the other for hole doping ($x > 0$). The hole doped dome shows a small plateau in $T_c(x)$ at $x \approx 0.125$ ⁹⁰. In light red one can see a charge order dome, above in light brown the pseudogap phase is depicted. The gap and ordering phenomena were discussed in the past^{91,92}. The antiferromagnetic phase is shown in green, it is much more pronounced in the electron doped area ($x < 0$). Strongly hole doped materials show a "normal"-metal behavior.

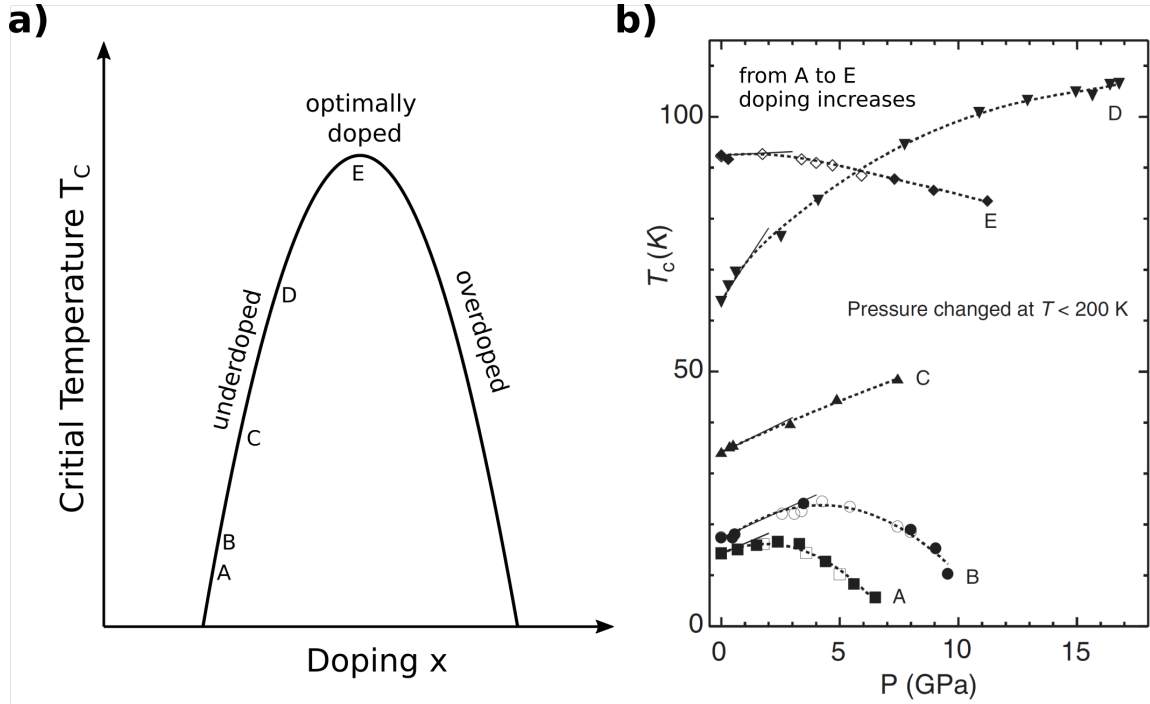


Figure 2.3: **T_c -dependence domes:** **a)** here the superconducting dome is shown. The doping dependence of $T_c(x)$ is depicted, **b)** the measured dependency of the critical temperature on pressure on differently doped YBCO samples. The doping increases from A to E. While A to C are strongly underdoped samples. D with the strongest pressure response has the formula of $\text{YBa}_2\text{Cu}_3\text{O}_{6.63}$. E denotes optimal doping. (This graphics are taken from the "Handbook of High-Temperature Superconductivity"^{7,8})

The doping level with the highest T_c is called optimal with a value of $x \approx 0.15$. In Fig. 2.3 a) the superconducting dome doping dependence of $T_c(x)$ is sketched. For values below and above the optimal doping the critical temperature is below ($T_c(x_{optimal}) > T_c(x \neq x_{optimal})$).

Doping is not the only variable which influences the superconducting dome, pressure as well as an external magnetic field have influence to the shape⁷. The pressure effects were investigated by J.S. Schilling^{8,93}.

In Fig. 2.3 b) the pressure dependence of T_c for differently doped YBCO samples is shown^{7,8}. The doping increase from A-E. The samples A-C show the pressure dependence of T_c for strongly under doped samples, a dome shaped dependence is depicted. Sample D ($\text{YBa}_2\text{Cu}_3\text{O}_{6.63}$) is underdoped as well, but shows the strongest increase in T_c . It even surpasses the maximal T_c achieve able by doping. Sample E is an optimal doped sample. Here T_c decrease by the application of pressure.

2.1.6 PRESSURE DEPENDENCE OF T_c

Fig. 2.3 **b**) shows the effect of pressure to differently doped samples of $\text{YBa}_2\text{Cu}_3\text{O}_{6+y}$. T_c of underdoped samples tends to increase if pressure is applied. While optimally doped crystals show a weak decrease in T_c . Usually, T_c of overdoped samples decrease by pressure^{94,95}. Conductivity and Hall measurements showed that the application of pressure to $\text{YBa}_2\text{Cu}_3\text{O}_{6+y}$ crystals increase the planar hole doping^{94,96}

The fact that some underdoped samples show a significantly higher $T_{c,max}(p)$ than what can be achieved by chemical doping points to an intrinsic pressure effect, a mechanism not affected by doping.

$$\left(\frac{dT_c}{dp}\right)_{total} = \left(\frac{\partial T_c}{\partial x}\right) \left(\frac{\partial x}{\partial p}\right) + \left(\frac{dT_c}{dp}\right)_{intrinsic} \quad (2.1)$$

The first part on the right side of equation (2.1) ($\partial T_c/\partial x$) describes the changes of T_c by the change of doping x . The second part ($\partial x/\partial p$) describes the change of doping x by the effect of pressure p . The last part on the right side ($(dT_c/dp)_{intrinsic}$) describes the intrinsic effect on T_c by pressure. In this thesis these effects are considered.

2.1.7 SELECTED YBCO INVESTIGATIONS

In this section some selected NMR related investigations done in Leipzig shall be presented as well as some formal relations.

It was shown that the charges in the CuO_2 -plane can be measured at an atomic level by NMR^{84,97}. The relation between the Cu and O quadrupole splitting along the respective principle axes to the planar hole densities n_{Cu} and n_O is given by^{84,97}:

$$^{17}\nu_{Q,\sigma} = 2.453 \text{ MHz} \cdot n_p + ^{17} C_c \quad (2.2)$$

$$^{63}\nu_{Q,c} = 94.3 \text{ MHz} \cdot n_d - 5.68 \text{ MHz} \cdot 4(2 - n_p) + ^{63} C_c \quad (2.3)$$

This allows the determination of the doping ζ measured by NMR. It follows the relation given by⁹⁷:

$$\zeta + 1 = n_{Cu} + 2n_O \quad (2.4)$$

ζ adds a nominal hole to the already present in the parent compound. Here one has to separate between the doping chemically x or y and the doping measured by NMR ζ .

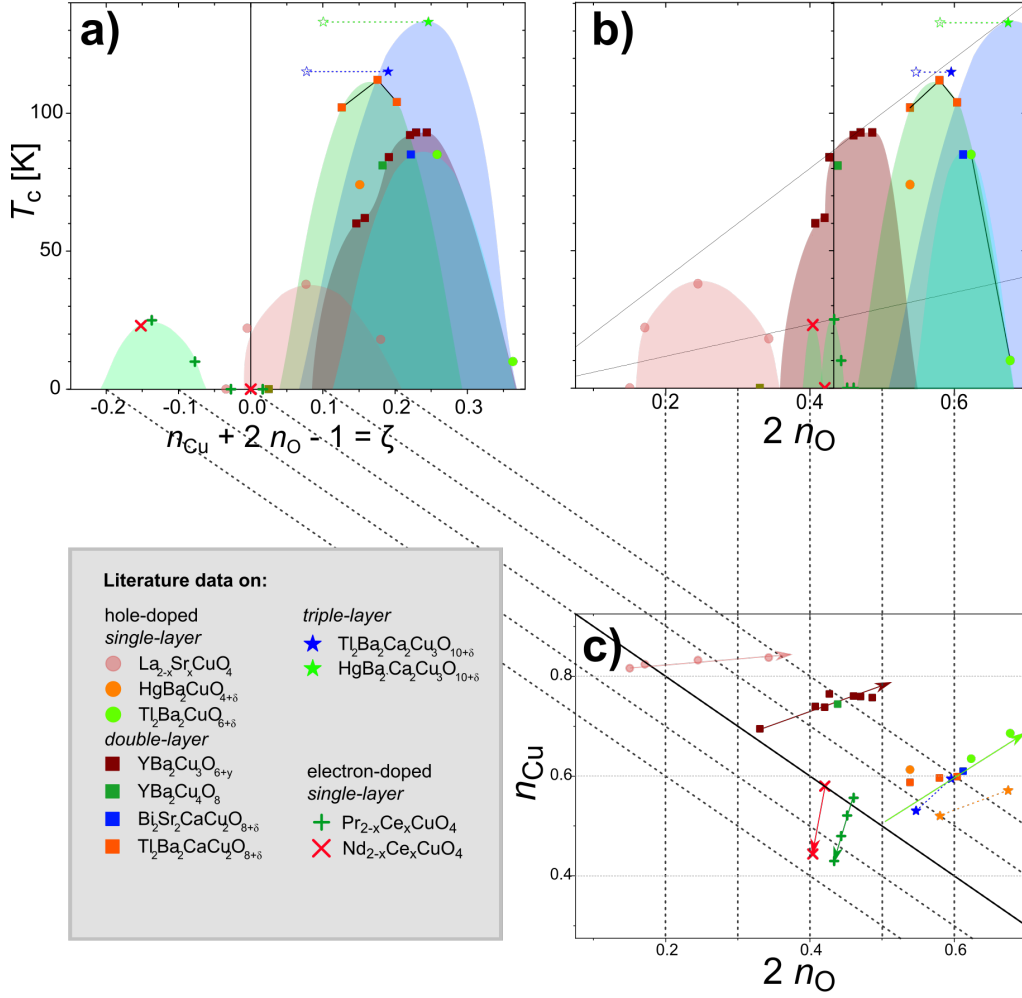


Figure 2.4: **NMR Phase diagram of selected cuprates:** **a)** T_c as a function of ζ . ζ is the hole doping measured by NMR. **b)** Here the critical temperature T_c is given as a function of $2n_O$. A proportionality between $T_{c,max}$ and n_O is revealed. **c)** A plane of n_{Cu} and $2n_O$ reveals the differences between the various cuprate families. It further relates to the plots a) and b) above.

Fig. 2.4 a) shows a categorization of different cuprates by ζ , the doping measured by NMR. Here the superconducting domes of the different families do not lay above each other like the domes dependent on the chemical doping x do ($x_{optimal} \approx 0.15$).

It was found^{97,98} a order of cuprates according to their maximal T_c depending on the oxygen hole content $2n_O$ of the CuO_2 -plane (see Fig. 2.4 b)). This was very recently confirmed by a three-band Hubbard model with cellular dynamical mean-field theory done by the group of André-Marie Tremblay at the Université de Sherbrooke⁹⁹.

By the combination of Fig. 2.4 a) and Fig. 2.4 b) a $n_{\text{Cu}}-2n_{\text{O}}$ -plane can be shown (Fig. 2.4 c)). The black diagonal 'parent' line, for $\zeta = 0$ is the boarder between hole and electron doped materials, every family starts at an other point around $\zeta = 0$. The different sharing mechanism between the cuprate families influence the slope in the $n_{\text{Cu}}-2n_{\text{O}}$ -plane of chemical doping. For YBCO (brown) it is $\Delta n_{\text{Cu}}/\Delta n_{\text{O}} = 0.52$.

2.1.8 YBCO NMR UNDER PRESSURE

In this last subsection, two high-pressure NMR investigations which had been done in the past at the University of Leipzig shall be presented.

In 2011 T. Meissner^{93,100} investigated the electronic properties of $\text{YBa}_2\text{Cu}_4\text{O}_8$ above the critical temperature. The pseudo gap feature indicated by a temperature dependent spin susceptibility of the oxygen signals (O(2) and O(3)) in the copperoxid-plane were vanished by the application of pressures up to 6.3 GPa. The measured data are shown in Fig. 2.5. One can see the effect of pressure which closes step by step the pseudo gap for the O(2,3) signals while the spin susceptibility of the apex oxygen O(1) is unchanged if pressure is applied. The idea of a two component spin susceptibility was discussed, where the first component displays the characteristic T-dependence which is the dominant part at ambient conditions. At elevated pressures this component first component decreases, while the second component increases strongly.

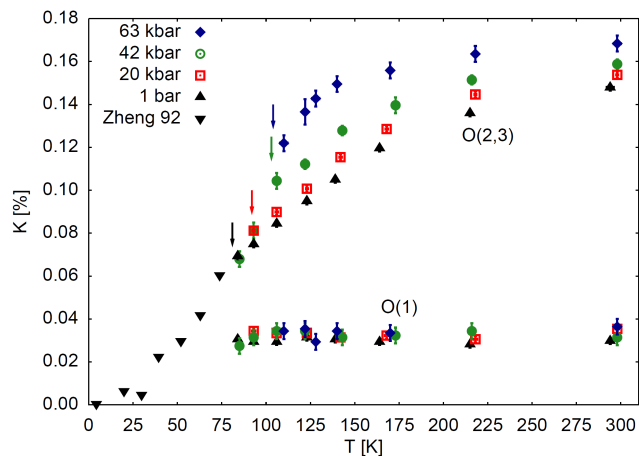


Figure 2.5: **Closing the Pseudogap:** ^{17}O NMR shifts temperature dependency. The arrows mark the measured critical temperature T_c at the actual pressure. O(1) denotes the signal of the apex oxygen position, which is unaffected by the application of pressure. O(2,3) correspond to the oxygen nuclei in the CuO_2 -plane. This graphic was published by T. Meissner¹⁰⁰ in 2011

In 2018 S. Reichardt^{6,9} discovered a commensurate charge density variation in the CuO_2 -plane by the investigation of an almost optimally doped single crystal of $\text{YBa}_2\text{Cu}_3\text{O}_{6.9}$ up to 1.8 GPa predicted earlier⁸⁴. He observed the change of the double peak feature of his sample and the effect of pressure at the temperature of 100 K and 300 K. S. Reichardt⁶ presented a full set of NMR data of a $\text{YBa}_2\text{Cu}_3\text{O}_{6.9}$ single crystal under pressures up to 1.8 GPa. The effect of pressure was interpreted to increase the strength of a bulk charge ordering and that this is ubiquitous in the CuO_2 -plane of all cuprates. In 2019 I. Vinograd¹⁰¹ disagreed, they investigated the effect of hydrostatic pressure on the charge density waves (CDW) in $\text{YBa}_2\text{Cu}_3\text{O}_{6+y}$ under pressure up to 1.9 GPa and found a slightly weakened.

For the evaluation in this thesis in sec. 5.2.2, concerning the charges in the $2n_{\text{O}}-n_{\text{Cu}}$ -plane, the data of the work from S. Reichardt for the sample Y-6.9 were also used.

2.2 SILVER-INDIUM-TELLURIDE

Silver-Indium-Telluride (AgInTe_2) belongs to the family of *chalcogenides*. The ternary semiconductor has a non zero Seebeck coefficient which assigns it to the group of thermoelectrics. The efficiency of a process, where waste heat is a decisive factor, and could be increased by the generation of electric energy using a thermoelectric material^{102,103}. Unfortunately (AgInTe_2) is not the "best" thermoelectric material, nevertheless it is of interest in the research.

A detailed description of the synthesis is given by Y. Aikebaier¹⁰⁴. It was done by S. Welzmüller and O. Öckler at the chemistry department at University of Leipzig^{105,106}.

2.2.1 MATERIAL PROPERTIES, NMR

The used AgInTe_2 samples were only available as polycrystalline powder. For the usage in the NMR anvil cells it was ground to a fine powder. Due to the low natural abundance of the NMR active Te isotopes and the very low Lamor frequency of the Ag isotopes (see tab. 2.2) combined with the extreme small sample volume and bad SNR only ^{115}In NMR was feasible. In table 2.2 the NMR relevant material properties are shown:

	spin I	γ (10^7rad/sT)	NA (%)
^{107}Ag	1/2	-1.087	51.82
^{109}Ag	1/2	-1.25	48.18
^{115}In	9/2	5.8908	95.72
^{113}In	9/2	5.8782	4.28
^{125}Te	1/2	-8.498	6.99
^{123}Te	1/2	-7.049	0.87

Table 2.2: Properties of the NMR active Silver, Indium and Telluride isotopes⁸⁷

2.2.2 CRYSTAL STRUCTURE

The chalcopyrite structure⁷⁸ of AgInTe_2 is shown in Fig. 2.6 a). A detail structure analysis of the samples used in this thesis was done by S. Welzmüller^{105,106}. The chalcopyrite structure appears at ambient conditions, with a high degree of local symmetry, it forms the space group $I-42d$. Every atom is tetrahedrally coordinated by four next neighbors. The lattice parameters are $a = 6.45742(6)$ Å and $c = 12.65146(17)$ Å. By the consideration of $2a > c$ one can see a lack of symmetry, the unit cell is a little shrunk in \hat{c} -direction.

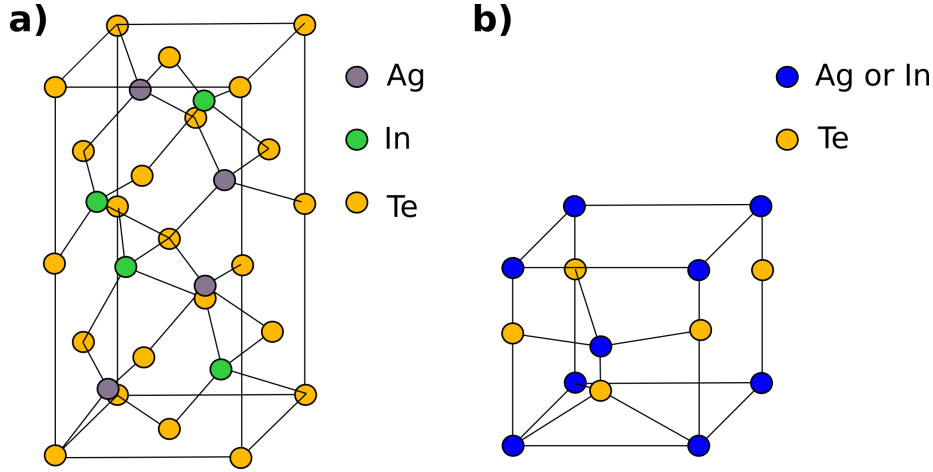


Figure 2.6: **AgInTe Crystal structure:** a) A sketch of the chalcopyrite structure b) A sketch of a cation-disordered orthorhombic structure with spacegroup Cmcm

2.2.3 PHASE TRANSITIONS

In 1969 K.J. Range⁷⁸ investigated the structural changes if hydrostatic pressure is applied by X-Ray diffraction. A structural phase transition in AgInTe_2 at pressures above 1.5 GPa and a temperature of 350 °C was observed. At room Temperature the phase transition occurs at 3 - 4 GPa¹⁰⁷. The high pressure phase is a cation-disordered orthorhombic structure with spacegroup Cmcm shown in Fig. 2.6 b). The disordered rock-salt type structure or a mixture of Cmcm- and NaCl-structure are discussed in literature^{78,107} as well. The high pressure phase has a much higher conductivity of about 10^3 . When pressure is released the high pressure phase stays stable for several weeks. Then it decays to a meta stable zincblend-type structure. An annealing at 1 bar and 150 °C generates the highly ordered chalcopyrite structure again. An ab initio study of the phase transitions was done by Komsilp Kotmool¹⁰⁸ in 2015.

- The chalcopyrite structure (AgInTe_2 -I) has a density of $\rho_{\text{I}} = 6.15\text{g}/\text{cm}^3$
- The NaCl-structure (AgInTe_2 -II) has a density of $\rho_{\text{II}} = 7.28\text{g}/\text{cm}^3$.
- The Cmcm-structure (AgInTe_2 -III) has a density of $\rho_{\text{III}} = 7.53\text{g}/\text{cm}^3$.
- The zincblend-type-structure (AgInTe_2 -IV) has a density of $\rho_{\text{IV}} = 6.60\text{g}/\text{cm}^3$.

“It doesn’t matter how beautiful your theory is, it doesn’t matter how smart you are. If it doesn’t agree with experiment, it’s wrong.”

Richard P. Feynman.

3

Experimental

In this chapter the experimental work with the NMR equipment as well as the different details of cell preparation are discussed. Ideas to improve the microelectronic performance of the microcoil setup are presented. Here first prototypes which were not tested systematically are shown.

The detailed standard process of preparing the Leipzig NMR anvil cells and building the microcoils is described elsewhere [45,44,100](#)

3.1 SPECTROMETER AND MAGNET

The two used magnets, *Ascend 500 WB*, made by the *Bruker Corporation*, which have a magnetic flux density of 11.74 T. The magnetic field generated by high currents circulating in superconducting coils inside a cryostatic setup, which is cooled by liquid helium. Two spectrometers, *AVANCE III HD* from the *Bruker Corporation*, were used for the measurements. The program *Top Spin 3.5.7* offers an easy user interface. The amplifier supplies 500 W of power which is damped to the needed by a damping element. The pulse from the amplifier goes through the damping element along a matched signal line, passing a coupler, reaching the probehead. Then the coupler switches to the detection line.

3.2 EVALUATION OF THE MEASURED SIGNALS

For the evaluation of the measured data the Windows software *Origin Pro 7.5* from *Origin-Lab Corporations*, including the extension ONMR for NMR data, was used. *Origin* allows an analysis of measured signals in time domain, as well as a numerical 'Fourier Transformation' tool to extend the analysis to the frequency domain. Further a curve fitting tool is integrated which is based on a nonlinear least squares fitter based on the Leven-Marquardt algorithm. The Peak analysis tool allows an easy determination of intensity relations of peak to noise ratios. All plots and data shown in this work are prepared by using this program.

Some optical issues were processed with *Inkscape* afterwards. *Inkscape* is a vector graphic editor from the open source supplier GNU for graphical editing and creation of scalable vector images.

3.3 MICRO ELECTRONICS

In this section some improvements of the anvil cell design from daily routine are shown and discussed. Unfortunately no more detailed investigations could be done, for example a systematic series of measurements of the tested designs to make a clear scientific evaluation possible.

3.3.1 IMPROVEMENTS OF THE SET UP

The basic idea to improve the performance of NMR set up is to reduce parasitic elements in the circuit. The first step is a reduction of the resistance of the circuit and with this it's damping, which increases the Q-factor. The second step focusing of inductive and capacitive elements to the sample chamber to reduce parasitic effects of cables, wires, couplers etc.

GUIDE PINS MADE FROM SILVER

I removed the old brass guide pins for the gasket and exchanged them for a silver wire of the same diameter. Several methods were tested to improve the conductivity between the silver pins and the titanium cell body. The attempt with silver epoxy paste for the connection did not lead to the lowest resistance. The lowest resistance was reached with five steps.

1. grinding the silver pins surface, to generate a rough surface and remove possible surface oxidation.
2. grinding the guide pin holes from the inside by using a drill
3. putting a very small amount of solder inside the hole and stuff it to the bottom with the silver guide pin
4. putting the cell body with the guide pins in the holes and the solder below in the oven and heating it up to 250 °C for 20 minutes.
5. after the heating in the oven the solder iron is placed on the top of every guide pin for at least 1 minute

Before heating up the cell the anvils should be removed, because heat effects, like the difference of expansion of the different materials, could damage the anvils. A reduction of

the resistance between cell body and guide pin from $1.2 - 1.5 \Omega$ to $0.2 - 0.3 \Omega$ could thereby be reached.

For the future better contact would be possible by using a screw thread at the lower tip of the silver wire and the titanium guide pin hole. This would increase the contact surface dramatically, which leads to a better electrical contact.

GROUNDING PLATE

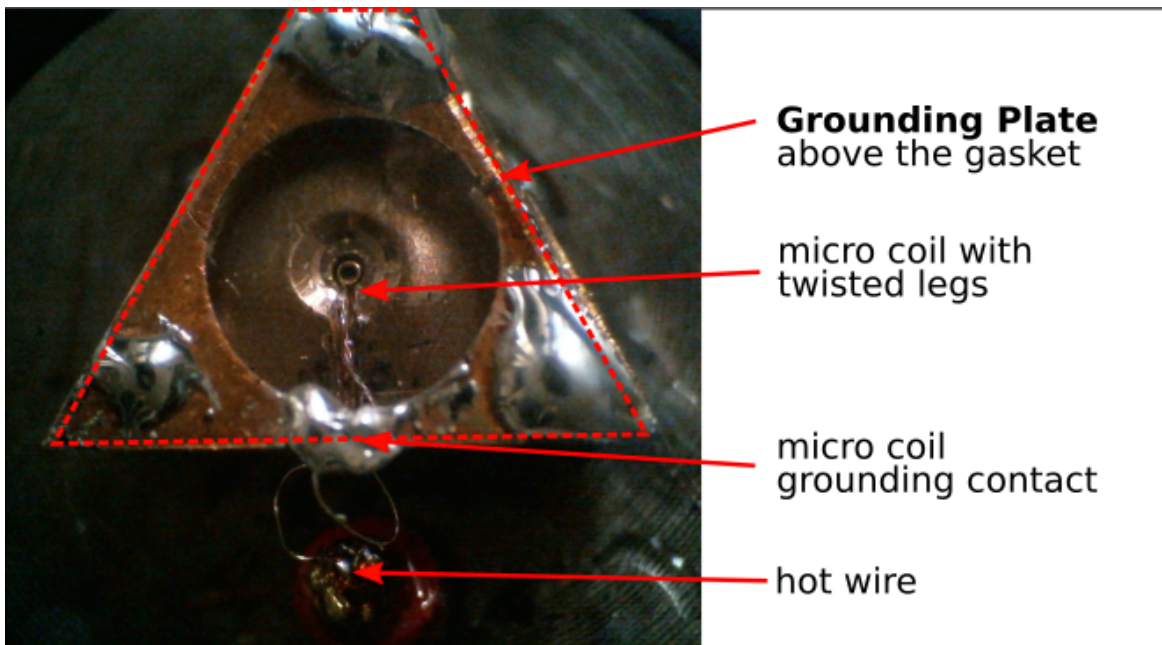


Figure 3.1: **Picture of the grounding plate:** One can see the grounding plate above the gasket. In the gasket hole a microcoil with twisted legs is placed. The connections of the coil's legs allow a parallel wire course and with this twisted legs.

The grounding plate (see Fig. 3.1) was added to realize a reduction of the effective resistance of one guide pin by three guide pins in parallel.

$$R_{total} = \frac{R_1 R_2 R_3}{R_1 R_2 + R_1 R_3 + R_2 R_3} \quad (3.1)$$

For $R_1 = R_2 = R_3 = 0.3 \Omega$ it results in $R_{total} = 0.1 \Omega$.

Further it allowed a reduction of the leg length and a parallel or twisted course of wires from the hot wire to the cell chamber and back to the grounding plate. Of course the resistance of the added ground plate also contributes to the total resistance.

TWISTED LEGS

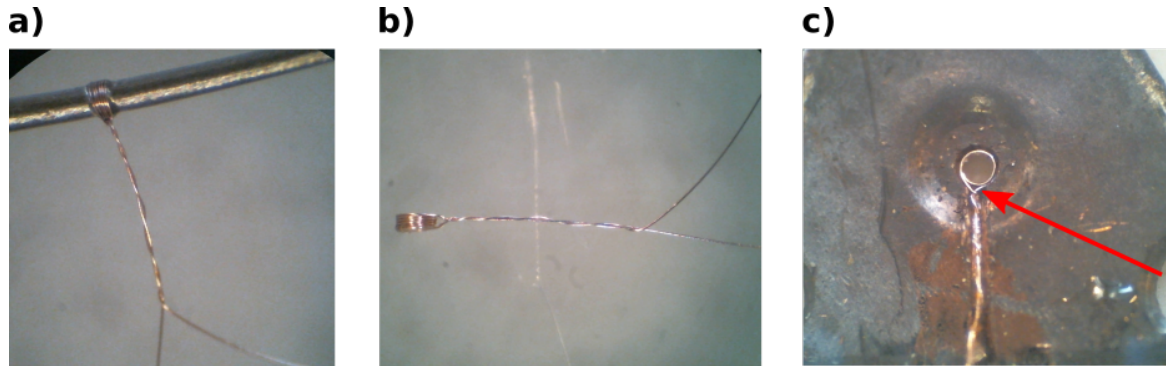


Figure 3.2: **Coils with twisted legs:** a) a coil with twisted legs on awl b) a coil with twisted legs removed from the awl c) a coil with twisted legs in side the the gasket hole, which create with the anvils the sample chamber. The red arrow marks the weakest point were a possible short circuit most likely appears due to the deformation of the gasket

The effect of twisted pair cable to reduce the inductance and the influence from outer interference has been known for long time¹⁸. The two relatively long legs of the used coil, compared to the diameter of the winding, lead to a large influence of the course of these leg wires. If they are perfectly parallel the inductivity should be canceled and have the smallest parasitic effect.

To have a fixed value close to zero the concept of twisted legs was tested. This led to a reduction of the hole inductance of the circuit, which shows the large parasitic effect of the legs. An other advantage of twisted legs is that only one channel is needed to reach the coil. But here is also the problem. Due to the deformations of the gasket, and with this the deformations of the channel, containing the two twisted wires, the legs can cause a short circuit inside the channel (see Fig. 3.2 c)). At ambient conditions very good values were reached, but by applying pressure the signal was lost quickly even at low pressures. The result was that two channels were scratched inside the pressure region and both lead into a combined channel outside the pressure region, where the legs are twisted.

3.3.2 SPECIAL COIL DESIGN

ELLIPTICAL COILS

The preparation of elliptical microcoils was necessary to increase the filling factor, due to the extremely flat micro crystals which had to be placed upright in the chamber.

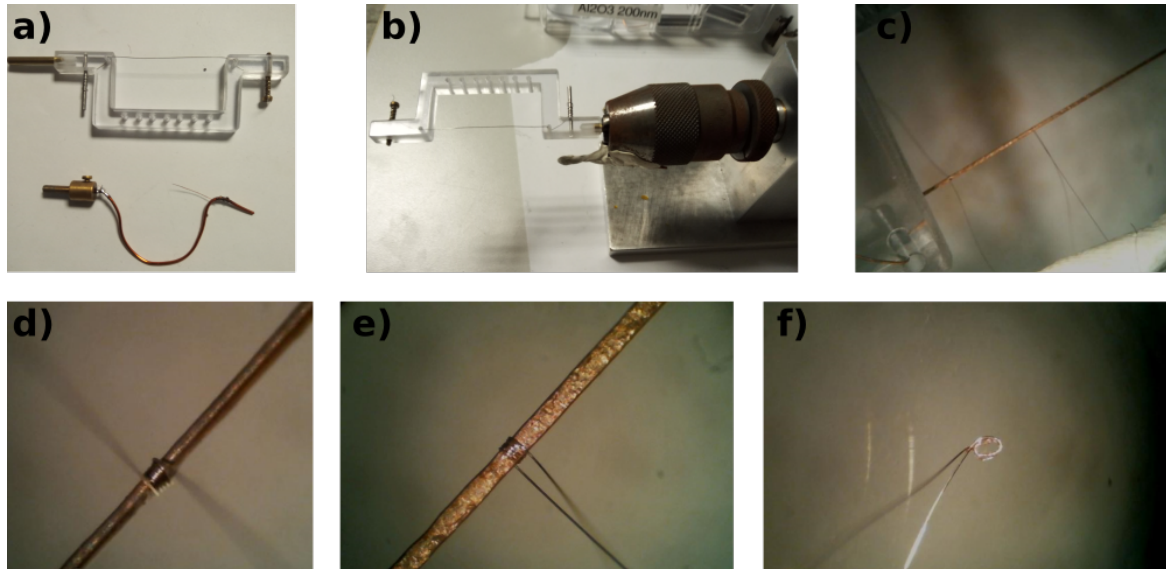


Figure 3.3: **Pictures of the preparation of elliptical coil:** a) shows the two used winding frame for the flat wires. At the top is the one which was produced by the workshop, below is the first draft made of an copper wire with a large diameter b) Here one can see the winding frame fixed in the drill chucks, which allows the rotation of the winding frame c) shows zoom in cut out of the micro wires wounded around the flat wire d) shows one axis of the cross section e) shows the other axis of the cross section f) one can see the finished elliptical coil

To generate an bradawl with an elliptical cross-section, different wires were tested, pressing them flat with different amounts of force, so different a and b radius of the ellipsis were formed. The initial wire used finally had a diameter $100\ \mu\text{m}$ and was pressed to $a \approx 70\ \mu\text{m}$ and $b \approx 130\ \mu\text{m}$ see Fig. 3.3 d) and e). This bradawl was now tightened in the winding frame (See Fig. 3.3 a)- c)), which allowed a free rotation. To wind the microcoil the silver wire with a diameter of $25\ \mu\text{m}$ and $5\ \mu\text{m}$ insulation was wound around the bradawl. Its shape was fixed with cold temperature varnish. The most difficult part is to remove the microcoil from the not perfectly smooth surface of the self-made bradawl. Silicon spray was found to help to reduce the friction.

3.3.3 NEW COIL FOR THE Y-6.50 CELL (MC-2 BETA CELL)

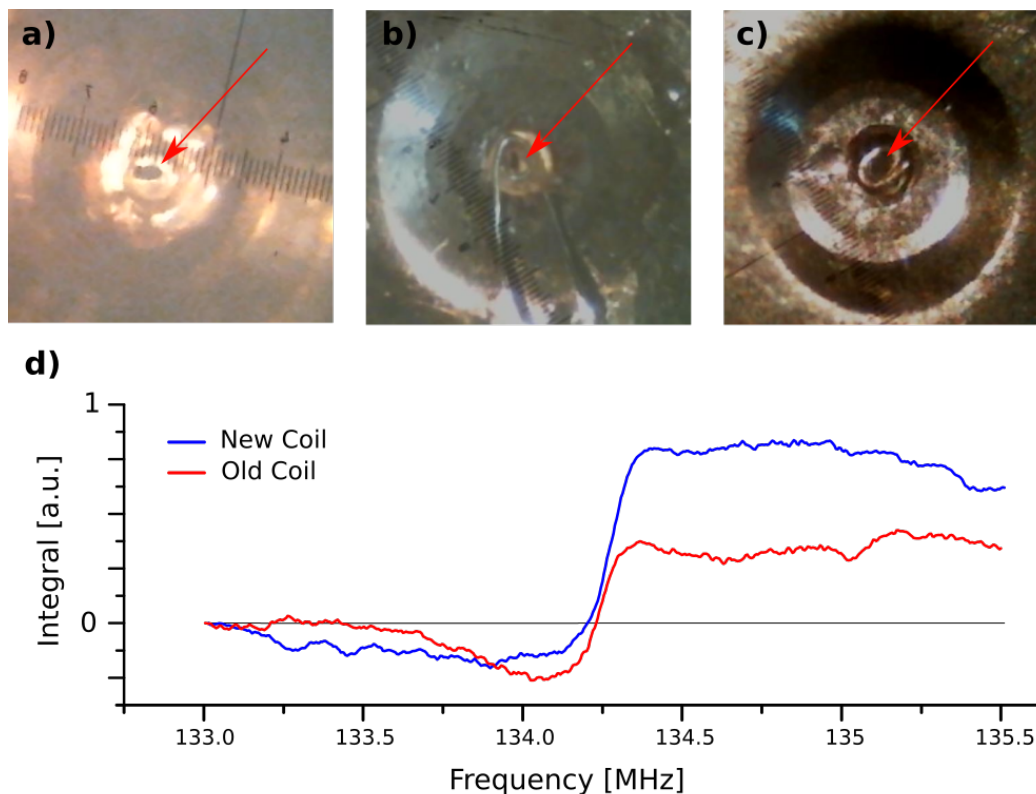


Figure 3.4: **Cylindrical coil vs. elliptical coil:** **a)** shows the first coil for the Y-6.5 cell (MC-2-Beta cell), a cylindrical coil. Due to the very flat crystal the filling factor was only about 8 % **b)** shows the new elliptical coil from above and **c)** from below. Using an elliptical coil increased the filling factor to about 13%. The red arrows point to the very small crystal. **d)** Here the compare of the integrals in frequency domain of the old cylindrical coil and the new elliptical coil is shown.

Due to the extremely flat micro crystal MC-2 Beta ($40 \times 40 \times 90 \mu m^3$) the realized filling factor using a cylindrical coil was only 0.077 (see Fig. 3.4 a)). To increase this filling factor and with this the SNR a method to prepare elliptical microcoils was developed. In Fig. 3.4 b) and c) one can see the elliptical microcoil from both sides of the gasket. The filling factor was increased by almost the factor of two from 0.077 to 0.129.

The SNR of the old coil of ^{63}Cu in c direction was ≈ 0.004 , for the new coil it was increased to ≈ 0.007 . The difference is very clear with the graphic shown in Fig. 3.4 d), which shows the integral in the frequency domain of the new coil.

DOUBLE WOUND MICROCOILS

The idea of a double wound coil came up to increase the inductance to be able to tune the probe easier to the low oxygen frequencies. This was tested in the Y-6.85 cell.

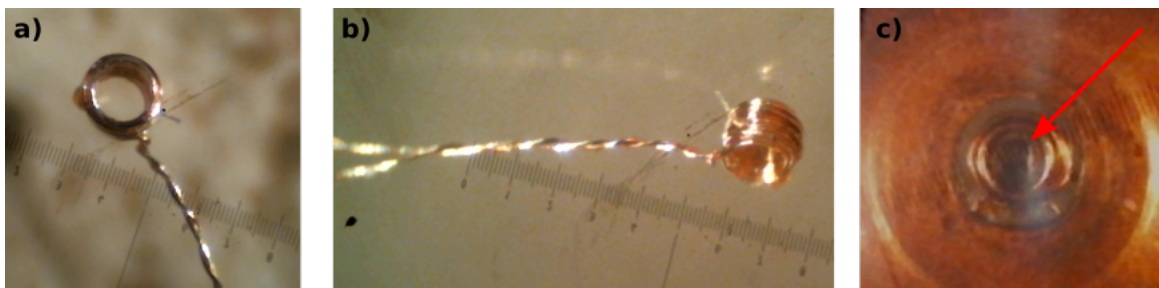


Figure 3.5: **Double wound coils:** with twisted legs **a)** from the top, **b)** from the side and **c)** inside the cell from the bottom view the red arrow marks the single crystal Y-6.85 (twisted legs were not used for the measurements)

In Fig. 3.5 a) and b) one can see a double wound microcoil with twisted legs. In Fig. 3.5 c) the double wound coil is placed in the sample chamber of the anvil cell. For the final measurement setup the twisted leg technique was not used.

3.4 SUMMARY OF THE CHAPTER

In this chapter the setup is presented in more detail. The magnet, spectrometer as well as the software for the analysis is introduced. Then some prototypes are presented where ideas to improve the performance were realized. It was possible to show that a double wound microcoil, an elliptic microcoil as well as twisted legs of these coils are possible to build by the hand under a microscope.

An increase of the Q-factor was achieved by improving the grounding of the guide pins by replacing the old brass pins with silver pins and solder them to the titan cell body. An additional use of a grounding plate above the gasket to connect all three guide pins parallel allowed to reduce the length of the legs as well as an improved grounding.

The first analysis of the twisted legs design were very positive in term of NMR performance. Unfortunately the twisted legs tend to create a short circuit, if the twisted pair is placed in only one channel due to the strong deformations. A compromise was found using two channels inside the high pressure region and twisting the legs before connecting to the hot wire and the grounding contact.

With a somewhat complicated procedure it was possible to build an elliptic microcoil which increases the filling factor for very flat microcrystals and with this the signal of the Y-6.5 cell.

A double wound microcoil was realized to shift the tuning range of the circuit to lower frequencies by increasing the inductance of the coil. The frequencies of the oxygen transitions were reached. Unfortunately no further systematic investigations of the designs was performed.

*“Measure everything that can be measured - and
make measurable that which is not yet measur-
able”*

Galileo Galilei

4

Sample Chamber Monitoring for single crystal NMR in high pressure cells

The basic principles and the measurements of the sample chamber’s dimensions are presented in this section. First, the basics of height measurements, the arrangement of the anvils and the idea behind is explained. The second part, considers the measurements of the diameter and the transverse movement of the gasket material. In the third part, a discussion according to the ‘Theory of the Gasket’ by D.J. Dunstan⁵⁰ is presented. Finally the volume determination, the compressability and an error discussion is given.

The data presented in this section are published in the journal “Review of Scientific Instruments”¹⁰⁹ in 2021.

4.1 NECESSITY OF SAMPLE CHAMBER MONITORING

When pressure is increased, the sample chamber of an anvil cell runs through an extreme deformation. This deformation is described theoretically by D.J. Dunstan⁵⁰. It is described in the theory part of this work as well (sec. 1.3.4).

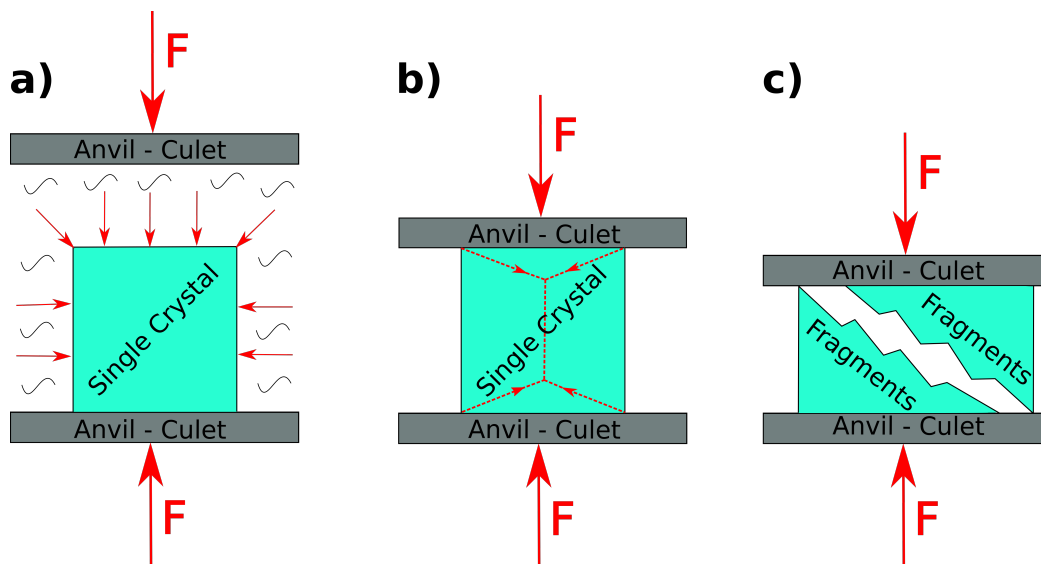


Figure 4.1: **Crystal between two anvils:** a) The single crystal is in hydrostatic conditions the distance of the culet surfaces of the anvils is larger than the height of the single crystal. b) The culet surfaces of the anvils has contact with the crystals edges and pressurizes it uniaxial, causing tensions inside the crystal. c) The anvils broke the single crystals, it is not possible to do the orientation of the crystal fragments

At single crystal experiments under high pressure, the dimensions especially the height of the sample chamber is a limiting factor during the pressure increase. If the chamber height is larger than the crystal height, and the conditions for the pressure medium are fulfilled^{51,52,53}, in this case paraffin oil (see sec. 1.3.5), we assume the conditions to be hydrostatic. With a decreasing height of the sample chamber, near or below the single crystal's height, the crystal could be pressurized uniaxial or even break. (see Fig. 4.1)

The presented method is essential to push high pressure single crystal NMR measurements to its limits.

4.2 MEASUREMENTS

4.2.1 MEASURE THE HEIGHT OF A SAMPLE CHAMBER

Some works propose^{110,111,112}, a measurement of the height of the sample chamber by measuring two reference points at the anvils. Following this idea, an optically clearly detectable edge between two of the anvils surface can act as visible reference under a microscope. In Fig. 4.2, the visible edges at the anvils are marked. The deformation of the anvils in the considered pressure range is small¹¹³ and is neglect in this thesis.

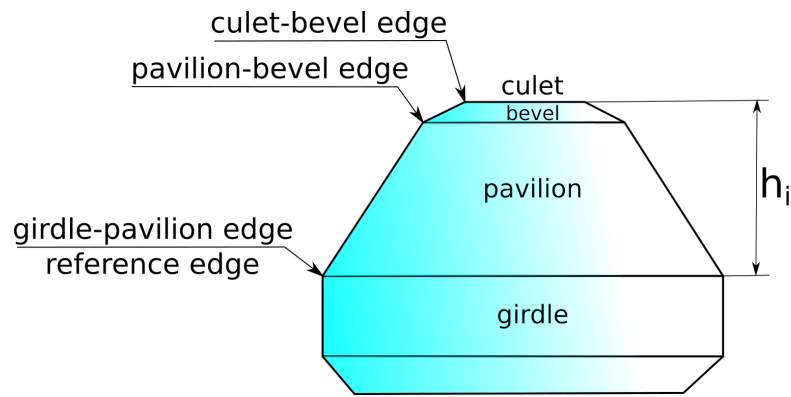


Figure 4.2: **Reference edges of an anvil:** The visible edges at the used anvils are marked. The height h_i gives the orthogonal distance between the culet-bevel edge and the girdle-pavilion edge of the anvil i .

To measure the orthogonal heights of the anvils the distance between the girdle-pavilion edge and the culet-bevel edge was measured. (see Fig. 4.2)

The height measurements of h_i were done from three different angles at 120° distance to one another, the average of the three values was defined as height h_i . The whole process was done while the anvils were already fixed in the seats of the cells, which allowed reproduceable angles according to the cells orientation.

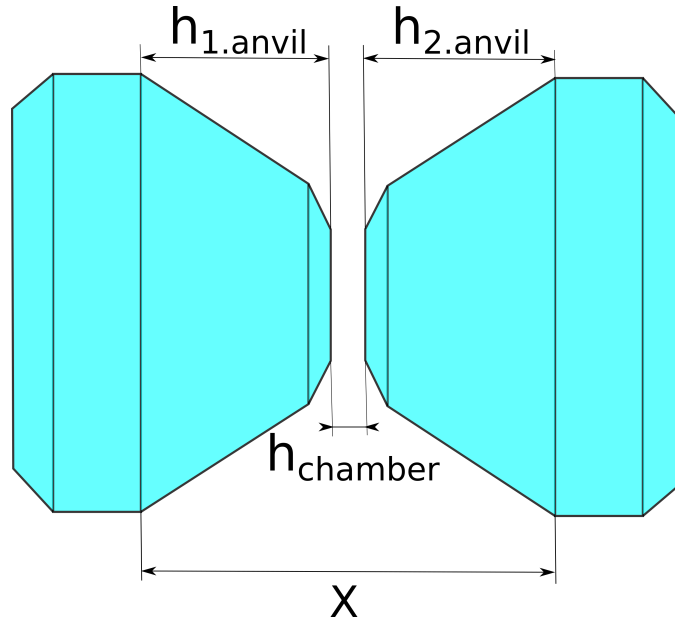


Figure 4.3: **Concept of height measurements:** Optical visualization of equation (eq. 4.1). By measuring X the distance between the two reference edges, the height h_{chamber} can be calculated if the heights of the anvils $h_{1.\text{anvil}}$ and $h_{2.\text{anvil}}$ are known.

If the heights $h_{1.\text{anvil}}$ and $h_{2.\text{anvil}}$ of two opposed anvils are known, the height of the sample chamber which is effectively the distance between the two culet surfaces, can be calculated by measuring the distance of the reference edges and deduct the two anvil heights. This is pictured in Fig. 4.3.

$$h_{\text{chamber}} = X - h_{1.\text{anvil}} - h_{2.\text{anvil}} \quad (4.1)$$

The experimental procedure of measuring the anvils and measuring the height of the chamber was performed using a Toshiba digital microscope equipped with a piezo controlled movable sample table. This table allowed a focusing on one reference edge and a movement over several millimeters in a precision of $\pm 2.5 \mu\text{m}$ to an other reference edge. An overview photo is given in Fig. 4.4 a) and b). For the final measurements a much higher zoom level was used.

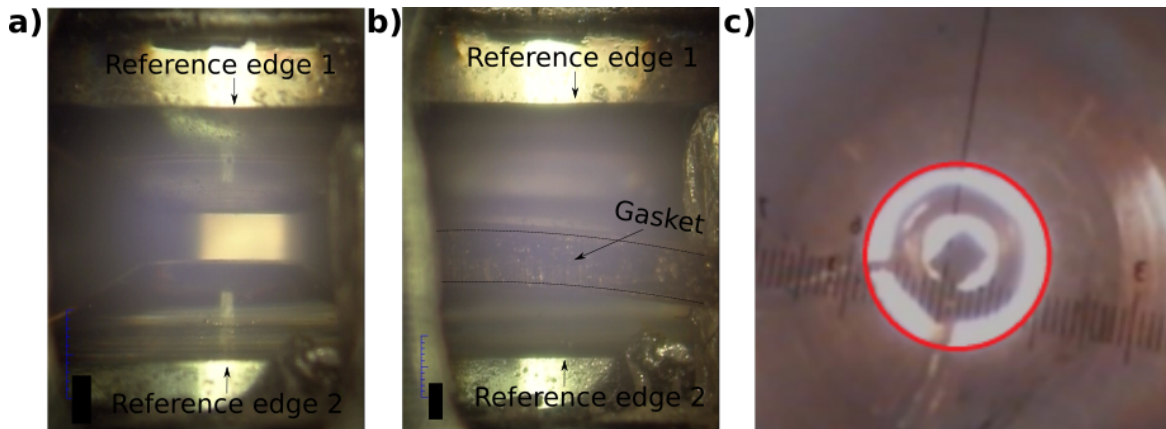


Figure 4.4: **Pictures of the anvils under the microscope:** a) Shows the two opposed anvils with out a gasket in between. b) Show the same anvils with a gasket in between, the reference edges remain visible and can be used to measure the chamber height. c) Measurement of the diameter of the sample chamber, first the red circle was fitted to the photo then the diameter was measured by the reference of the gauged scale in the microscope. Also the microcoil and the micro crystal can be seen here. This photo shows the Y-6.85 cell at a pressure of 5 GPa. (The final measurement was done with a higher zoom level.

4.2.2 HOW TO MEASURE THE DIAMETER

To measure the diameter, a photo was taken by a camera fitted onto the ocular of the microscope. Additionally a measuring scale plate was added in this ocular. This scale was gauged for the different zoom levels. In Fig. 4.4 c) an example for such a photo is shown. The photos were taken through the transparent anvils which allowed a view in the sample chamber. For the evaluation a red circle was fitted to the chambers edge. Then the diameter of this circle was measured. For the evaluation the radius was calculate by the diameter.

4.2.3 RESULTS OF THE HEIGHT AND DIAMETER MEASUREMENTS

In this section the measured values are presented, for more details of the theoretical background please check the sec. 1.3.4.

Y-6.85 CELL (ALPHACELL) AND Y-6.5 CELL (BETACELL)

In Fig. 4.5 the relevant parameters, the radius $r_g(p)$ in blue, as well as the values for the height $h(p)$ in red, of the sample chambers depending of the pressure for the Y-6.85 cell and the Y-6.5 cell are shown.

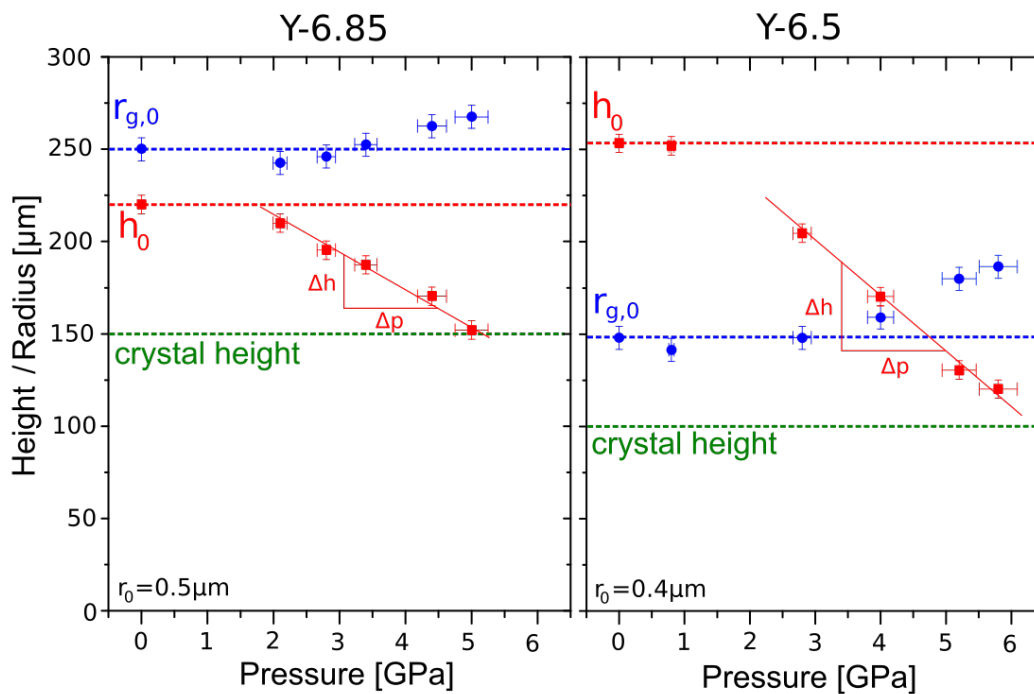


Figure 4.5: **Height and radius measurements:** Left for Y-6.85 cell and right for the Y-6.5 cell. The red squares show the measured values for the sample chambers height, the blue circles show the measured radius. The green dashed lines mark the crystal heights. The red lines depicts a linear function with a slope triangle $\Delta h/\Delta p$. $r_{g,0}$ is the initial radius, h_0 is the initial height and r_0 is the radius of the used culet. The slope triangle for height reduction of the Y-6.85 cell is $-22.1 \mu\text{m}/\text{GPa}$. The slope triangle for Y-6.5 cell is $-32.96 \mu\text{m}/\text{GPa}$

While $h(p)$ and $r_g(p)$ are the chambers height and radius depending on the pressure p , h_0 and $r_{g,0}$ are the initial height and initial radius of the sample chamber measured at ambient

conditions before the pressure is increased. The crystal height is marked in green. For low pressures (below < 2 GPa) only a very small decrease of the the height is noted. This can be seen more clearly for the Y-6.5 cell at 0.9 GPa. For the values at higher pressures (above > 2 GPa) a decrease in height and an increase of the radius above the initial is clearly observed for both cells. A clear boarder between the *thin* and *thick*- gasket regimes is not observed. The transition between the regimes for these architectures occurs fluent around 2 GPa. For both cells one can see a decrease of the height above 2 GPa. A line was put through the height values for elevated pressures. The lines give the slope $\Delta h/\Delta p = -22.1 \mu\text{m}/\text{GPa}$ for the Y-6.85 cell and $-32.96 \mu\text{m}/\text{GPa}$ for the Y-6.5 cell.

The ratio $r_0/h(p)$ as well as the ratio $(r_0 - r_g(p))/h(p)$ are considered by literature^{39,50} as characteristic (sec. 1.3.4) . These ratios influence the behavior of the gasket under pressure mainly, and can be set easily by the preparation process.

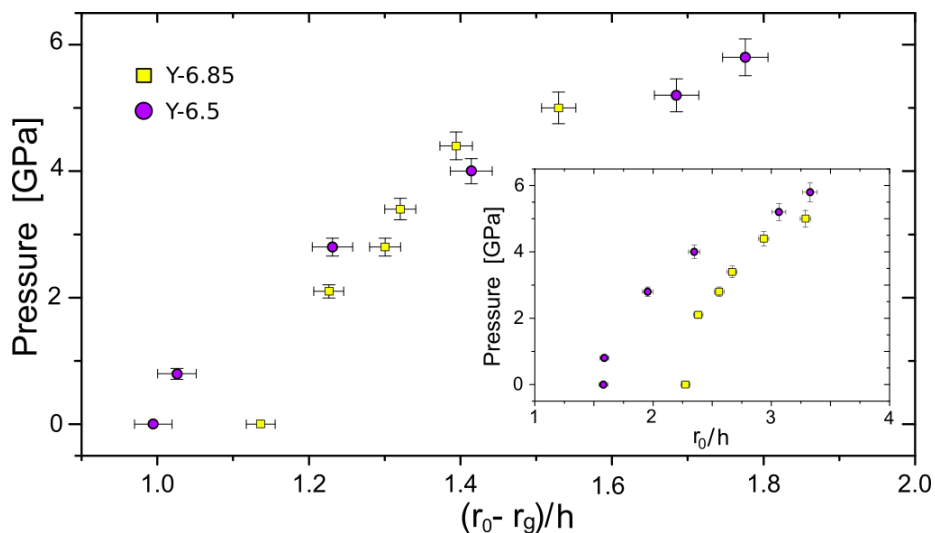


Figure 4.6: **Cell parameters depending on pressure:** The measured pressure (p) inside the gasket is depicted as function of the cell parameters, r_0 is the radius of the culet, $r_g(p)$ is the radius of the chamber depending on the pressure, $h(p)$ is the height of the chamber depending on the pressure. $(r_0 - r_g(p))/h(p)$ is shown in the main panel, $r_0/h(p)$ is shown in the inset

By comparing the ratio of the initial radius of the hole in the gasket $r_{g,0}$ with the initial height of the chamber h_0 , one will see, the initial shaped cylinder of the Y-6.85 cell ($r_{g,0}/h_0 = 1.13$) is initially a much flatter cylinder then in the Y-6.5 cell ($r_{g,0}/h_0 = 0.59$). While the radius for Y-6.85 cell is larger then the height, the radius for the Y-6.5 cell is smaller then the height (see Fig. 4.5).

The ratio between $r_{g,0}$ and r_0 , for the Y-6.85 cell is $r_{g,0}/r_0 = 0.5$ and $r_{g,0}/r_0 = 0.375$ for the Y-6.5 cell. This ratio influences the transition between the *thin* and *thick*-gasket regimes. A gasket with a larger value for the ratio, has a larger hole radius proportional to the culet radius, and will reach the pressure of extruding the material only, the *thick*-gasket regime, earlier^{39,50}.

So if we want to increase the range of the *thin* - gasket regime further to have more stability while pressure is increased one should build the cell with that in mind: A large culet radius r_0 stabilizes the architecture and the flow behavior. And a gasket hole should be small, better is 1/3 of the initial radius r_0 then 1/2³⁹.

In Fig. 4.6 the pressure is plotted over the ratio $(r_0 - r_g(p))/h(p)$ in the main panel. A generic behavior is found for the higher pressure values. A linear slope of 7 GPa was determined, which appears too large for the sticking regime of the gasket (CuBe) between the anvils (6H-SiC). This large value could be explained by a large friction coefficient $\mu \approx 0.5$ which is unknown as well as the unknown massive support factor which also influences the system.

The inset of Fig.4.6 shows the ratio $r_0/h(p)$. The initial ratio for the Y-6.85 cell is 2.27 and goes up to 3.29 at 5 GPa. For the Y-6.5 cell it goes from 1.58 to 3.35 at 5.8 GPa.

4.2.4 VOLUME DETERMINATION, COMPRESSABILITY OF PARAFIN OIL

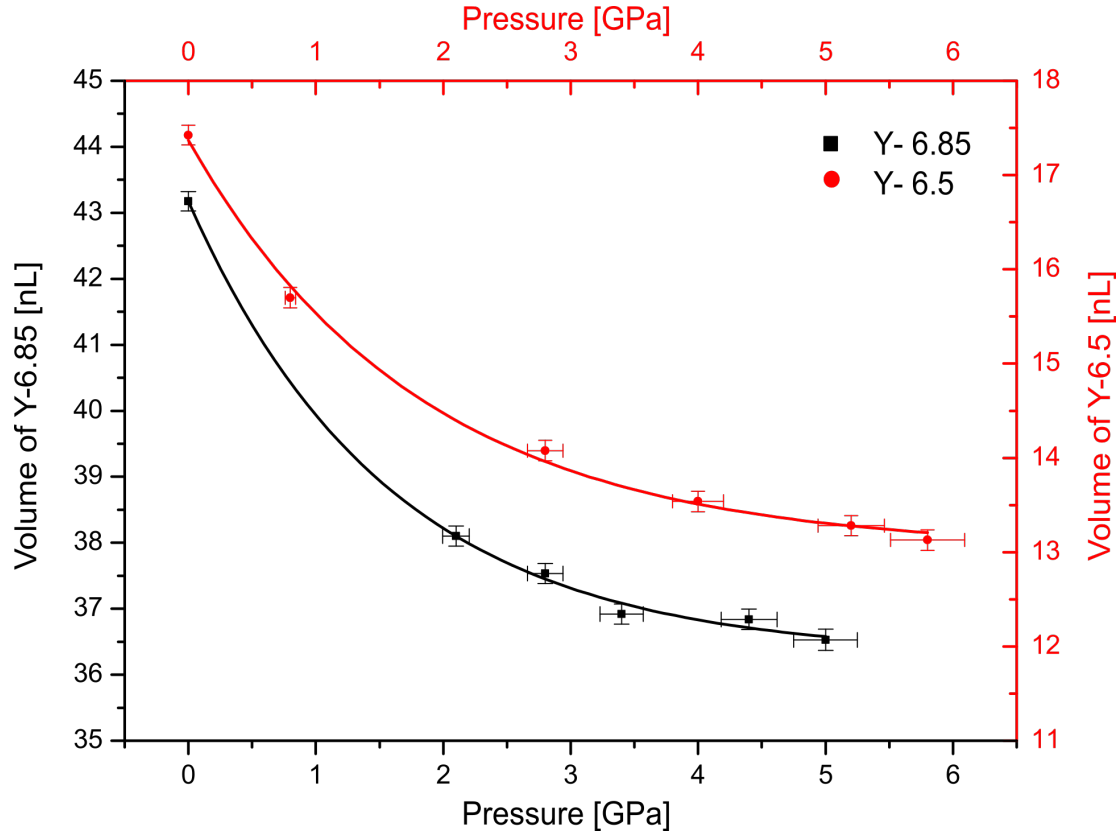


Figure 4.7: **Volume of Y-6.85 cell and Y-6.50 cell:** The black squares depicts the volume of the Y-6.85 cell. The black line is a exponential fit function with and decay coefficient of $\kappa_{Y-6.85}=1.4703$. The red circles depicts the volume of the Y-6.50 cell. The red line is an exponential fit function with and decay coefficient of $\kappa_{Y-6.5}=1.4923$

To be able to calculate the volume of the sample chamber the shape was approximated as being cylindrical. By knowing the height and the diameter the common formula for a cylinder's volume $V(p) = \pi \cdot r(p)^2 \cdot h(p)$ was calculated at every pressure point. Then the fit function (eq. 1.31) given in sec. 1.3.5 was used to determine the bulk modulus.

Here paraffin oil is the dominant material inside the sample chamber, only a small fraction of the volume is occupied with the volume of the single crystal of $\text{YBa}_2\text{Cu}_3\text{O}_{7-x}$. In Fig. 4.7 the volume reduction of the sample chamber is shown for the Y-6.85 cell as well as for the Y-6.5 cell. The bulk modulus for the Y-6.85 cell is $\kappa_{Y-6.85} = 1.4703$, for the Y-6.5 cell it is $\kappa_{Y-6.5} = 1.4923$. This is in good agreement with the values for air free mineral oil ($\kappa = 1.4 - 1.6 \cdot 10^4$ bar) from literature⁵⁴.

4.3 ERROR CONSIDERATION

Here a brief consideration about the uncertainties of the measurements and the volume determination of this method to monitor the sample chamber in a high pressure NMR cell is given. The biggest uncertainties are the reading errors at the measurements of the height and the diameter. Further a failure propagation for the calculated values of volume is presented. The numerical failures from the plot functions are much smaller and are not considered here.

UNCERTAINTY OF THE HEIGHT MEASUREMENT

The precision of the measuring process with the piezo controlled table is considered as $\pm 2.5 \mu\text{m}$.

UNCERTAINTY OF THE DIAMETER MEASUREMENT

The diameter is measured by a picture taken through a microscopes ocular. Then the fitted circle is measured by the scale in the ocular, then the values is divided by two to get the radius. A realistic failure for this method is assumed as $\pm 7.5 \mu\text{m}$.

UNCERTAINTY OF THE VOLUME DETERMINATION

To calculate the failure of the volume determination a failure propagation was implemented. Due to the formula of the cylinders volume the resulting failure of a failure propagation is $\frac{\Delta V}{V} = 2 \cdot \frac{\Delta d}{d} + \frac{\Delta h}{h}$. For example this results in a failure for the volume of $\pm 0.63 \text{ nl}$ at the pressure of 2.8 GPa. All failures are depicted in the Fig. 4.7.

UNCERTAINTY OF THE PRESSURE DETERMINATION

The uncertainty of the pressure determination up to 10 GPa is given by $> 5\%$ of the measured pressure^{33,40}.

DEFORMATION OF THE ANVILS

The deformation of the anvils in this pressure range is below $\pm 1 \mu\text{m}$ ¹¹³

4.4 DISCUSSION

Previous works^{110,111,112} showed the possibility of measuring the distance of the anvils by measuring the distance of two reference points. The method using a piezo controlled table presented here to measure the height of the sample chamber is new. Here we used the edges between the surfaces of the anvils which are optically clearly focus able as reference edge. Additional diameter measurements allowed a determination of the volume which was done before by L. N. Dzhavadov¹¹² for helium. We show the compressability of paraffin oil.

Furthermore our data show that the pressure dependent ratio $(r_0 - r_g(p))/h(p)$ sets the final pressure if the chamber's height shall not go below the crystal's height, were the crystal would be pressurized uniaxial.

If this knowledge is used for the high pressure NMR cell preparation for single crystals, higher pressures should be reachable. Never forgetting the limit which is set by the tensile strength of the gasket material, CuBe in this case. But the recognition that a larger culet provides more stability of the sample chamber, which is necessary for single crystal measurements and the possibility to monitor the chambers dimensions are very important for the planning of high pressure NMR anvil cells for single crystals in the future.

“The combined results of several people working together is often much more effective than could be that of an individual scientist working alone.”

John Bardeen

5

Single Crystal NMR of $\text{YBa}_2\text{Cu}_3\text{O}_{6+y}$ up to 4.4 GPa

In this chapter the measured data of two NMR anvil cells, equipped with two differently doped single crystals, are presented and discussed.

First, measurements of the critical temperature for both cells Y-6.85 and Y-6.5 are shown, explained and compared to literature data to determine the doping content. Next the orientation of a $\text{YBa}_2\text{Cu}_3\text{O}_{6+y}$ single crystal in a magnetic field, depending on the second order frequency shift of the central transition is shown. Then the measured changes with pressure of the quadrupole frequencies and the calculated charges, are shown and discussed in terms of the $2n_{\text{O}}-n_{\text{Cu}}$ -plane.

The data presented in this section are under review and are published in arXiv¹¹⁴

5.1 DOPING LEVEL AND THE CRITICAL TEMPERATURE

5.1.1 T_c MEASUREMENT

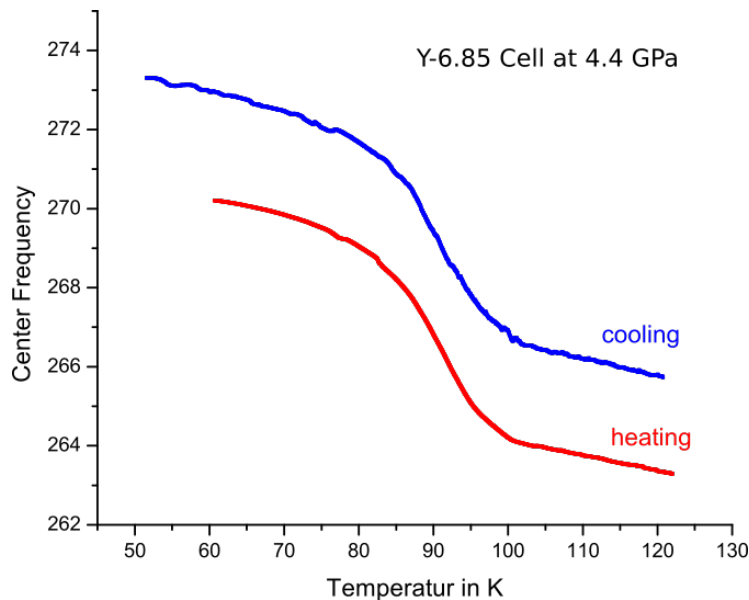


Figure 5.1: **Temperature response of the circuit:** In this figure the temperature dependent change of the center frequency of the resonant circuit is shown. The diamagnetic transition of the superconductor changes the inductance of the micro coil containing the high- T_c sample. This example curve was recorded with the Y-6.85 cell at 4.4 GPa.

In section 2.1.5 the dome like behavior of T_c from doping as well as from pressure is discussed. In Fig. 2.3 b) in section 2.1.5 the pressure dependency or differently doped samples is shown⁸.

It is possible to determine the doping content by measuring the critical temperature at ambient pressure⁹. Using the Meissner effect, the change of a superconductors susceptibility below the critical temperature, and with this the inductance change of a coil containing the sample is a practical tool for the determination of T_c in an NMR anvil cell. This method was used by different groups in the past^{115,116,117}. The superconducting transition is accompanied by a sharp change of the magnetic susceptibility $\chi(T)$ of the crystal. The inductance of the microcoil can be described by $L = L_0(1 + \rho\chi(T))$, were L_0 is the inductance of the empty coil and ρ is a factor which is influenced by different parameters like the filling factor, the anisotropic penetration depth in a RF field and others. Furthermore the proportionality between $\chi(T)$ and the inverse square of the resonance frequency f_R^{-2}

allows the determination of T_c ⁹.

The process itself was simple. The cell was cooled down with a cryostat in zero field conditions to around 120 K, so above the critical temperature. The circuit was tuned and matched at around 250 MHz. A Hameg spectrum analyzer was used to obtain the frequency response. A Lakeshore 332 module was used to drive a defined temperature sweep ramp to a temperature of 50 K, well below the critical temperature. With a python program the resonance frequency of the circuit f_R was plotted over the temperature (see Fig. 5.1).

Depending on the heat capacity of the probehead and the cell, which surround the sample, a hysteresis between heating and cooling occurred. The temperature sweep rate influences this effect dominantly. For very fast heating and cooling rates the hysteresis is large. So these experiments were done with very low temperature sweeping rates of ≈ 0.1 K/min. The definition for T_c as upper temperature, where about 10% of the frequency shift occurred was used⁹. An example of such an measurement is shown in Fig. 5.1.

Above and below the superconducting jump the change rate of the center frequency is equal depending on the temperature response of the circuits components. Considering the derivation of these functions reveals the inset very clearly. This is shown in the next section, for the Y-6.85 cell and the Y-6.5 cell.

Y-6.85 (MC-2 ALPHA CELL)

The derivative of the cooling curve shows most clearly the inset of the superconducting transition. The constant change, which is an offset in the derivation was subtracted. This is shown in Fig. 5.2 for the Y-6.85 cell.

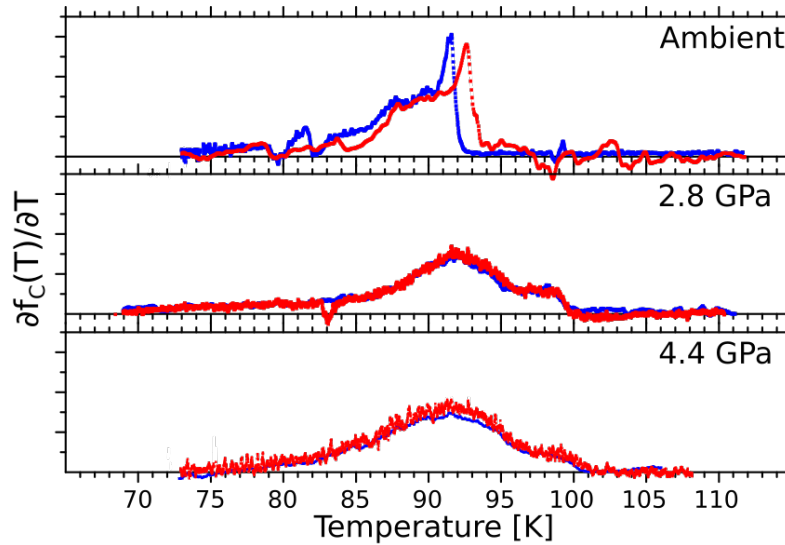


Figure 5.2: **Derivative of the temperature dependent center frequency Y-6.85:** The derivative of the circuits center frequency of the Y-6.85 cell is shown. Blue for a cooling process. Red for heating. The aberration of the position at ambient conditions is caused by a too fast sweeping rate, which was reduced for the following measurements. The change of shape between the different pressures can be attributed to doping inhomogeneties which induce a little variation in the pressure response.

The hysteresis at ambient condition comes from a high temperature sweeping rate. For higher pressures it was reduced so almost no hysteresis appears. Further one can see the changes of the inset areas differ for different pressures. At ambient pressure the change is much steeper then at higher pressures. The change of the shapes can be attributed to doping inhomogeneties which produce a wider variation of responses if pressure is increased. 10% of the frequency change was reached at ambient conditions at a temperature of 92 K. At a pressure of 2.8 GPa the critical temperature is 96 K and at 4.4 GPa a decrease was seen again to 93 K. A summary of the values are presented in Fig. 5.4.

Y-6.50 (MC-2 BETA CELL)

The derivative of the cooling curve shows most clearly the inset of the superconducting transition. This is shown in Fig. 5.3 for the Y-6.5 cell.

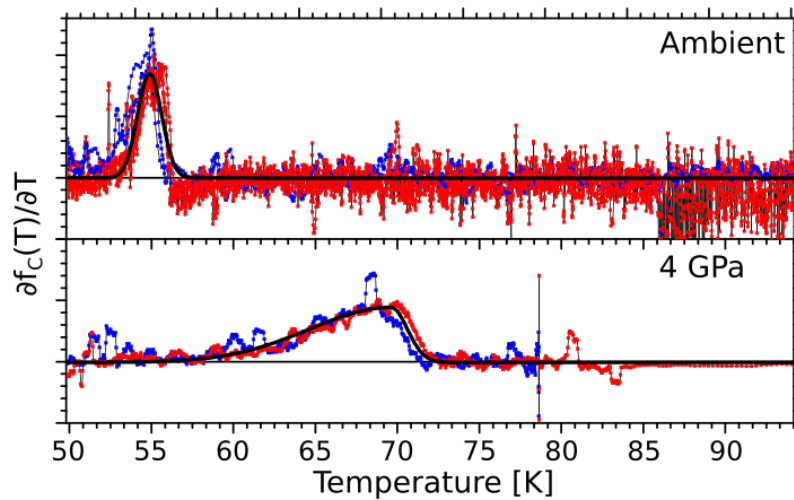


Figure 5.3: **Derivative of the temperature dependent center Frequency Y-6.5:** The derivative of the circuits center frequency of the Y-6.5 cell is shown. Blue for a cooling process. Red for heating. The change of shape can be attributed by doping inhomogeneties which induce a little variation in the pressure response.

The difference between the ambient pressure response and the response at 4 GPa is obvious. By applying pressure the inset of the frequency change occurs at higher temperatures. The difference in shape can be attributed to doping inhomogeneties, which widens the pressure response. 10% of the frequency change was reached at ambient conditions at a temperature of 54 K. At a pressure of 4 GPa the critical temperature is 69 K. A summary the values are shown in Fig. 5.4.

5.1.2 COMPARISON TO THE LITERATURE

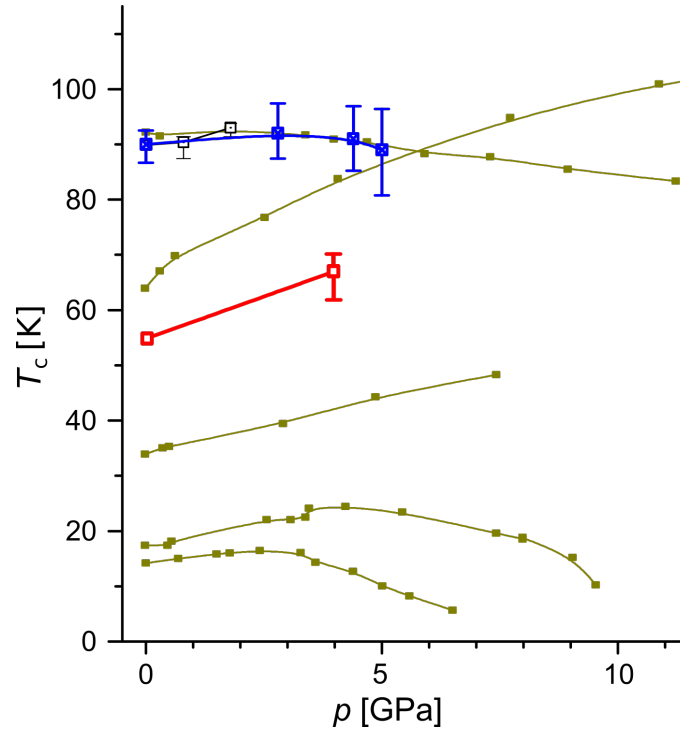


Figure 5.4: **Pressure dependence of the critical temperature:** In this figure the measured pressure dependencies of the critical temperature are shown. For the Y-6.5 cell in red, the Y-6.85 cell in blue. The black data points belong to the crystal Y-6.9, these measurements had been done by Steven Reichardt⁹. These data are plotted and compared with the literature data in yellow^{7,8}

In Fig. 5.4 the measured values for the two cells are presented and compared to the data from literature^{7,8}. In blue one can see the measured critical temperature of the Y-6.85 cell, in red the critical temperatures of the Y-6.5 cell, dependent on pressure. In black are the values measure by Steven Reichardt⁹. A compare of our data to the literature allowed a doping content determination. The structural formula of the sample in the Y-6.85 cell is $\text{YBa}_2\text{Cu}_3\text{O}_{6.85}$, for the sample in the Y-6.5 cell it is $\text{YBa}_2\text{Cu}_3\text{O}_{6.5}$.

5.2 ORIENTATION OF THE SINGLE CRYSTAL

The strong orientation dependence of NMR parameters make a precise alignment of the single crystal with respect to B_0 necessary. This was achieved by the grounding contact of the cylinder cells which also acts as a one axis goniometer. By the rotation of the cylindrical cell body in the holder (angle φ with $\varphi \in [0, 2\pi]$) and the tilting of the cell by the goniometer it self (angle β with $\beta \in [-\frac{\pi}{9}, \frac{\pi}{9}]$), an effective two axis positioning is possible.

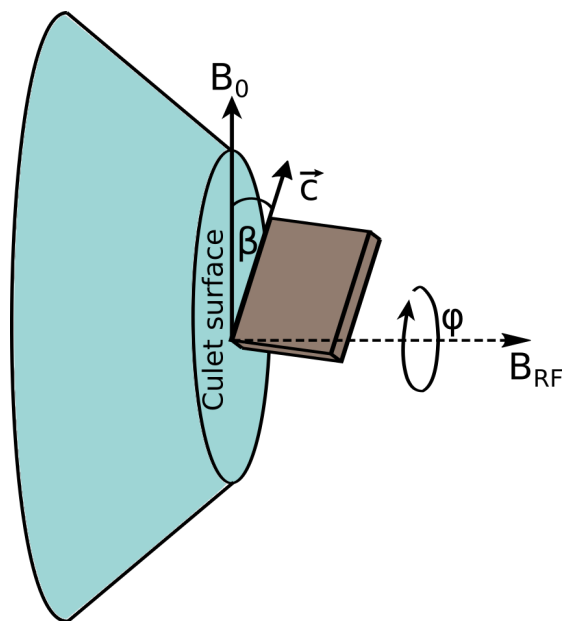


Figure 5.5: **Sketch of the crystal on the culet surface:** Here a single crystal fixed on the culet surface is shown. It is experimentally not possible to fix the crystal perfectly aligned to the culet surface. Which results in two angles needed for the alignment: the angle φ and the azimuth angle β

In general four NMR copper signals are possible to distinguish⁸⁶. First, the metallic copper which is in a small percentage in the silver wire of the microcoil. Second, the metallic copper signal from the copper beryllium gasket. These copper nuclei are outside the coil, so no nutation is possible. The third and the fourth are the copper signals from the single crystal inside the microcoil. The third is the signal from the CuO-chain site. Due to the interest of CuO₂-plane, this resonance was not studied systematically. The fourth is the copper signal from the CuO₂-plane.

For the alignment of a single crystal in the external magnetic field the orientation dependence of the second order quadrupole shift on the central transition of the ⁶³Cu nuclei of

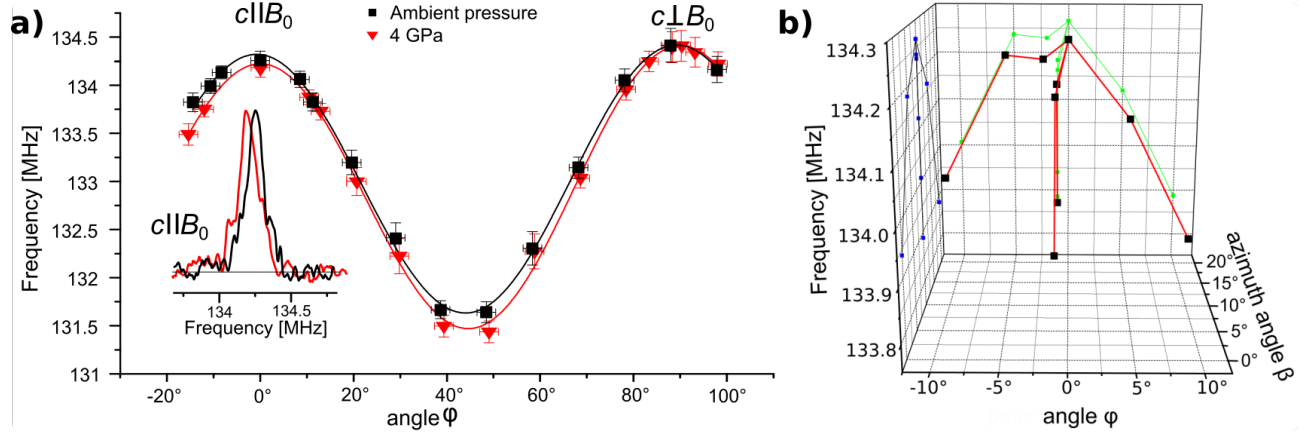


Figure 5.6: **Orientation dependency of the ^{63}Cu Central transition of the Y-6.5 cell:** **a)** The measured orientation dependent frequency values of the central transition are shown. Then the second order quadrupole effect on the central transition was used as fit function to determine the quadrupole frequencies⁹. Black at ambient conditions, red at 4 GPa. The quadrupole frequency increases from $\nu_{Q,\text{ambient}}=29.43 \text{ MHz} \pm 0.03 \text{ MHz}$ at ambient conditions to $\nu_{Q,4\text{GPa}}=30.01 \text{ MHz} \pm 0.05 \text{ MHz}$ at 4 GPa . (These data were recorded with the help of Stefan Zankov) **b)** Shows the orientation dependency of the central frequency in a 3D plot of the azimuth angle β and the angle ϕ . (This graphic was designed with the help of Michael Jurkutat)

the CuO_2 -plane was used. Due to its short T_1 of around $\approx 1.3 \text{ ms}$ at ambient conditions it was possible to do a lot of scans in an acceptable time. The resonance frequency of the central transition, in dependence on the orientation angle, goes through two maxima, at the orientation of $c\parallel B_0$ ($\phi = 0^\circ$) and $c\perp B_0$ ($\phi = 90^\circ$)⁸⁶. The measured frequency dependency for the Y-6.5 cell is shown in Fig. 5.6. The azimuth angle $\beta_{\text{Y-6.5}} = 10^\circ$ of this crystal with respect to the cell's body was determined by maximizing the frequency values of the central transition by changing the other axis of the goniometer while the crystal is in the orientation of the maximum of $c\parallel B_0$. The azimuth angle of the Y-6.85 cell was $\beta_{\text{Y-6.85}} = 5^\circ$. A very detailed description of this procedure as well as the derivation of the fitting function is given in a previous work by Steven Reichardt⁹. The consideration of Euler angles were used to correct the angles which were measured before the tilt of β was included. Then the angle dependence of the second order quadrupole shift of the central transition was used as fit function to determine the quadrupole frequency⁸⁶. This is shown in Fig. 5.6.

The difference between the fitted functions (function is given in sec. 2.1.8, eq. (1.7)) is due to the change in the quadrupole frequency, which increased from $\nu_{Q,\text{ambient}}=29.43 \text{ MHz} \pm 0.03 \text{ MHz}$ at ambient conditions to $\nu_{Q,4\text{GPa}}=30.01 \text{ MHz} \pm 0.05 \text{ MHz}$ at 4 GPa for the crystal

Y-6.5.

To check that the crystal did not change its orientation after the pressure was increased the same procedure was repeated at 4 GPa. The positions of the maxima of both fits are at the same angle in respect to the cells body (Fig. 5.2), in combination with the unchanged angle $\beta=10^\circ$, this is a proof that the orientation of the crystal did not change while pressure was increased.

5.2.1 QUADRUPOLE FREQUENCIES PRESSURE DEPENDENCY

In this section the measured values for the quadrupole frequencies are presented in Fig. 5.7:

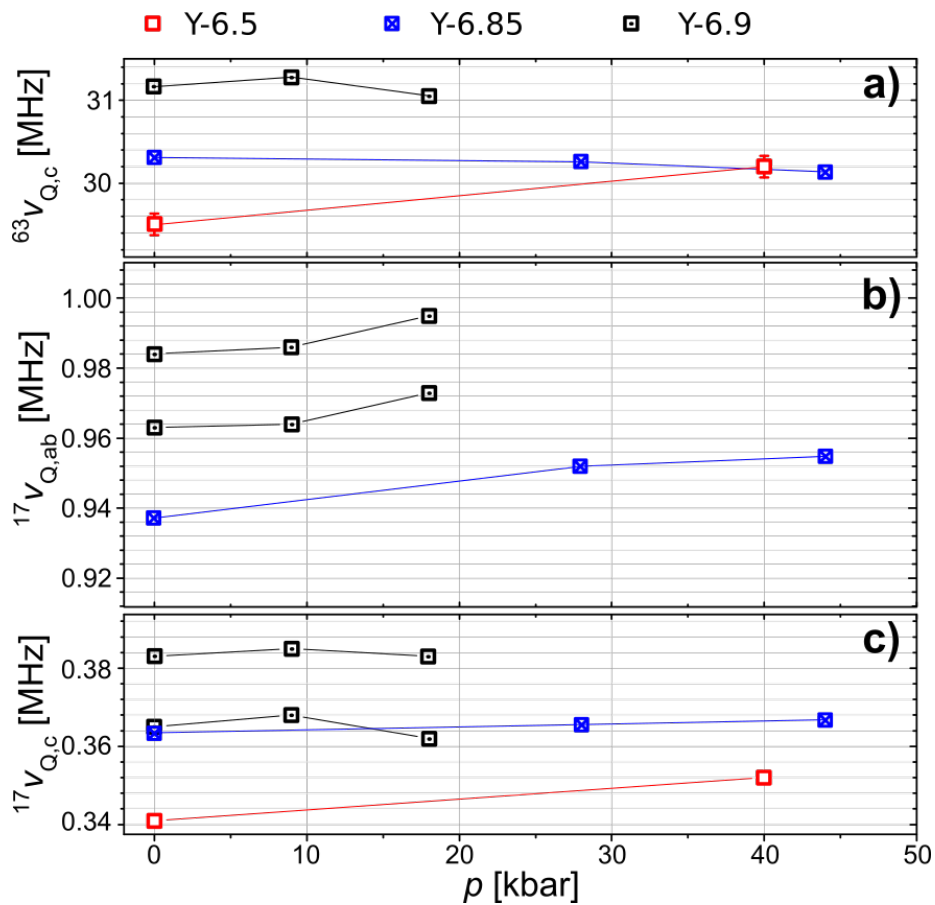


Figure 5.7: **Quadrupole frequencies, pressure dependency:** The Y-6.5 cell in red, the Y-6.85 cell in blue and the Y-6.9 cell, done and measured by Steven Reichardt⁹, in black. **a)** ^{63}Cu , $c\parallel B_0$ **b)** ^{17}O , $ab\parallel B_0$ **c)** ^{17}O , $c\parallel B_0$, this graphic and data were designed and evaluated with the help of Michael Jurkutat

In Fig. 5.7 **a)** the measured quadrupole frequencies $^{63}\nu_{Q,c}$ of the ^{63}Cu , the planar copper nuclei in the orientation $c\parallel B_0$, are presented. The quadrupole frequencies $^{17}\nu_{Q,ab}$ and $^{17}\nu_{Q,c}$ of the ^{17}O nuclei in the CuO_2 -plane, in the orientation $ab\parallel B_0$ and in the orientation $c\parallel B_0$ are shown in Fig. 5.7 **b)** and **c)**.

In Fig.5.7 **a)** one can see, $^{63}\nu_{Q,c}$ increases for the underdoped sample Y-6.5, while it stays almost constant for the near optimally doped Y-6.85 and the Y-6.9 crystal (Y-6.9 is part of a previous work by Steven Reichardt⁹⁾ and even decreases slightly at higher pressures. This is consistent with previous investigations¹¹⁸⁾. The quadrupole frequencies for the Y-6.5 cell were determined by the orientation dependency (see sec. 5.2). For the Y-6.85 cell and the Y-6.9 cell, the relative position of the satellite transitions were recorded.

In Fig.5.7 **b)**, $^{17}\nu_{Q,ab}$ shows the quadrupole frequencies of the ^{17}O nuclei when the crystal is oriented with the a - b -plane along the external B_0 -field ($ab\parallel B_0$). One can see an increase of $^{17}\nu_{Q,ab}$ for all samples. Unfortunately this splitting was not measurable with the Y-6.5 crystal filled cell, due to the bad SNR. The data for further evaluations of the Y-6.5 crystal comes from literature data^{7,119)}. For the Y-6.85 and the Y-6.9 cell full spectra were recorded at every predicted pressure value.

In Fig.5.7 **c)** $^{17}\nu_{Q,c}$, the quadrupole frequencies for the $c\parallel B_0$ orientation of the ^{17}O nuclei are shown. Here we also see for all samples an increase of the quadrupole frequencies which is more pronounced for the underdoped sample Y-6.5 than for the near optimally doped samples. Similar changes in underdoped crystals were also observed by Vinograd¹²⁰⁾. To determine the quadrupole frequencies in this orientation, the effort to record full oxygen spectra were done for the Y-6.5, Y-6.85 and Y-6.9 cell.

Some selected spectra of the Y-6.85 cell as well as for the Y-6.5 cell are shown in the appendix (see sec. A.1). From all the quadrupole frequencies the local charges as well as the hole content ζ can be determined^{84,97)} (theory sec. 2.1.7), which is shown in the next section.

5.2.2 CHARGES IN THE CuO_2 -PLANE UNDER PRESSURE

In the section above (sec. 5.2.1) the measured quadrupole frequencies are presented. The charges in the CuO_2 -plane can be determined by the quadrupole frequencies^{84,97} (sec. 2.1.7) and are presented in the following. The change with pressure (Δ_p) of the oxygen hole content ($2\Delta_p n_{\text{O}}$) and of the copper hole content ($\Delta_p n_{\text{Cu}}$) were calculated. This allows the determination of the change of the general doped hole content ($\Delta_p \zeta$) in the plane, measured by NMR.

The values are plotted in Fig. 5.8 over different parameters. **a)** to **c)** over the applied pressure. In **d)** and **e)** the value of $2\Delta_p n_{\text{O}}$ and $\Delta_p n_{\text{Cu}}$ are plotted over the change in doping $\Delta_p \zeta$. In Fig. 5.8 **f)** n_{Cu} is depicted over $2n_{\text{O}}$ which gives the planar charge distribution (see sec. 2.1.7). The diagonals in **f)** represent lines of constant doping content ζ :

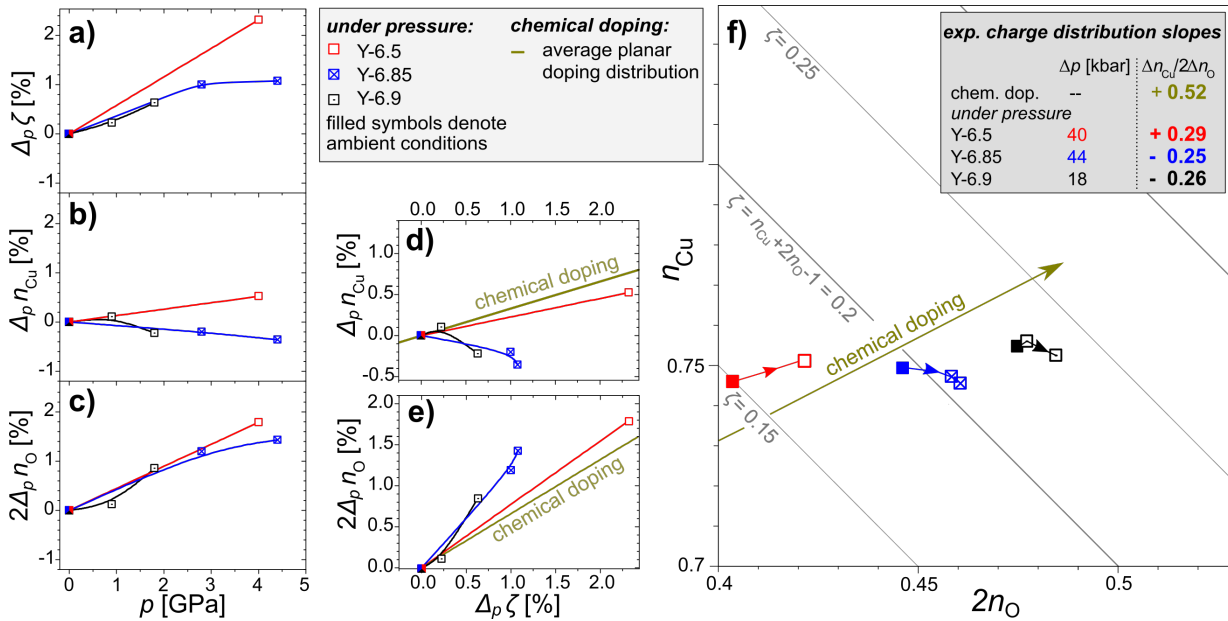


Figure 5.8: **Planar Charges:** Filled symbols denote the value at ambient conditions. Empty symbols the values at elevated pressure. **a)** shows the change of $\Delta_p \zeta$ dependent on the pressure **b)** shows the change of $\Delta_p n_{\text{Cu}}$ dependent on the pressure **c)** shows the change of $2\Delta_p n_{\text{O}}$ dependent on the pressure **d)** shows the change of $\Delta_p n_{\text{Cu}}$ dependent on $\Delta_p \zeta$ **e)** shows the change of $2\Delta_p n_{\text{O}}$ dependent on $\Delta_p \zeta$ **f)** Shows the $2n_{\text{O}}-n_{\text{Cu}}$ -plane and the pressure induced movements of the different samples. This graphic was designed with the help of Michael Jurkutat¹¹⁴

Starting with Fig. 5.8 **a**): If pressure is increased, an increase in hole doping is clear for all samples ($\Delta_p \zeta > 0$). The change in doping is larger for the Y-6.5 sample in red, with a slope of $\approx 5.8 \times 10^{-3}$ holes/GPa. The slopes for the near optimally doped samples in blue for the Y-6.85 and in black for the Y-6.9 were $\approx 3.5 \times 10^{-3}$ holes/GPa in the low pressure area, but it flattened at higher pressures.

In Fig. 5.8 **b**) one can see the change of $\Delta_p n_{\text{Cu}}$ depending on the pressure. For the Y-6.5 (red) sample the slope is $\approx 1.3 \times 10^{-3}$ holes/GPa. The nearly optimally doped sample Y-6.9 (black) shows for low pressures a weak increase, but for higher pressures beyond 1 GPa a decrease of the Cu hole content can be seen. The Y-6.85 (blue) sample shows a clear decrease of $\Delta_p n_{\text{Cu}}$ for elevated pressures.

In Fig. 5.8 **c**) the change of $2\Delta_p n_{\text{O}}$ with pressure is shown. For all cells one can see a clear increase of $2\Delta_p n_{\text{O}}$ with pressure. The slope of this increase is $\approx 4 \times 10^{-3}$ holes/GPa. The near optimally doped sample (blue) shows a flattening effect for higher pressures.

To compare the increase or decrease of the hole contents at the oxygen ($2\Delta_p n_{\text{O}}$) and copper ($\Delta_p n_{\text{Cu}}$) nuclei in the plane, the relation to the total change of the hole content ($\Delta_p \zeta$) with pressure, is presented in Fig. 5.8 **d**) for copper and **e**) for oxygen. The chemical doping slope ($+0.52 \Delta n_{\text{Cu}}/2\Delta n_{\text{O}}$) is marked with the yellow line.

In **d**) one can see the change of $\Delta_p n_{\text{Cu}}$ over $\Delta_p \zeta$. Here the changes is below the chemical doping slope for all three samples. In **e**) the change of all samples of $2\Delta_p n_{\text{O}}$ is clearly above the chemical doping slope. In combination these plots clearly indicate a pressure induced intra planar charge redistribution. Where the oxygen hole doping is favored over the copper hole doping. Which is more pronounced in the near optimally doped samples Y-6.85 (blue) and Y-6.9 (black). For the Y-6.5 cell the slope is much nearer at the chemical. Here we clearly observe a decrease of n_{Cu} and an increase of n_{O} , compared to the expected changes only from doping.

In Fig.5.8 **f**) the values are plotted in the $2n_{\text{O}}-n_{\text{Cu}}$ -plane. The ambient values are marked by a filled symbol while the direction of the movement in the plane if pressure is increases is marked by a arrow.

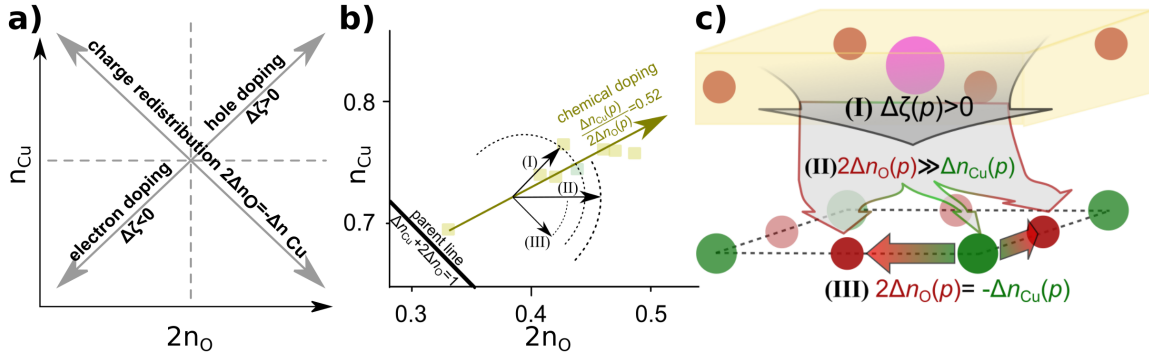


Figure 5.9: **Movements in the $2n_{\text{O}}-n_{\text{Cu}}$ -plane:** **a)** a compass is shown, which explains the effects which are behind the movements in the different directions in the $2n_{\text{O}}-n_{\text{Cu}}$ -plane **b)** shows the three effect I - III which can occur in the $2n_{\text{O}}-n_{\text{Cu}}$ -plane at the example of YBCO **c)** shows a cut out from the crystal structure and depicts the three effect I - III; (These graphic were designed with the help of Michael Jurkutat)

Next, we consider movements in the $2n_{\text{O}}-n_{\text{Cu}}$ -plane. In Fig. 5.9 **a)** a compass is shown which indicates the direction of the movement in the $2n_{\text{O}}-n_{\text{Cu}}$ -plane by two orthogonal arrows. The one direction indicates the change of the doping content. Perpendicular is the direction of a movement along a $\zeta = \text{const.}$ line. Such a movement would indicate a charge redistribution, which means the single values of $2n_{\text{O}}$ and n_{Cu} change, but the sum is still constant.

In Fig. 5.9 **b)** and **c)**, three different effects areas are marked with roman numbers to show the three effects which been observed.

I, denotes the effect of doping holes in the CuO_2 -plane, if pressure is applied, which is clearly observed (see Fig. 5.8 **a)**).

II, describes the effect when charges enter the CuO_2 -plane, they favor the location at oxygen atom over the location at the Cu atom. So the increase of $2n_{\text{O}}$ is favored over n_{Cu} , and more so than by chemical doping. This is observed for all samples by the deviation of the chemical doping slope in Fig.5.8 **f)**.

III, is an intra planar charge redistribution. This is observed for the higher pressures in the nearly optimally doped samples.

In Fig. 5.9 **c)** all three effects I - III are shown in a sketch of the crystal structure.

THE $2n_{\text{O}}-n_{\text{Cu}}$ -PLANE :

To have a closer look on the $2n_{\text{O}}-n_{\text{Cu}}$ -plane, a zoomed in graphic of Fig. 5.8 f) is given Fig. 5.10. The filled symbols denote the ambient conditions, while the colored arrows show the direction of the changes in the plane.

For the Y-6.5 (red) sample, one can see clearly an increase in doping. Furthermore the slope ($+0.29 \Delta n_{\text{Cu}}/2\Delta n_{\text{O}}$) is below the slope of the chemical doping ($+0.52 \Delta n_{\text{Cu}}/2\Delta n_{\text{O}}$) which indicates the favoring effect II of pressure on the plane. For the Y-6.85 (blue) sample, one can see the I effect by the move direction away from the parent line ($\Delta_p \zeta > 0$). The II effect one can see by the deviation from the chemical slope. The slope here is even negative $-0.25 \Delta n_{\text{Cu}}/2\Delta n_{\text{O}}$ which indicates the third effect III, the intra planar charge redistribution. This is more pronounced especially for higher pressures. For the Y-6.9 (black) sample almost the same behavior is shown. I shows an increase in ζ . II the slope $-0.26 \Delta n_{\text{Cu}}/2\Delta n_{\text{O}}$ is clearly below the slope of chemical doping. And even the III effect, the charge redistribution is observable for higher pressures.

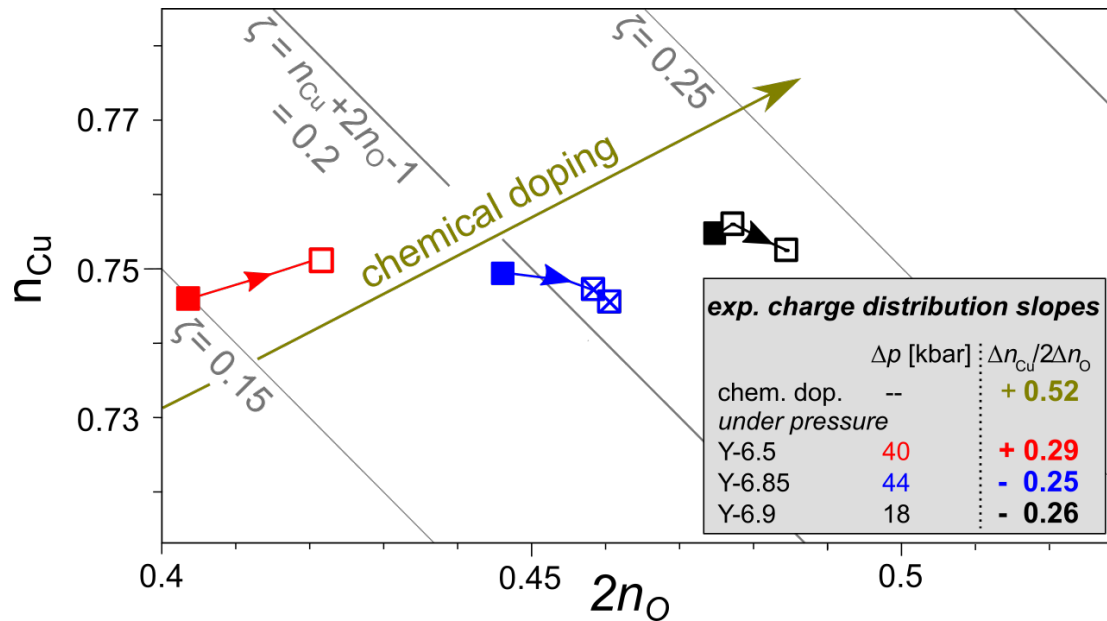


Figure 5.10: $2n_{\text{O}}-n_{\text{Cu}}$ -plane: Here the measured values of the charge distribution of holes between oxygen and copper are plotted in the $2n_{\text{O}}-n_{\text{Cu}}$ -plane . One can clearly see a deviation from the chemical doped direction, which is marked by the yellow arrow. In all three samples the oxygen hole content increases stronger then the copper hole content; for more information please check the text above (This graphic was designed with the help of Michael Jurkutat)

5.3 DISCUSSION

I, The first effect, the pressure induced doping, depends clearly on the initial hole doping content. Some previous works found values of a doping change, up to $\partial x/\partial p \approx 2\%/GPa$ ^{121,122}. Our data give a weaker slope of $\partial\zeta/\partial p \approx 0.58(5)\%/GPa$ for the Y-6.5 crystal and $\partial\zeta/\partial p \approx 0.36(5)\%/GPa$ for the near optimally doped samples. Patricia Alireza¹²³ estimated in 2017 for stronger underdoped YBCO samples a slope of $\partial x/\partial p \approx 0.32\%/GPa$. Different theoretical modeling approaches argue against these values^{120,124}.

II, The second effect, describes the favoring of the entering hole to a location at the oxygen atom over a location at the copper atom. Pressure increases $2n_O$ more the n_{Cu} a chemical doping would, which leads to a relative higher O hole content. Liangzi Deng¹²⁵ found similar effects in Bi-based cuprates by first principle calculations. Their finding of $\partial n_{Cu}/\partial p \approx -0.4\%/GPa$ is a bit larger than ours.

III, the intra-planar charge redistribution induced by pressure is obvious by observing the decreases n_{Cu} while the overall doping ζ increases. This redistribution from holes at the copper atoms to oxygen atoms shows an increase in the copper oxygen bond covalency, which can be seen as a decrease of the charge transfer gap. Oxygen increases its contribution to the unoccupied bands while copper to the occupied. Other methods in several studies found a decreasing charge transfer gap consistent with an increasing $T_{c,max}$ ^{126,127,128}.

The increase of $T_{c,max}$ by applying pressure for different doping levels were in good agreement with previous reports⁸. The slope of the critical temperature on the pressure, given by our data is $0.84(1)K/GPa$ which is in good agreement with early values given by Sascha Sadewasser et. al.¹²⁹. They found for the intrinsic pressure effect of YBCO a slope of $1K/GPa$. Comparing different cuprate families, here YBCO to $La_{2-x}Sr_xCuO_4$ (LSCO), shows the mixture of effects differ. While in YBCO the chemical doping and charge redistribution, both is affected by pressure, in LSCO the doping almost unaffected and T_c increases for all doping levels¹³⁰. This increase points to a mainly charge redistribution induced by pressure in LSCO which is for all doping levels consistent shown by a pressure-independent Hall coefficient⁹⁶.

In 2021 André-Marie Tremblay at the Université de Sherbrooke⁹⁹ confirmed with a three-band Hubbard model with cellular dynamical mean-field theory the observations done by Michal Jurkutat^{97,98} which found a order of cuprates according to their maximal T_c depending on the oxygen hole $2n_O$ content of the CuO_2 -plane. The redistribution effect of charges in the CuO_2 -plane affected by pressure could be part of models in the future which consider the shrinking of the unit cell.

*“There is no adequate defense, except stupidity,
against the impact of a new idea.”*

Percy Williams Bridgman

6

Silver-Indium-Telluride NMR under pressure

In this chapter the pressure investigation of silver-indium-telluride powder (AgInTe_2) is presented. The phase transition^{78,107} between 3 GPa and 4 GPa was of interest. Unfortunately no signal was found at pressures above 5 GPa. Up to pressures of 2.5 GPa an increase of the quadrupole frequency was observed and proven by a nutation spectroscopy experiment. The spectra at 4 GPa and 5 GPa point to a quadrupolar second order affected central transition of a powder. The phase transition could not be proven by these NMR experiments due to the signal lost at higher pressures.

The data presented in this section are published by the American Chemical Society¹³¹

6.1 INTRODUCTION

Silver-Indium-Telluride (AgInTe_2) is a chalcogenide with a tetrahedral coordination at ambient conditions. Chalcogenides are chemical compounds which contain chalcogen anions (oxygen, sulfur, selenium, tellurium, ...) and other, metallic or strong electropositive elements as cations. The indium atom has 4 nearest neighbors of tellurium in a tetrahedral coordination.

With a non-zero Seebeck coefficient¹³², AgInTe_2 is part of the thermoelectric materials. These materials show a potential difference by a temperature difference of their surfaces and reverse, electronically measurable by a voltage. While in most material these effects are very small, too small to be useful in technical application, AgInTe_2 is of interest of the photovoltaics and optoelectronics research. But AgInTe_2 it self is not a "good" thermoelectric. The chemical flexibility of the chalcogenides allows the synthesis of a large number of various solid solutions, with a wide range of energy band gaps and lattice parameters^{102,105,106}.

For high pressure physics AgInTe_2 is interesting due to its phase transition between 3 – 4 GPa^{78,107}. The structural phase transition of AgInTe_2 was reported with X-ray diffraction (XRD) studies in 1969. From the chalcopyrite structure, almost perfectly order with silver (Ag), indium (In) and tellurium (Te) atoms, to the high pressure phase, an unordered NaCl-type structure or an unordered $Cmcm$ structure, which are discussed in literature^{78,107}. These observations are confirmed by *ab-initio* techniques¹⁰⁸. The chalcopyrite crystal structure ($I\bar{4}2d$) of AgInTe_2 at ambient conditions, gives a surrounding of each silver and indium atom by 4 tellurium atoms. The pressure-coordination rule²² expects a phase transformation to a structure with a higher coordination number. The NaCl-type structure as well as the $Cmcm$ structure fulfills these conditions.

After decompression the high pressure phase slowly transforms back to the chalcopyrite structure, with a disorderd sphalerite-type structure in between⁷⁸. At elevated temperatures this process can take over weeks. Recording this restructuring process with NMR, to answer the question of the energy dissipation, was part of the motivation for the high pressure investigation of the material. Unfortunately this question could not be answered with this work.

For more detailed information about the crystal structures and phase transition, please check the samples chapter, in sec. 2.2.

6.2 SAMPLE

The measured sample of AgInTe_2 was prepared by Simon Welzmler under the guidance of Oliver Oeckler at the University of Leipzig (for more details please check^{105,106} or the basic chapter, sec. 2.2).

The Silver (Ag 99.999%, Premion), Indium (In 99.999%, VEB Spuremetalle Freiberg), and Tellurium (Te, puriss., VEB Spuremetalle Freiberg) were melted in stoichiometric amounts in a sealed silica ampule under a dry argon atmosphere. From 950 °C, the mixture was quickly cooled, followed by an annealing procedure at 400 °C.

A X-ray diffraction experiment, using a Huber G670 Guinier diffractometer, suggests a high level of purity and homogeneity. A Rietveld simulation based on a chalcopyrite-type structure was fitted to the recorded XRD data. For the NMR experiments a fine powder was grinded using an agate mortar and pestle. All the NMR experiments are made at fields of at 9.3 T and 11.7 T at ambient temperatures.

6.3 PRESSURES CELLS

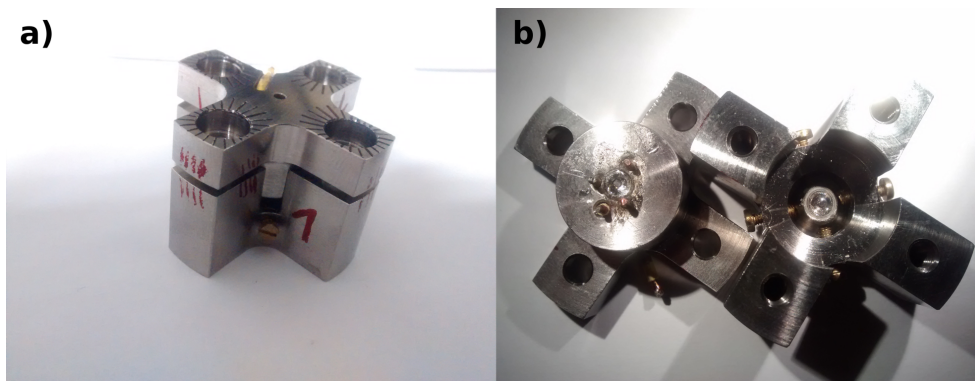


Figure 6.1: **Picture of a cross cell:** a) the closed cross cell with markers to hold the initially defined orientation, b) a opened cross cell, one can see the anvils in the center as well as the screws for the alignment of the seats containing the anvils and the guide pins for the gasket.

The pressure cells used in the experiments are cross cells (see Fig 6.1). Built and designed at the University of Leipzig by T.Meier⁴⁴. Only powdered samples can be measured in these cells. Due to the unsymmetrical design no fitting goniometer for angle dependent measurements was built. (for more details check the sec. 1.3.3)

6.3.1 SIGNAL TO NOISE RATIO

The signal to noise ratio (SNR) is a limiting factor of the experiments presented here. To record one spectrum the needed time of signal averaging was ≈ 2 Days at ambient condition and was even increased for elevated pressures. The experimental repetition time of 5 times T_1 resulted in $t_{repetition,ambient}=150$ ms. 10^6 scans for the echos at ambient conditions were needed. At elevated pressures, the SNR decreases, and more scans are needed to resolve a spectrum. One measurement could then take several days up to a week.

For the nutation experiments the FID signal was used, which needed a much lower number of scans to resolve only the central transition. To avoid possible heating effects for high power levels at the nutation experiments, the repetition times were increased. For example, with a pulse power of 100 W the repetition time was $t_{repetition,100W} = 700 \mu s$, which led to a experimental time of one nutation experiment of 9 Days. Per pressure point and cell it took around two weeks. The time for the measurement at all pressure points and in all cells were in sum several months up to a year.

The SNR for the different pressure values are given below:

Cell 1:

- Ambient $\rightarrow 0.05$
- 1.4 GPa $\rightarrow 0.01$
- 2.5 GPa $\rightarrow 0.006$
- 3 GPa $\rightarrow 0.002$

Cell 2:

- Ambient $\rightarrow 0.09$
- 4 GPa $\rightarrow 0.01$
- 5 GPa $\rightarrow 0.002$
- After pressure release $\rightarrow 0.006$

6.4 MEASUREMENTS

6.4.1 FID OF SILVER-INDIUM-TELLURIDE AT 11.7 T

Both natural occurring Indium isotopes are NMR active. ^{115}In with a natural abundance of 95.72% and ^{113}In with a natural abundance of 4.28%. The FID of the ^{115}In in AgInTe_2 occurs at a frequency of 109.537 MHz. This line is shifted by -481ppm with respect to the reference material $(\text{In}(\text{NO}_3)_3)$. Due to the low conductivity (1 meV bandgap) the shift is considered to be purely chemical. The resonance line of the second isotope ^{113}In occurs at the frequency of 109.305 MHz. The spin quantum number for both isotopes is $(I=9/2)$. Small deviations from the cubic symmetry of the Indium environment occur^{102,105}. The powder spectra consist of a sharp central peak surrounded by a broad foot (see Fig. 6.2):

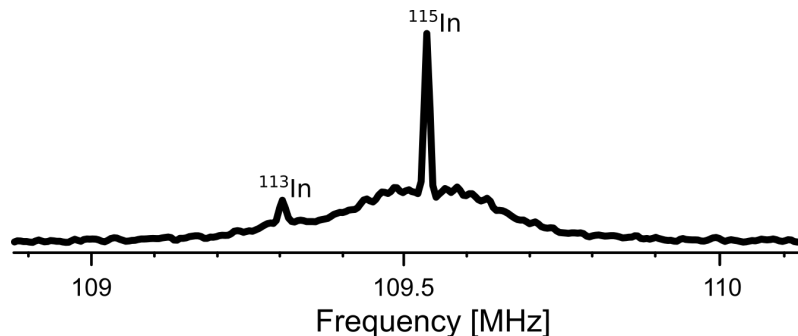


Figure 6.2: **Spectrum of AgInTe_2 , at ambient conditions:** Here the spectrum of AgInTe_2 is shown at ambient conditions. One can see the broad foot around the sharp central peak of ^{115}In . This can be caused by the small deviations from the cubic symmetry of the Indium's environment and quadrupolar interactions. The second peak shows the ^{113}In resonance.

A simulation done by Robin Gühne, matching to the same sample, published in here¹³³, assumed the following parameters to describe the powder spectrum. The quadrupole frequency $\nu_Q = 90\text{ kHz}$, the asymmetry parameter $\eta_Q = 0.3$ and a Gaussian additional broadening $2\sigma = 7\text{ kHz}$. This broadening effect is assigned to be a quadrupolar broadening due to local variations of the Indium's surrounding.

6.4.2 SPECTRUM

Here the spectra at different pressures are put together in one figure, (see Fig. 6.3). To record the spectra at ambient conditions, at 1.4 GPa, at 2.5 GPa and at 3 GPa, solid echos experiments ($\frac{\pi}{2}-\tau-\frac{\pi}{2}$) were performed in Cell 1. For the spectra at 4 GPa and 5 GPa, Hahn echo experiments ($\frac{\pi}{2}-\tau-\pi$) were performed in Cell 2. The spectra after the release of pressure was recorded in Cell 2 after reaching a pressure of 10 GPa, due to the large deformation of the coil the signal had a bad SNR:

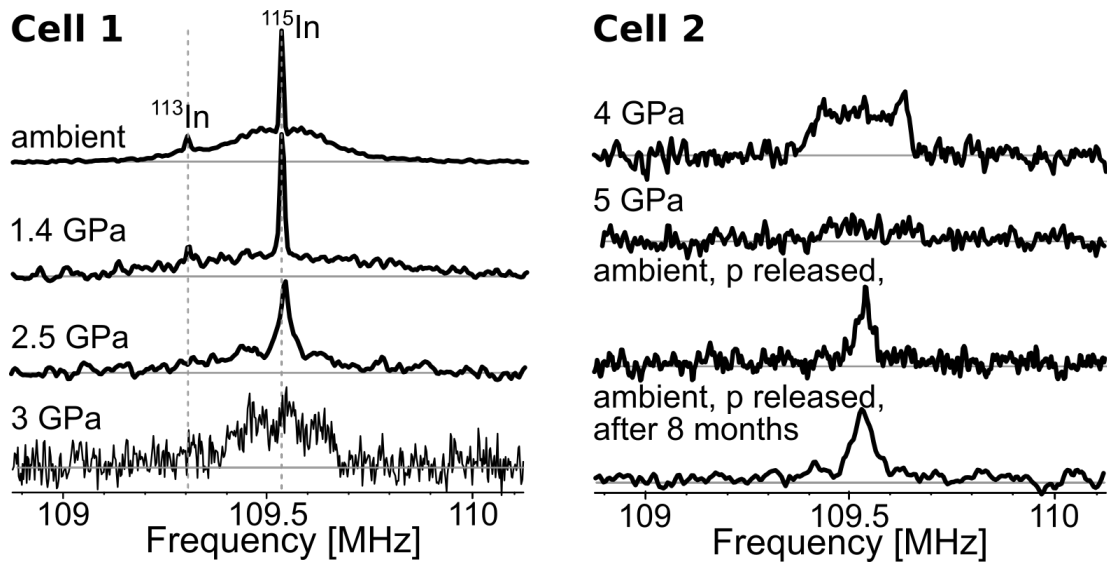


Figure 6.3: **Spectra of AgInTe_2 , pressure dependent:** The spectra of AgInTe_2 are presented at different pressures. **Cell 1:** in the left column the spectra from ambient to 3 GPa is given. From Ambient to 1.4 GPa the foot gets broader which could indicate an increases of the quadrupole frequency. At 2.5 GPa also the central transition is affected and strongly broadened. At 3 GPa a broad very noisy spectral distribution is recorded, which hints to a second order quadrupole affected central transition. The worsening of the SNR of Cell 1 led to the construction of a second cell with better SNR to carry out the measurements at higher pressures. **Cell 2:** in the right column one can see the spectra recorded at higher pressures in cell 2. At 4 GPa one can see a signal distribution which could depict a second order broadened central transition. At 5 GPa the signal is vanished almost completely. It was not possible to record a signal at higher pressures up to 10 GPa. But after the release of pressure back to ambient conditions, a ^{115}In signal was recorded again at the originally ambient position, due to the bad SNR after the expected deformation of the coil, the broad foot could not be recorded. After 8 months the measurement was repeated with more scans, but no significant change was seen.

The ambient spectrum of Cell 1, in the left column in Fig. 6.3, shows clearly the resonances of both isotopes ^{115}In and ^{113}In , and also a broad foot of the weakly perturbed satellite transitions of a powder around the central transitions, like shown in section 6.4.1 in Fig. 6.2. The second spectrum which was recorded at 1.4 GPa also shows a narrow central transition of both isotopes, but the foot of satellite transitions is much broader distributed, this hints at an increase of the electric field gradient in the unit cell which results an increase of the quadrupole frequency and with this a broader frequency distribution. The third spectrum at 2.5 GPa shows a slightly higher shift and a conspicuous broadening of the central transition. The fourth spectrum at 3 GPa was recorded with a large signal loss. A broad signal distribution is recorded with no obvious sign of a central transition. The second isotope ^{113}In can not be resolved for the elevated pressures.

Due to the bad SNR a new cell was built to reach higher pressures. The fifth spectrum at 4 GPa on the right side of Fig. 6.3 shows a broad distribution of resonances which could be a second order quadrupole affected central transition of a powder. More details about this effect is investigated in section 6.4.4. The sixth spectrum at 5 GPa was the highest pressure an echo was found, unfortunately the SNR was extremely bad. At pressures of 6.4 GPa, 8.2 GPa and 10 GPa no signal was found in a broad frequency range. The seventh spectra show the frequency distribution after the pressure was released. A signal was found at the position of the ambient resonance. The bad SNR could be explained by the large deformation of the coil and the chamber by reaching the 10 GPa before. A second measurement 8 months later, with much more scans to improve the SNR, confirmed the spectrum, no broad foot was resolved.

6.4.3 NUTATION SPECTROSCOPY

Here a nutation spectroscopy carried out in a NMR-Anvil Cell is presented. It was performed to investigate the quadrupole interaction of the indium nuclei of the powdered AgInTe_2 sample for ambient, 1.4 GPa and 2.5 GPa. With increasing the pressure the frequency range of the broad foot around the central transition increases as well. Nutation spectroscopy confirms an increasing field gradient.

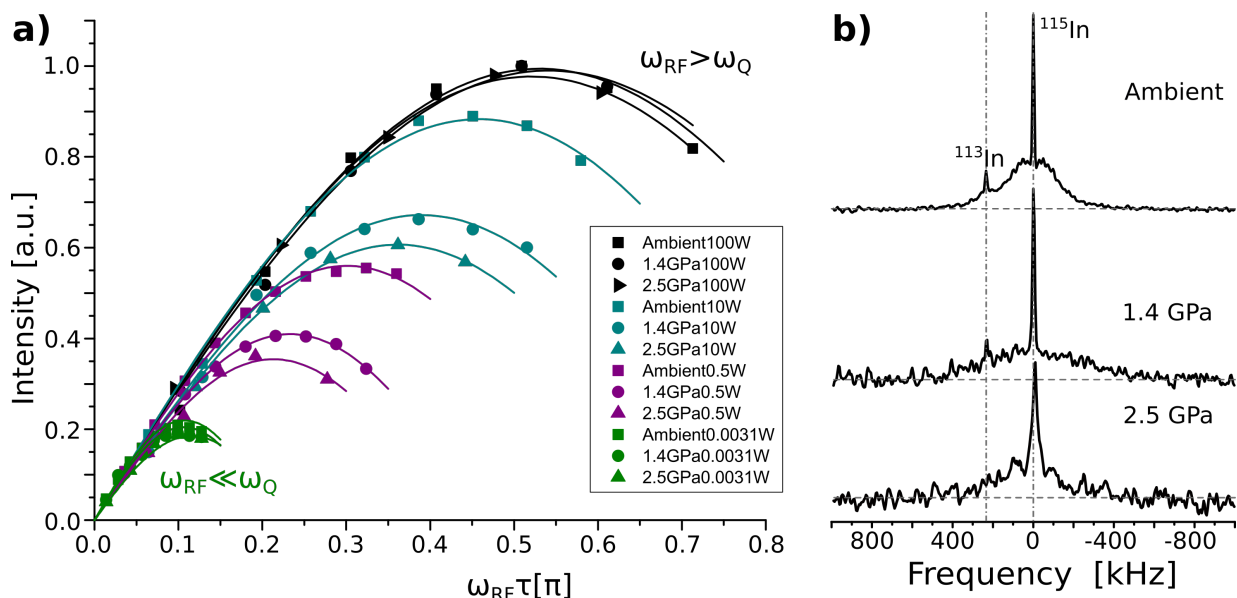


Figure 6.4: ^{115}In nutation spectroscopy at different pressure a) The power values between 100 W for non-selective excitation and 0.0031 W for the selective excitation are equal for all pressures as well as the $\pi/2$ -pulse length of 0.5μ . The intermediate power levels show the tendency of an earlier bending for higher pressures, which proves an increase of the quadrupole frequency with elevated pressure. b) The associated spectra at the considered pressures, one can see the increase of the range of the foot around the central transition with increasing pressure.

A final proof of an acting quadrupole coupling of a nuclei can be given by power level dependent nutation experiment (see section 1.1.8 for theory). The response of a given spin system to a perturbation, in this case a Radio-Frequency-pulse (RF-pulse), depends strongly on the relation between the RF-pulse strength and the intensity of the quadrupole coupling which is given by $\omega_Q = 2\pi\nu_Q$.

If the RF-pulse strength ω_{RF} is varied, ω_Q can be estimated. The excitation is called non-selective if the RF-pulse is much stronger than the quadrupole interaction ($\omega_{RF} \gg \omega_Q$). In this case the contribution of the quadrupole interaction to the sum of Hamiltonians can be ignored during the excitation, the RF-pulse is the dominant part. In the non-selective case the system therefore acts like a spin 1/2 system.

The excitation is called selective if ($\omega_{RF} \ll \omega_Q$), which can be described like the excitation of a single transition^{10,14}. The central transition of a powdered sample is the only transition which can be treated almost independently. So the selective excitation is aimed on this transition.

The quantum number $I = 9/2$ defines the ratio between the selective and the non-selective case (see section 1.1.8).

$$I_{selective} = \frac{I_{non}}{I + 1/2} = \frac{I_{non}}{5} \quad (6.1)$$

Moreover the RF-frequency of the non selective case is increased by this factor.

$$\omega_{RF,selective} = (I + 1/2)\omega_{RF,non} = 5 \cdot \omega_{RF,non} \quad (6.2)$$

The equation (eq. 6.1) and frequency (eq. 6.2) are fulfilled in Fig. 6.4.

The behavior of the spin system if excited with the intermediate power values ($\omega_{RF} \approx \omega_Q$) allow the determination of ω_Q . Here it should be noted, the agreement of a simulation and an experiment remains strongly limited. Due to the considerable uncertainties, the determined values can vary. However, in Fig 6.4 one can see an increase of the quadrupole frequency by the tendency of an earlier bending of the curves at the same power values at elevated pressures.

To gauge the RF-coil excitation with a 1/2-Spin system metallic aluminum was added in the sample chamber. Aluminum nuclei has a spin number of $I = 5/2$, but in it's perfectly cubic environment the electric field gradient is zero. Without a splitting all resonances, the central transition and the satellites transitions are at the same frequency and act like a spin 1/2 system. The nutation of ^{115}In , with the highest power value of 100 W, acts exactly like the aluminum excitation, like a spin 1/2 system.

For a fixed set of power values, driven down from high ($\omega_{RF} \gg \omega_Q$) to low ($\omega_{RF} \ll \omega_Q$), a higher quadrupole interaction will lead to an earlier reaching of the selective behavior. The measured nutation maxima ($\pi/2$ -pulses) occur earlier for higher pressures and similar

power levels, implying an increasing quadrupole interaction by pressure. It proves the observation of the spectra that the quadrupole frequency increases.

6.4.4 SECOND ORDER EFFECT AND SIGNAL LOSS ABOVE 5GPa

After the pressure was increase up to 4 GPa, in the pressure region of the expected phase transition, the shape of the spectrum changed much. The intensity of the echo decreased and the original sharp central transition of indium disappeared. To investigate this in more detail Hahn echo experiments were employed.

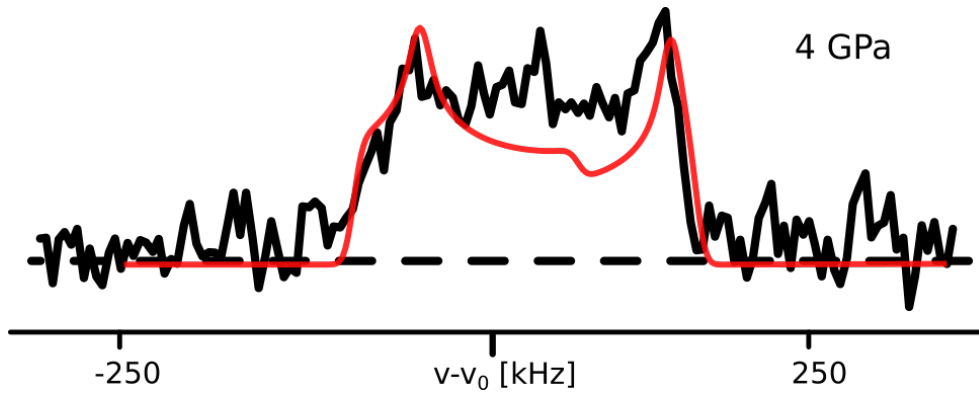


Figure 6.5: ^{115}In spectrum at 4 GPa with simulation: Hahn echo Experiment, with a pulse length of $0.5 \mu\text{s}$ at 4 GPa. The measured spectrum is depicted by the black line. The simulation of a second order quadrupole affected central transition of a powder is fitted with a red line (This simulation was done by Robin Guehne)

(Fig. 6.5) shows the ^{115}In spectrum of AgInTe_2 at 4 GPa. The sharp edges of this measured spectrum (black line), combined with invisible satellite transitions, remind on a second order quadrupole affected central transition of a powder. The graphic additionally shows a simulation (red line) of a second order affected central transition of a powder done by Robin Guehne. The parameters for this simulation are:

$$\nu_Q = 2420 \text{ kHz} \quad \eta = 0.18 \quad \sigma = 34 \text{ kHz}$$

The quadrupole frequency increased from $\nu_{Q,Ambient}=90 \text{ kHz}$ to $\nu_{Q,4\text{GPa}}=2420 \text{ kHz}$ by the factor of $f=\frac{2420}{90} \approx 37$. This could point to a phase transition or a intermediate mixed state between the two known phases^{78,102}

Unfortunately it was not possible to investigate this spectrum at an other B_0 field to prove it is an second order affected central transition of the powdered sample.

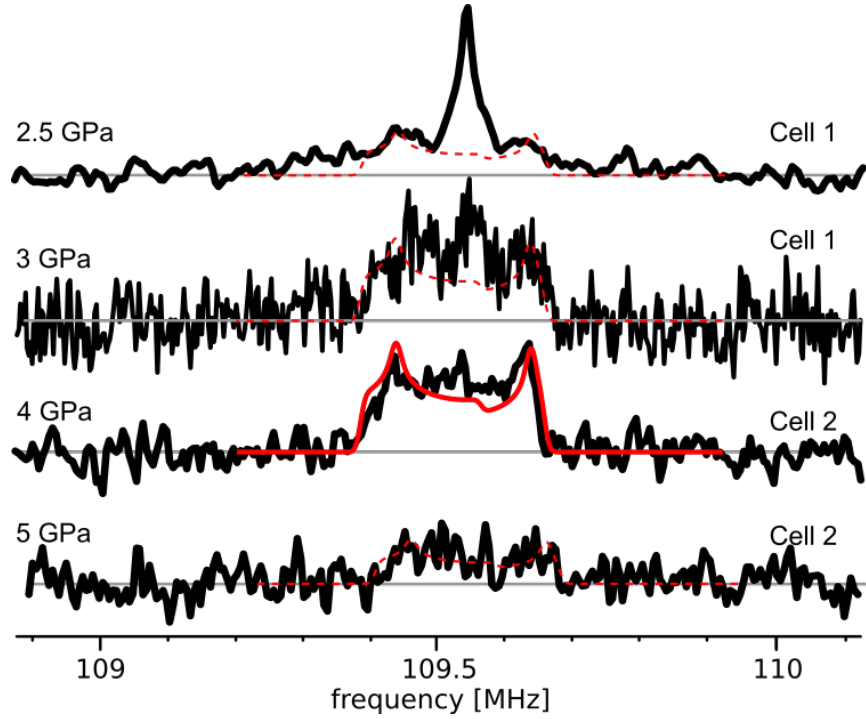


Figure 6.6: **Second order affected spectra AgInTe_2** : The black lines show the measured spectra. The red solid line at 4 GPa shows the simulation depicted in Fig. 6.5. This simulation is drawn with a red dashed line also in the other spectra to show a conjecturer of an under laying second order quadrupolar affected central transition which increases with pressure and vanishes above 5 GPa. The spectrum at 2.5 GPa and 3 GPa was recorded in cell 1, The spectrum at 4 GPa and 5 GPa was recorded in cell 2.

In the Fig. 6.6 the spectra of AgInTe_2 at different pressure values are shown. Around the pressure range between 3 GPa and 4 GPa, were the phase transitions was identified by XRD⁷⁸, the spectral distribution of resonances changes strongly. The Spectrum at 2.5 GPa shows the first inset of a possible second order quadrupole effect. The central transition (CT) is broadened while the horns left and right of the CT rise. For 3 GPa one can see the broad distribution of resonances which fit the width of the 4 GPa and 5 GPa spectrum. Furthermore the central peak decreased. This could point to a coexistence of two phase in this pressure range. The red solid line in Fig. 6.6 show a simulation of a second ordered affected central transition of a powdered sample which fit to the spectrum at 4 GPa. The red dashed lines are the same simulation drawn in the spectra at the other pressures to give an idea of the possible mixture.

The measurement at 5 GPa show a massive signal loss in compare to 4 GPa. At 6.4 GPa up

to 10 GPa no signal was found. Different echo experiments were performed to find signals at these high pressures. 5 – 10 MHz broadband solid echos as well as narrow frequency stepped Hahn echos at different frequencies in a band width of 3 MHz with a large number of scans were performed but no resonance were found.

6.4.5 T_1 MEASUREMENTS

To measure the longitudinal relaxation in an external B_0 -field, recovery experiments of Indium in AgInTe_2 at different pressures were performed.

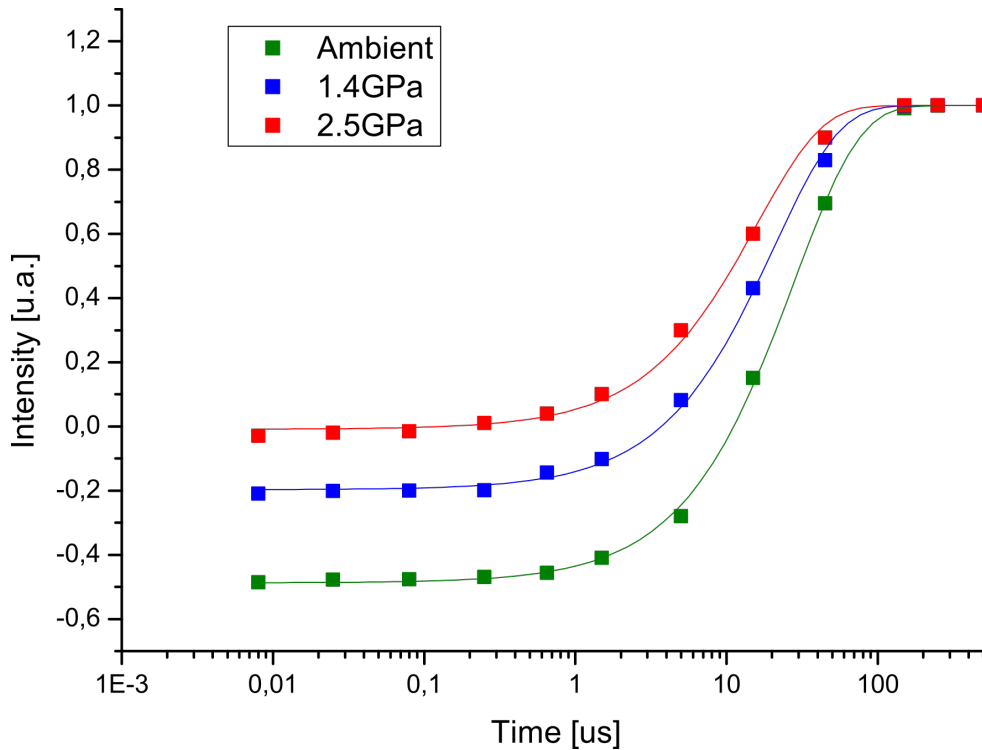


Figure 6.7: T_1 measurements of Indium in AgInTe_2 for different pressures: At ambient conditions is $T_1 = 28.1$ ms, at a pressure of 1.4 GPa is $T_1 = 20.6$ ms, at a pressure of 2.5 GPa is $T_1 = 15.8$ ms

To measure T_1 , an inversion recovery pulse sequence, defined by a π -pulse followed by a $\frac{\pi}{2}$ -pulse and separated by a variable time τ , was used. The intensity as function of the separation time τ is plotted in Fig. 6.7 over a logarithmic time scale. Identical pulse sequence parameters were used for all measurements at the three pressure values.

All the measurements were done under non-selective excitation conditions see sec. 6.4.3 to allow an standard T_1 evaluation with a single exponent decay fit function.

6.4.6 SHIFTS

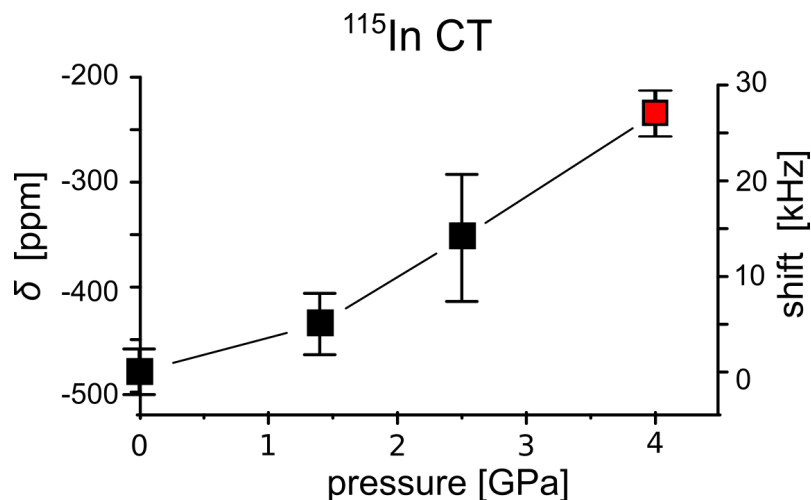


Figure 6.8: **Shifts of AgInTe_2 pressure dependent:** The resonance frequency of the central transition is plotted as a function of pressure. The point at 4GPa is the simulated center frequency of the second order affected central transition simulation of the powdered sample.

Figure 6.8 shows the resonance frequency of the central transition as a function of pressure. One can see a small increase of the shift with increasing pressure. The point at 4 GPa is the calculated center frequency of a second order affected central transition of the powdered sample simulation.

6.5 DISCUSSION

At ambient conditions the material under investigation seems to be a well ordered chalcopyrite structure. The very small field gradient at the indium nuclei can be understood by the almost symmetric surrounding with 4 tellurium atoms (tetrahedron). The secondary neighbors are 4 indium and 8 silver atoms with an average distance of about 450 pm^{105,104}. The additional quadrupolar broadening can be explained by a local distribution of EFG caused by small irregularities or point defects¹³⁴.

Thiti Bovornratanaraks¹⁰⁷ showed in 2010 a detailed structural study with X-ray diffraction on AgInTe₂ up to 6.2 GPa. From ambient to 2.8 GPa a small increase of the reflection spacing is indicated by the XRD patterns. This can be interpreted as a small deformation of the initial chalcopyrite structure, which could increase the quadrupolar interaction strength. An increase is what we find in the spectra and which is proven with nutation spectroscopy experiments.

The phase transition from chalcopyrite to NaCl or *Cmcm* between 3 GPa and 4 GPa is observed by different groups^{78,107}. This is exactly the pressure range where we find something looking like a strong second order affected central transition. Thiti Bovornratanaraks further finds a mixture of both structures at 4.2 GPa. The spectrum (see Fig. 6.6) at 3 GPa appears to show a mixture of both structure types. The narrow peak in the center may represent the rest of the low pressure phase, while the broad resonance line may then be the high pressure phase with a second order quadrupolar broadened CT. Even at 2.5 GPa the first onset of this effect may be seen.

In cell 2 at 4 GPa the peak in the center has almost disappeared. Due to the much better SNR of cell 2 in the higher pressure range a fitting of a second order powder pattern was possible (see sec. 6.4.4). The spectrum at 5 GPa in Fig. 6.6 shows a signal loss. Measurements at 6.4 GPa, 8.2 GPa and 10 GPa in different pressure cells could not find a signal in a broad frequency range. Due to the high unordered high pressure phase without a clear definition of nearest neighbors to the indium nuclei⁷⁸ one could expect a very broad distribution of resonance frequencies which are too broad to resolve in a micro sample in a finite measurement time.

After the pressure was released a signal was found at the same frequencies where the central transition was measured before. The broad foot could not be resolved due to a bad SNR, maybe caused by the large deformation of the coil and the chamber. The visible broadening (≈ 50 kHz) in comparison to the initial line width of this peak could be an indication of the intermediate phase with the sphalerite-type structure which will decay back to the

chalcopyrite structure over time⁷⁸(see sec. 2.2.3).

The T_1 measurements with an decreasing longitudinal relaxation time, if pressure is increased, would fit to the increase of the quadrupolar coupling. However, it is no proof, due to the fact that the inversion of the signal decreases from ambient conditions to 2.5 GPa.

The motivation for these experiments have been to reproduce the measurements of Thomas Meier. He published in 2015⁵ a insulator-to-metal-transition in AgInTe_2 and showed spectra up to 20 GPa. A jump in resonance frequency, in the range of the phase transition around 3 GPa and 5 GPa was found, interpreted as a Knight shift stemming from free carriers (metal). We did not find the signal of the high pressure phase, so our shift data do not show this jump.

Our data show a signal loss above 5 GPa, up to 10 GPa no signal in a broad frequency range was found anymore including the before published frequencies.

*“Not only is the Universe stranger than we think,
it is stranger than we can think.”*

Werner Heisenberg

7

Summary and Outlook

In this chapter a summary of the chapters before is given. The order above is kept, so starting with the sample chamber monitoring, then the investigation of the $\text{YBa}_2\text{Cu}_3\text{O}_{6+y}$ single crystals under pressure followed by the investigation of AgInTe_2 under pressure. Finally an Outlook is given.

7.1 SUMMARY

7.1.1 SAMPLE CHAMBER MONITORING FOR SINGLE CRYSTAL NMR

The fourth chapter describes the technique to measure the height and the diameter insitu, while the cell is closed. An observation of the chambers height reduction was needed to increase the pressure range for single crystal measurements to its limits before the crystal is pressurized uniaxially. Height measurements combined with measurements of the diameter allowed an estimation of the volume and with this a determination of the compressability of the pressure medium paraffin oil.

The height was measured by the compare of the distance between two references at the anvils. As optically clear focusable reference line the edges between two surfaces at the anvil were used. If the orthogonal distance between the reference edges of the two anvils is known the distance between the anvils which is equivalent to the height of the camber can be calculated. The diameter was measured by photos, taken through the anvils with a microscope.

Finally the measured pressure dependence of the height, the diameter and the volume confirmed the theoretical predictions by D.J. Dunstan⁵⁰ in 1989, concerning the pressure dependence of a sample chamber of an anvil cell.

Due to its almost constant height the *thin gasket* regime could act as working regime for single crystal investigations under pressure. The cognizance, that a larger culet increases the range of the thin gasket regime by stabilization of the chamber, is in contrast to the basic idea of the miniaturization of the anvil tips to increase the maximal pressure, if the chamber deformation is one of the limiting factors.

7.1.2 SINGLE CRYSTAL NMR OF $\text{YBa}_2\text{Cu}_3\text{O}_{6+y}$ UP TO 4.4 GPa

The fifth chapter presents the results of the high pressure NMR investigations of differently doped $\text{YBa}_2\text{Cu}_3\text{O}_{6+y}$ single crystals up to 4.4 GPa. Two high pressure NMR anvil cells were prepared. The discussion also considers the results of a previous report by Steven Reichardt⁹.

First, the measurements of the pressure dependence of the critical temperature are shown. The temperature dependent center frequency of the probe head circuit was observed. The inset of the diamagnetic response identifies the superconducting transition. These values are discussed and compared to the literature data.

The next part shows how a YBCO single crystal in an external magnetic field can be aligned by using NMR data and shift measurements. The orientation dependency of the second order shift of the center transition allows, also for weak signals and weak satellite intensities, a determination of the quadrupole frequency.

The quadrupole frequencies allowed the determination of the charges in the CuO_2 -plane pressure dependent. Presented in terms of the $2n_{\text{O}}-n_{\text{Cu}}$ -plane three induced effects were observed by pressure:

- I an increase of the hole doping
- II a favoring increasing of the oxygen hole content over the copper hole content
- III an intra-planar charge redistribution of the holes from copper to oxygen

These effects are differently strong pronounced depending on the initial doping of the single crystal and the pressure. While for lower pressures and for the lower doped sample the doping charges in the CuO_2 -plane effect was much more pronounced. The effect of the redistribution of charges is more dominant for doping levels closer to the optimal doping content and higher pressures.

The intra-planar charge redistribution opens a new way of thinking about pressure effects in high temperature superconductors. This has to be considered in theoretical concepts of the superconductivity in cuprates under pressure in the future.

7.1.3 SILVER-INDIUM-TELLURID NMR UNDER PRESSURE

The sixth chapter presents the results of the NMR investigation of AgInTe_2 powder under pressure. The earlier recorded phase transition^{78,107} was of interest, but was not confirmable by our ^{115}In NMR data.

For pressures below 3 GPa a slightly increase of the quadrupole frequency was observed, which fits to a slightly deformed chalcopyrite structure at low pressures. The increase of the quadrupole frequency was proven by a power dependent nutation spectroscopy experiment. Several NMR anvil cell were prepared and filled with the AgInTe_2 powder, but no signal was found at pressures above 5 GPa in a wide range around the initial lamor frequency at 109.537 MHz.

At pressures between 3 GPa to 5 GPa spectra were recorded which looked like a second order affected central transition of a powder. The spectra would fit to a mixture of a ordered phase, transforming to a strongly disordered high pressure phase.

In all cells no ^{115}In signal was found above 5 GPa up to 10 GPa. After the release of the pressure the signal was found again at the same frequency were ^{115}In was found before at ambient conditions.

The previously reported transition between 3 GPa and 4 GPa, given by literature^{78,107}, was not confirmable by our ^{115}In NMR data. Furthermore the measurements of a spectrum of the high pressure phase and the insulator-metal-transition, identified by an inset of the knight shift, recorded before⁵ were not repeatable.

7.2 CONCLUSION AND OUTLOOK

Different microcoil architectures were prepared by hand. The results for the prototypes were good but a systematic study of these tests could be part of investigations in the future.

A method for the necessary height measurements as well as a method for the measurement of the diameter of the sample chamber of a closed anvil cell are described. The determined compressability of the pressure medium, paraffin oil, fits to the values reported in literature. Further this method enables, by the analysis of the observed basic parameters of the cell architecture, dependent on the pressure, a better understanding how the parameters of the cell behaves under load. Which led to the cognizance, that a larger culet diameter causes a more stable height of the sample chamber and increases the range of the working regime, for single crystal measurements. The stability of the sample chamber especially the observation of the height is essentially important for single crystal NMR. New approaches with $\text{YBa}_2\text{Cu}_3\text{O}_{6+y}$ single crystals in an anvil NMR cell should consider these findings while the cell architecture is planed, to maximize the pressure range of the working regime.

This thesis gives an important contribution to the increase of the reachable pressures with the NMR anvil cell set up which is used by the Haase group at the University of Leipzig. It allowed measurements of $\text{YBa}_2\text{Cu}_3\text{O}_{6+y}$ single crystals up to 4.4 GPa. A prove of a charge redistribution in the CuO_2 -plane induced by pressure is given. This has to be considered by theoretical concepts which try to understand the pressure effects in the CuO_2 -plane of cuprates.

André-Marie Tremblay from the Université de Sherbrooke⁹⁹ confirmed with a three-band Hubbard model with cellular dynamical mean-field theory the observations done by Michal Jurkutat and Damian Rybicki^{97,98} which found an order of cuprates according to their maximal T_c , depending on the oxygen hole content $2n_O$ of the CuO_2 -plane. The redistribution effect of charges in the CuO_2 -plane affected by pressure could be part of models in the future which consider the shrinking of the unit cell.

Danksagung

Während meiner Zeit am 2.Physikalischen Institut der Universität Leipzig hatte ich eine sehr lehrreiche Zeit. Ich konnte viele Erfahrungen mit der technischen Umsetzungen von experimentellen Aufbauten sammeln. Dabei wurde ich mit theoretischen Grundlagen der verschiedensten Themen konfrontiert und musste diese mit Kollegen, diskutieren. Diese Diskussionen waren immer sehr lehrreich und haben mein Verständnis für verschiedene Themen in der Physik weiter vertieft. Die regelmäßigen Vorträge haben stark zu diesem Lerneffekt beigetragen. Dafür möchte ich mich allgemein bedanken.

Speziell möchte ich noch bei den Menschen bedanken ohne die diese Arbeit nicht zustande gekommen wäre:

Zuerst möchte ich meinen Eltern, Beatrix und Herbert Kattinger erwähnen, die mich tatkräftig bei allem unterstützt haben. Sowohl finanziell also auch moralisch stehen sie immer hinter mir und ich möchte mich hiermit dafür Bedanken. Meiner Freundin Melanie danke ich für die Rückendeckung und dein Verständnis während dieser Zeit. Meiner Schwester Miriam danke ich für viele Gespräche und auch für die Unterstützung in anstrengenden Zeiten.

Bei Jürgen Haase möchte ich mich explizit bedanken, da er immer als Ansprechpartner für grundlegende Fragen ob theoretisch oder experimentell zur Verfügung stand, als auch für die Arbeit und die Zeit beim schreiben der Paper und für die Möglichkeit in einem so interessanten Bereich der Physik promovieren zu dürfen.

Für die Hilfe bei experimentellen Aufbauten und für sehr viele sehr lehrreiche Diskussionen möchte ich mich bei Michael Jurkutat bedanken. Unsere Zusammenarbeit war sehr produktiv und hat mir immer sehr viel Spaß gemacht.

Bei Robin Gühne ebenso für viele interessante und lehrreiche Gespräche als auch für seine Expertise beim schreiben von Papern und das genaue Auge für Details.

Darüber hinaus möchte ich mich auch bei allen anderen Mitarbeitern des Instituts bedanken, insbesondere bei Gert Klotzsche für jeglichen technischen Support und bei allen die mich mit Korrekturen, Anmerkungen und Ideen bei der Arbeit unterstütz haben.

Vielen Dank auch an die Promotionskommission für die Zeit und den Aufwand. Und vielen Dank an die Universität Leipzig für die Finanzierung und damit die Möglichkeit für diese Promotion.

“Thanking you once more, I want to wish you the best of luck for your future life and to conclude by saying to you: Dream your dreams and may they come true!”

Felix Bloch



Appendix

A.1 SPECTRA

Y-6.85 CELL

Ambient conditions ^{17}O : $ab \parallel B_0$

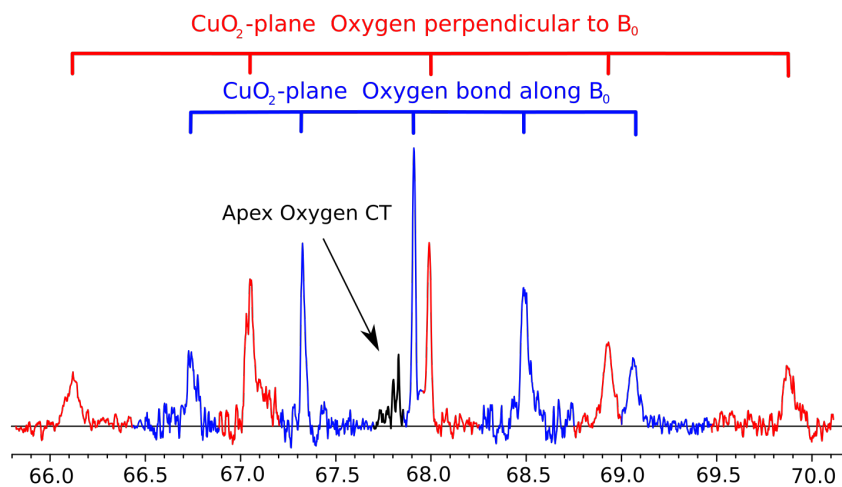


Figure A.1: In this figure the Oxygen spectrum ^{17}O of the Y-6.85 cell, $ab \parallel B_0$ at ambient conditions is shown.

28 kBar ^{17}O : $ab \parallel B_0$

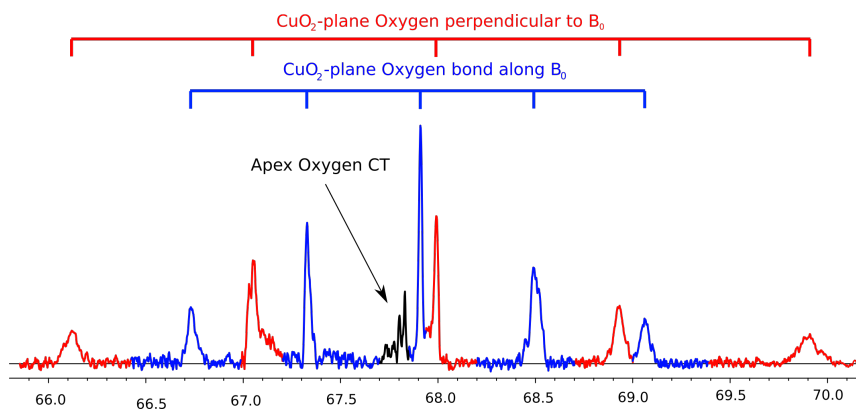


Figure A.2: In this figure the Oxygen spectrum ^{17}O of the Y-6.85 cell, $ab \parallel B_0$ at 28 kBar.

44 kBar ^{17}O : $ab \parallel B_0$

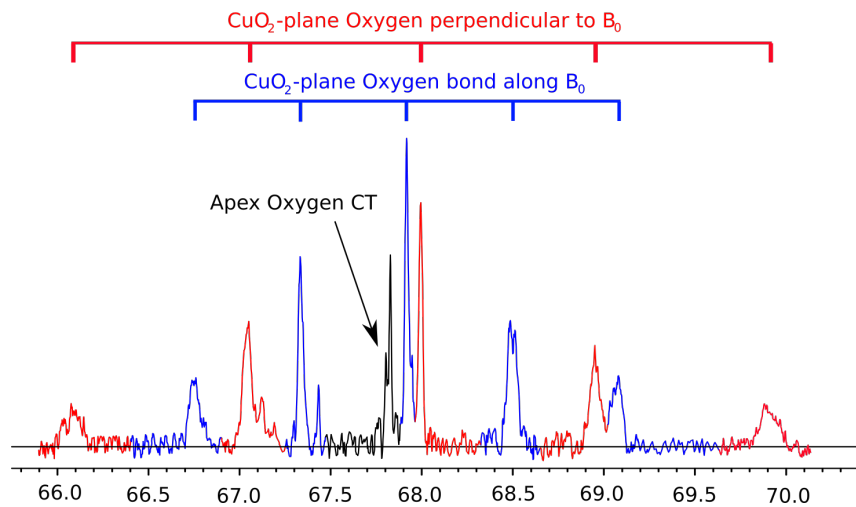


Figure A.3: In this figure the Oxygen spectrum ^{17}O of the Y-6.85 cell, $ab \parallel B_0$ at 44 kBar.

Ambient conditions ^{17}O : $c \parallel B_0$

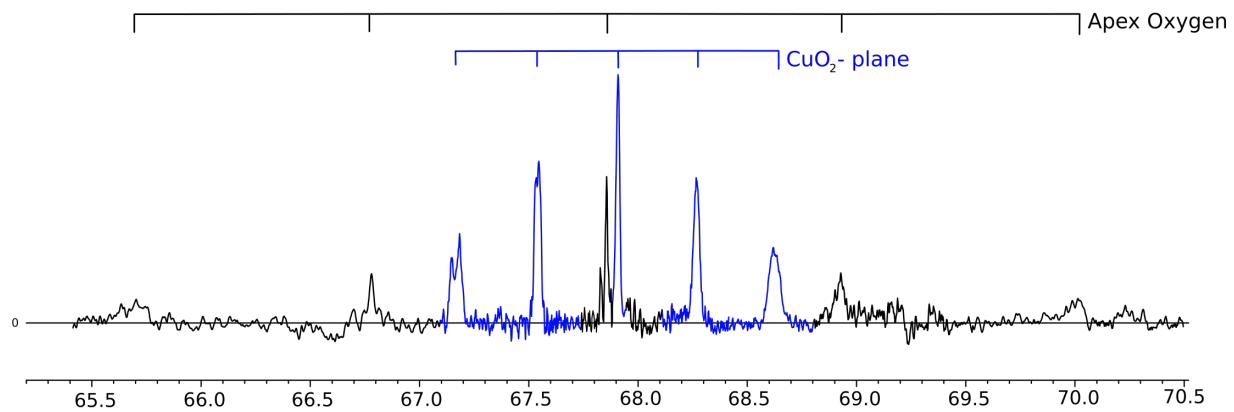


Figure A.4: In this figure the Oxygen spectrum ^{17}O of the Y-6.85 cell, $c \parallel B_0$ at ambient conditions is shown.

28 kBar ^{17}O : $c \parallel B_0$

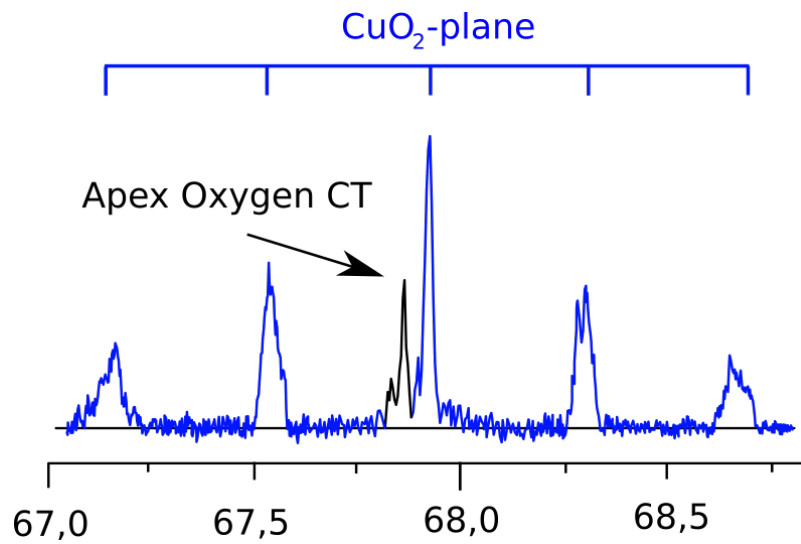


Figure A.5: In this figure the Oxygen spectrum ^{17}O of the Y-6.85 cell, $c \parallel B_0$ at 28 kBar is shown.

44 kBar ^{17}O : $c \parallel B_0$

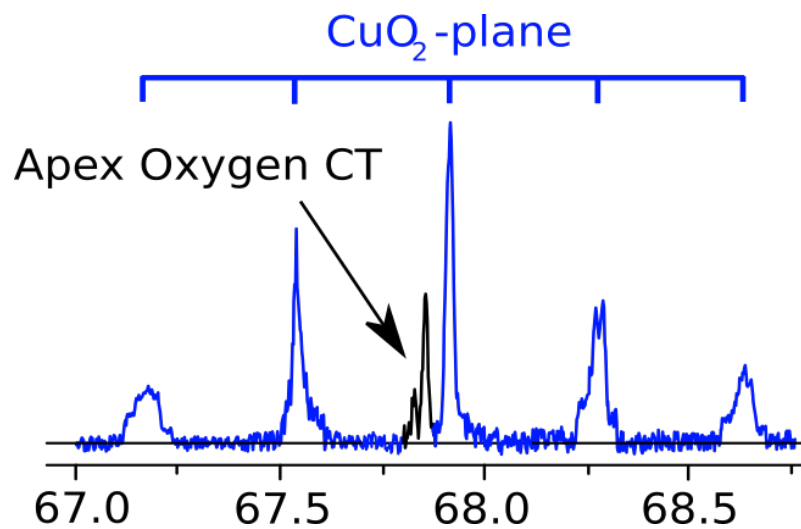


Figure A.6: In this figure the Oxygen spectrum ^{17}O of the Y-6.85 cell, $c \parallel B_0$ at 44 kBar is shown.

Mixed ^{17}O : $c \parallel B_0$, at 300 K and 100 K

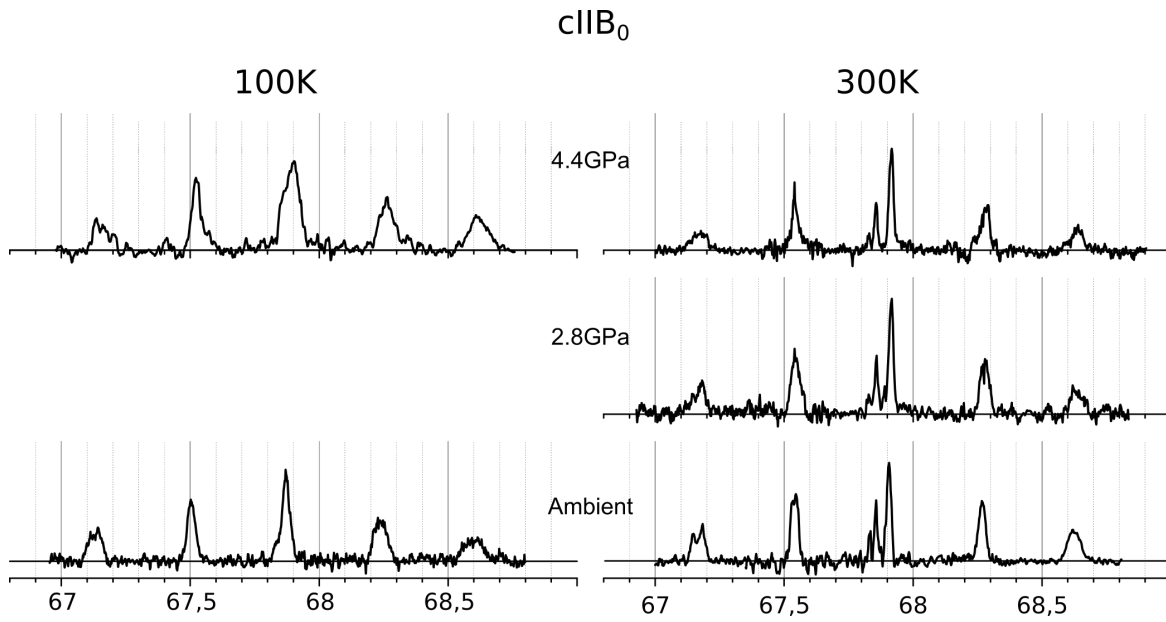


Figure A.7: In this figure the oxygen spectrum ^{17}O of the Y-6.85 cell, at ambient conditions, 28 kBar and 44 kBar for two temperatures is shown.

Mixed ^{63}Cu : $c \parallel B_0$, at 300 K and 100 K

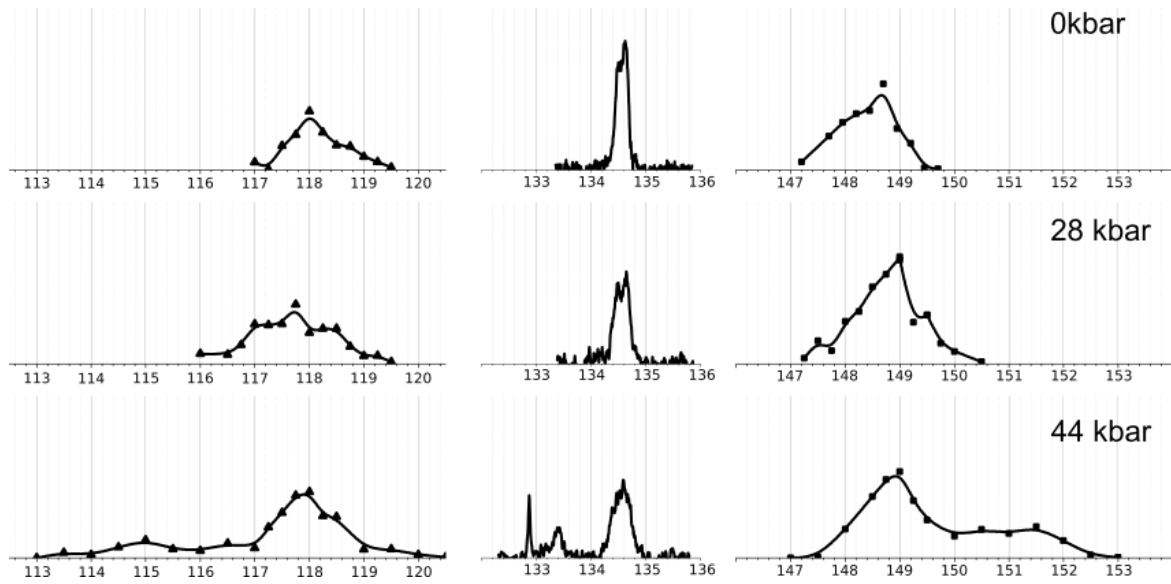


Figure A.8: In this figure the copper spectrum ^{63}Cu of the Y-6.85 cell, at different pressures is shown.

Y-6.5 CELL

Ambient conditions: $c \parallel B_0$

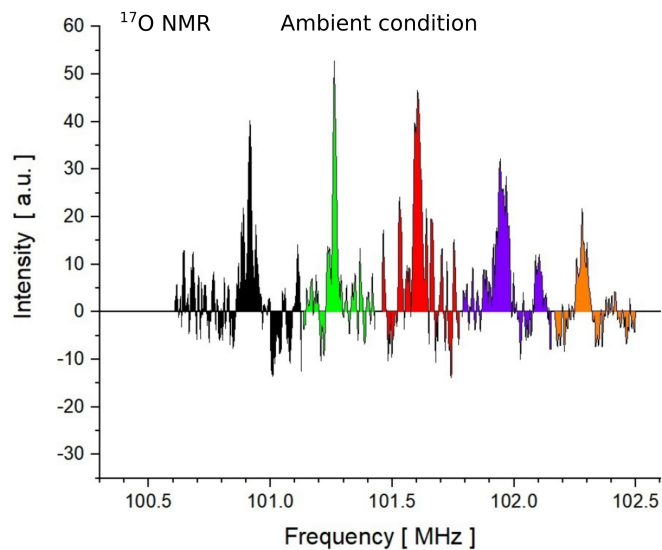


Figure A.9: In this figure the Oxygen spectrum of the of the Y-6.5 cell, $c \parallel B_0$ at ambient conditions is shown. (these data were evaluated by Stefan Tsankov)

40 kBar: $c \parallel B_0$

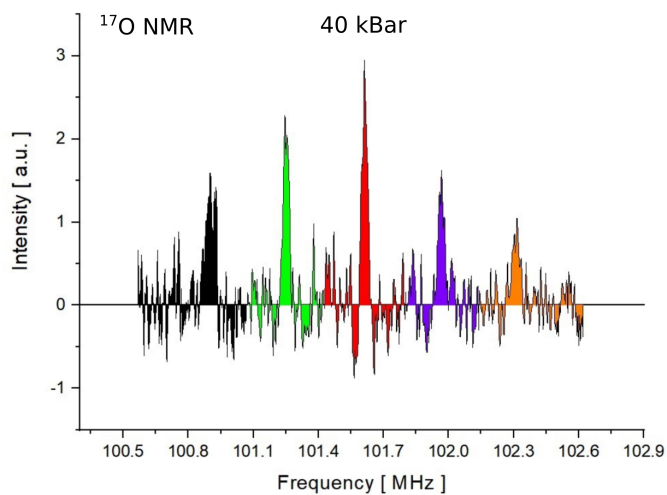


Figure A.10: In this figure the Oxygen spectrum of the Y-6.5 cell, $c \parallel B_0$ at 4 kBar is shown. (these data were evaluated by Stefan Tsankov)

References

- [1] R. Vaughan, C. Lai, and D. Elleman. An Apparatus for Magnetic Measurements at High Pressure. *Rev. Sci. Instrum.*, 42(5):626–629, 1971.
- [2] C.P. Slichter. *Principles of Magnetic Resonance*. Oxford University Press, 1996.
- [3] J. Haase, S. Goh, T. Meissner, P. Alireza, and D. Rybicki. High sensitivity nuclear magnetic resonance probe for anvil cell pressure experiments. *Rev. Sci. Instrum.*, 80(7):073905, 2009.
- [4] T. Meier, T. Herzig, and J. Haase. Moissanite anvil cell design for gigapascal nuclear magnetic resonance. *Rev. Sci. Instrum.*, 85(4):043903, 2014. <https://doi.org/10.1063/1.4870798>.
- [5] T. Meier, S. Reichardt, and J. Haase. High-sensitivity NMR beyond 200,000 atmospheres of pressure. *J. Magn. Reson.*, 257:39–44, 2015. <https://doi.org/10.1016/j.jmr.2015.05.007>.
- [6] S. Reichardt, M. Jurkutat, R. Guehne, J. Kohlrantz, A. Erb, and J. Haase. Bulk charge ordering in the CuO₂ plane of the cuprate superconductor YBa₂Cu₃O_{6.9} by high-pressure NMR. *Condens. Matter*, 3(3):23, 2018.
- [7] J.S. Brooks and J.R. Schrieffer. *Handbook of High-Temperature Superconductivity: Theory and Experiment*. Springer Science & Business Media, 2007.
- [8] J.S. Schilling. High-Pressure Effects. In J R Schrieffer, editor, *Handbook of High-Temperature Superconductivity*. Springer, 2007.
- [9] Steven Reichardt. *Dissertation: Nuclear Magnetic Resonance Study of the Planar Charge Symmetry under Pressure in High-Temperature Superconducting cuprates*. Universität Leipzig, Leipzig, 2018.
- [10] D. Freude and J. Haase. Quadrupole Effects in solid-state Nuclear Magnetic Resonance. In *Special Applications*, pages 1–90. Springer, 1993.
- [11] A. Abragam. *The Principles of Nuclear Magnetism*. Oxford university press, 1983.

- [12] M. L. Martin. E. Fukushima and S. B. W. Roeder. Experimental Pulse NMR: A nuts and bolts approach. Addition-Wesley Publishing Company, Reading, Massachusetts, 1981, 539 + xiv pp. US \$34.50 (hardback). *Organic Magnetic Resonance*, 21(12):770–770, 1983.
- [13] D. Ziessow. R. R. Ernst, G. Bodenhausen u. A. Wokaun: Principles of Nuclear Magnetic Resonance in One and Two Dimensions, Clarendon Press, Oxford 1987. 610 Seiten. *Berichte der Bunsengesellschaft für physikalische Chemie*, 92(12):1563–1565, 1988.
- [14] D. Fenzke, D. Freude, T. Fröhlich, and J. Haase. NMR intensity measurements of half-integer quadrupole nuclei. *Chemical physics letters*, 111(1-2):171–175, 1984.
- [15] Y. Li, A.M. Wolters, P.V. Malawey, J.V. Sweedler, and A.G. Webb. Multiple Solenoidal Microcoil Probes for High-Sensitivity, High-Throughput Nuclear Magnetic Resonance Spectroscopy. *Analytical chemistry*, 71(21):4815–4820, 1999.
- [16] D.A. Seeber, R.L. Cooper, L. Ciobanu, and C.H. Pennington. Design and testing of high sensitivity microreceiver coil apparatus for nuclear magnetic resonance and imaging. *Review of scientific instruments*, 72(4):2171–2179, 2001.
- [17] T. Okuchi, R.J. Hemley, and H. Mao. Radio frequency probe with improved sensitivity for diamond anvil cell nuclear magnetic resonance. *Rev. Sci. Instrum.* 76, 026111, 2005.
- [18] H. Meinke and F.-W. Gundlach. *Taschenbuch der Hochfrequenztechnik*. Springer-Verlag, 2013.
- [19] H. Nyquist. Thermal agitation of electric charge in conductors. *Physical review*, 32(1):110, 1928.
- [20] J.B. Johnson. Thermal agitation of electricity in conductors. *Physical review*, 32(1):97, 1928.
- [21] J. Mispelter, M. Lupu, and A. Briguet. *NMR probeheads for biophysical and biomedical experiments: theoretical principles and practical guidelines*. World Scientific Publishing Company, 2015.
- [22] W. Grochala, R. Hoffmann, J.i Feng, and N. W. Ashcroft. The chemical imagination at work in very tight places. *Angewandte Chemie International Edition*, 46(20):3620–3642, 2007.

- [23] P.W. Bridgman. *Physics of High Pressure*. Oxford university press, 1952.
- [24] K. Edalati and Z. Horita. A review on high-pressure torsion (hpt) from 1935 to 1988. *Materials Science and Engineering: A*, 652:325–352, 2016.
- [25] C.E. Weir, E.R. Lippincott, A. Van Valkenburg, and E.N. Bunting. Infrared Studies in the 1- to 15-Micron Region to 30,000 Atmospheres. *Journal of research of the National Bureau of Standards. Section A, Physics and chemistry*, 63A(1):55–62, 1959.
- [26] G.J. Piermarini. Alvin Van Valkenburg and the Diamond Anvil Cell. *High Pressure Research*, 11(5):279–284, 1993.
- [27] W.A. Bassett. High Pressure Res 29. *CP5-186*, 2009.
- [28] H.K. Mao, P.M. Bell, and R.J. Hemley. Ultrahigh pressures: Optical observations and Raman measurements of hydrogen and deuterium to 1.47 Mbar. *Phys. Rev. Lett.*, 55:99–102, Jul 1985.
- [29] R.M. Hazen. *The new alchemists: Breaking through the barriers of high pressure*. Crown, 1993.
- [30] P. M. Bell, J. A. Xu, and H. K. Mao. Static Compression of Gold and Copper and Calibration of the Ruby Pressure Scale to Pressures to 1.8 Megabars. In *Shock Waves in Condensed Matter. Springer US*, pages 125–130, 1986.
- [31] R.A. Forman, G.J. Piermarini, J.D. Barnett, and S. Block. Pressure measurement made by the utilization of ruby sharp-line luminescence. *Science*, 176(4032):284–285, 1972.
- [32] J.D. Barnett, S. Block, and G.J. Piermarini. An Optical Fluorescence System for Quantitative Pressure Measurement in the Diamond-Anvil Cell. *Review of Scientific Instruments*, 44(1):1–9, 1973.
- [33] I.F. Silvera, A.D. Chijioke, W. J. Nellis, A. Soldatov, and J. Tempere. Calibration of the ruby pressure scale to 150 GPa. *physica status solidi (b)*, 244(1):460–467, 2007.
- [34] K.A. Goettel, H. Mao, and P.M. Bell. Generation of static pressures above 2.5 megabars in a diamond-anvil pressure cell. *Review of scientific instruments*, 56(7):1420–1427, 1985.

- [35] W.C. Moss and K.A. Goettel. Finite element design of diamond anvils. *Applied Physics Letters*, 50(1):25–27, 1987.
- [36] L. Dubrovinsky, N. Dubrovinskaia, E. Bykova, M. Bykov, V. Prakapenka, C. Prescher, K. Glazyrin, H.-P. Liermann, M. Hanfland, M. Ekholm, Q. Feng, L. V. Pourovskii, M. I. Katsnelson, J. M. Wills, and I. A. Abrikosov. The most incompressible metal Osmium at static pressures above 750 Gigapascals. *Nature*, 338-8570(5):226–229, Sept 1 2015.
- [37] A.P. Drozdov, P.P. Kong, V.S. Minkov, S.P. Besedin, M.A. Kuzovnikov, S. Mozaffari, L. Balicas, F.F. Balakirev, D.E. Graf, and V.B. Prakapenka. Superconductivity at 250 K in lanthanum hydride under high pressures. *Nature*, 569(7757):528–531, May 2019.
- [38] A. Jayaraman. Ultrahigh pressures. *Reviews of Scientific Instruments*. 57, jan 1986.
- [39] M. Eremets. *High Pressure Experimental Methods*. Oxford University Press, 1996.
- [40] R.A. Forman, G.J. Piermarini, J.D. Barnett, and S. Block. Pressure measurement made by the utilization of ruby sharp-line luminescence. *Science*, 176(4032):284–285, 1972.
- [41] P. M. Mao, H. K. and Bell, J. W. Shaner, and D. J. Steinberg. Specific volume measurements of Cu, Mo, Pd, and Ag and calibration of the ruby R1 fluorescence pressure gauge from 0.06 to 1 Mbar. *Journal of Applied Physics*, 1978.
- [42] K. Kitagawai, H. Gotoui, T. Yagil, A. Yamadai, T. Matsumoto, Y. Uwatoko, and M. Takigawa. Space Efficient Opposed-Anvil High-Pressure Cell and Its Application to Optical and NMR Measurements up to 9 GPa. *The Physical Society of Japan (JPS)*, 338-8570, Jan 25 2010.
- [43] P. Alireza and S. Julian. Susceptibility measurements at high pressures using a microcoil system in an anvil cell. *Rev. Sci. Instrum.*, 74(11):4728–4731, 2003.
- [44] Thomas Meier. *Dissertation: High Sensitivity Nuclear Magnetic Resonance at Extreme Pressures*. Universität Leipzig, Leipzig, 2016.
- [45] T. Meier and J. Haase. High-Sensitivity Nuclear Magnetic Resonance at Gigapascal Pressures: A New Tool for Probing Electronic and Chemical Properties of Condensed Matter under Extreme Conditions. *JoVE*, pages 1940–087X, 2014. <https://doi.org/10.3791/52243>.

- [46] Almax-EasyLab. Moissanite (6H-SiC). <https://www.almax-easylab.com/WebSiteMoissaniteStandardDesign03REV01.aspx>. [Online; accessed September-2021].
- [47] Materion-Brush-Ltd. Alloy 25 data sheet, 2013.
- [48] Materion-Brush-Ltd. Magnetic Properties of Copper Beryllium, 2011.
- [49] RMI. Titanium Alloy Guide, 2011.
- [50] D. J. Dunstan. Theory of the gasket in diamond anvil high-pressure cells. *Review of Scientific Instruments* 60, Jan 1989.
- [51] N. Tateiwa and Y. Haga. Evaluations of pressure-transmitting media for cryogenic experiments with diamond anvil cell. *Review of Scientific Instruments*, dec 2009.
- [52] N. Tateiwa and Y. Haga. Appropriate pressure-transmitting media for cryogenic experiment in the diamond anvil cell up to 10 GPa. *Journal of Physics: Conference Series*, mar 2010.
- [53] J. W. Otto, J. K. Vassiliou, and G. Frommeyer. Nonhydrostatic compression of elastically anisotropic polycrystals. I. Hydrostatic limits of 4:1 methanol-ethanol and paraffin oil. *Phys. Rev. B* 57, 1998.
- [54] D. Will, N. Gebhardt, R. Nollau, D. Herschel, and H. Ströhl. *Druckflüssigkeiten*. Springer Berlin Heidelberg, Berlin, Heidelberg, 2011.
- [55] R.J. Hemley, C.S. Zha, A.P. Jephcoat, H.K. Mao, L.W. Finger, and D.E. Cox. X-ray diffraction and equation of state of solid neon to 110 GPa. *Physical Review B*, 1989.
- [56] J. Yen and M. Nicol. Temperature dependence of the ruby luminescence method for measuring high pressures. *Journal of Applied Physics*, 72(12):5535–5538, 1992.
- [57] A. Podlesnyak, M. Loguillo, G. M. Rucker, B. Haberl, R. Boehler, G. Ehlers, L.L. Daemen, D. Armitage, M.D. Frontzek, and M. Lumsden. Clamp cell with in situ pressure monitoring for low-temperature neutron scattering measurements. *High Pressure Research*, 38(4):482–492, 2018.
- [58] S. Lee, K. Luszczynski, R.E. Norberg, and M. S. Conradi. Nmr in a diamond anvil cell. *Review of scientific instruments*, 58(3):415–417, 1987.

- [59] S. Lee, M. S. Conradi, and R.E. Norberg. Molecular motion in solid H_2 at high pressures. *Physical Review B*, 40(18):12492, 1989.
- [60] S. Lee, M. S. Conradi, and R.E. Norberg. Improved nmr resonator for diamond anvil cells. *Review of scientific instruments*, 63(7):3674–3676, 1992.
- [61] M.S. Conradi. Conradi, mark s.: Evolution of nmr hardware. *eMagRes*, 2007.
- [62] Y. Uwatoko, S. Todo, K. Ueda, A. Uchida, M. Kosaka, N. Mori, and T. Matsumoto. Material properties of Ni–Cr–Al alloy and design of a 4 GPa class non-magnetic high-pressure cell. *Journal of Physics: Condensed Matter*, 14(44):11291, 2002.
- [63] N. Yamatoji, H. Fukazawa, H. Taira, Y. Kohori, C. Terakura, N. Takeshita, H. Takagi, and Y. Tokura. High Pressure ^{63}Cu Nuclear Quadrupole Resonance Measurements in Cu_2O up to 10 GPa Using Modified Bridgman Anvil Cell. *Journal of the Physical Society of Japan*, 76(Suppl. A):114–115, 2007.
- [64] H. Fukazawa, N. Yamatoji, Y. Kohori, C. Terakura, N. Takeshita, Y. Tokura, and H. Takagi. Manometer extension for high pressure measurement: Nuclear quadrupole resonance study of Cu_2O with a modified Bridgman anvil cell up to 10 GPa. *Review of scientific instruments*, 78(1):015106, 2007.
- [65] M.G. Pravica and I.F. Silvera. Nuclear magnetic resonance in a diamond anvil cell at very high pressures. *Review of Scientific Instruments*, 69(2):479–484, 1998.
- [66] S.H. Lee, K. Luszczynski, R.E. Norberg, and M.S. Conradi. NMR in a Diamond Anvil Cell. *Review of Scientific Instruments*, 58(3):415–417, 1987.
- [67] R. Bertani, M. Mali, J. Roos, and D. Brinkmann. A diamond anvil cell for high-pressure NMR investigations. *Review of scientific instruments*, 63(6):3303–3306, 1992.
- [68] J.L. Yarger, R.A. Nieman, G.H. Wolf, and R.F. Marzke. High-pressure ^1H and ^{13}C nuclear magnetic resonance in a diamond anvil cell. *Journal of Magnetic Resonance, Series A*, 114(2):255–257, 1995.
- [69] S.K. Goh, P.L. Alireza, P.D.A. Mann, A.-M. Cumberlidge, C. Bergemann, M. Sutherland, and Y. Maeno. High pressure de Haas–van Alphen studies of Sr_2RuO_4 using an anvil cell. *Current Applied Physics*, 8(3-4):304–307, 2008.

- [70] T. Suzuki, I. Yamauchi, Y. Shimizu, M. Itoh, N. Takeshita, C. Terakura, H. Takagi, Y. Tokura, T. Yamauchi, and Y. Ueda. High-pressure V-51 NMR study of the magnetic phase diagram and metal-insulator transition in quasi-one-dimensional beta-Na₀. *Phys. Rev. B* **79**, 33V2O5, 2009.
- [71] K. Kitagawa, H. Gotou, T. Yagi, A. Yamada, T. Matsumoto, Y. Uwatoko, and M. Takigawa. Space efficient opposed-anvil high-pressure cell and its application to optical and NMR measurements up to 9 GPa. *Journal of the Physical Society of Japan*, 79(2):024001, 2010.
- [72] K. Kitagawa, Y. Mezaki, K. Matsubayashi, Y. Uwatoko, and M. Takigawa. Phase diagram and superconductivity of NaFeAs studied by single-crystal ⁷⁵As-NMR under pressure up to 7.3 GPa. *The Physical Society of Japan (JPS)*, page 015031, 2014.
- [73] T. Meier and J. Haase. Anvil cell gasket design for high pressure nuclear magnetic resonance experiments beyond 30 GPa. *Rev. Sci. Instrum.*, 86(12):123906, 2015.
- [74] T. Meier, N. Wang, D. Mager, J.G. Korvink, S. Petitgirard, and L. Dubrovinsky. Magnetic flux tailoring through Lenz lenses for ultrasmall samples: A new pathway to high-pressure nuclear magnetic resonance. *Science advances*, 3(12), 2017.
- [75] J. Schoenmaker, K.R. Pirota, and J.C. Teixeira. Magnetic flux amplification by Lenz lenses. *Review of Scientific Instruments*, 84(8):085120, 2013.
- [76] N. Spengler, P.T. While, M.V. Meissner, U. Wallrabe, and J.G. Korvink. Magnetic Lenz lenses increase the limit-of-detection in nuclear magnetic resonance. *arXiv preprint arXiv:1606.07044*, 2016.
- [77] T. Meissner, S.K. Goh, J. Haase, M. Richter, K. Koepf, and H. Eschrig. Nuclear magnetic resonance at up to 10.1 gpa pressure detects an electronic topological transition in aluminum metal. *Journal of Physics: Condensed Matter*, 26(1):015501, 2013.
- [78] K.-J. Range, G. Engert, and A. Weiss. High pressure transformations of ternary chalcogenides with chalcopyrite structure—I. Indium-containing compounds. *Solid State Communications*, 7(24):1749–1752, 1969.
- [79] K. Bednorz and J. Mueller. Possible high temperature superconductivity in Ba-LaCuO. *Z. Phys*, 64:189, 1986.

- [80] J. G. Bednorz and K. A. Müller. Perovskite-type oxides—the new approach to high- T_c superconductivity. nobel lecture. *Angewandte Chemie International Edition in English*, 27(5):735–748, 1988.
- [81] M.K. Wu, J.R. Ashburn, C.J. Torng, P.H. Hor, R.L. Meng, L. Gao, Z.J. Huang, Y.Q. Wang, and C.W. Chu. Superconductivity at 93 K in a new mixed-phase Y-Ba-Cu-O compound system at ambient pressure. *Phys. Rev. Lett.*, 58:908–910, Mar 1987.
- [82] C.W. Chu. Cuprates-Superconductors with a T_c up to 164 K. In *100 Years of Superconductivity*, pages 244–255. CRC Press, 2011.
- [83] L.N. Cooper and D. Feldman. *BCS: 50 years*. World scientific, 2010.
- [84] J. Haase, O.P. Sushkov, P. Horsch, and G.V.M. Williams. Planar Cu and O hole densities in high- T_c cuprates determined with NMR. *Physical Review B*, 69(9):094504, 2004.
- [85] A. Williams, G.H. Kwei, R.B. Von Dreele, I.D. Raistrick, and D.L. Bish. Joint X-ray and neutron refinement of the structure of superconducting $\text{YBa}_2\text{Cu}_3\text{O}_{7-x}$: Precision structure, anisotropic thermal parameters, strain, and cation disorder. *Phys. Rev. B*, 37:7960–7962, May 1988.
- [86] C.P. Slichter. Magnetic Resonance Studies of High Temperature Superconductors. In J R Schrieffer and James S Brooks, editors, *Handbook of High-Temperature Superconductivity*, pages 215–256. Springer, New York, 2007.
- [87] Bruker. Bruker NMR Table. https://kodu.ut.ee/~laurit/AK2/NMR_tables_Bruker2012.pdf. [Online; accessed September-2021].
- [88] P.I. Djurovich and R.J. Watts. A simple and reliable chemical preparation of $\text{YBa}_2\text{Cu}_3\text{O}_{7-x}$ superconductors: An experiment in high temperature superconductivity for an advanced undergraduate laboratory. *Journal of chemical education*, 70(6):497, 1993.
- [89] A. Erb, E. Walker, and R. Flükiger. The use of BaZrO_3 crucibles in crystal growth of the high- T_c superconductors Progress in crystal growth as well as in sample quality. *Physica C: Superconductivity*, 258(1-2):9–20, 1996.
- [90] C.C. Homes, T. Timusk, R. Liang, D.A. Bonn, and W.N. Hardy. Optical conductivity of c axis oriented $\text{YBa}_2\text{Cu}_3\text{O}_{6.70}$: Evidence for a pseudogap. *Physical review letters*, 71(10):1645, 1993.

- [91] C.V. Parker, P. Aynajian, E.H. da Silva Neto, A. Pushp, S. Ono, J. Wen, Z. Xu, G. Gu, and A. Yazdani. Fluctuating stripes at the onset of the pseudogap in the high- T_c superconductor $\text{Bi}_2\text{Sr}_2\text{CaCu}_2\text{O}_{8+x}$. *Nature*, 468(7324):677–680, Dec 2010.
- [92] J.M. Tranquada, B.J. Sternlieb, J.D. Axe, Y. Nakamura, and S. Uchida. Evidence for stripe correlations of spins and holes in copper oxide superconductors. *Nature*, 375(6532):561–563, Jun 1995.
- [93] T. Meissner, S. Goh, J. Haase, G. Williams, and P. Littlewood. High-pressure spin shifts in the pseudogap regime of superconducting $\text{YBa}_2\text{Cu}_4\text{O}_8$ as revealed by ^{17}O NMR. *Phys. Rev. B*, 83:220517, Jun 2011. <https://link.aps.org/doi/10.1103/PhysRevB.83.220517>.
- [94] J.S. Schilling and S. Klotz. The influence of high pressure on the superconducting and normal properties of high temperature superconductors. In *Physical Properties of High Temperature Superconductors III*, pages 59–158. World Scientific Singapore, 1992.
- [95] S. Sadewasser, J.S. Schilling, A.P. Paulikas, and B.W. Veal. Pressure dependence of T_c to 17 GPa with and without relaxation effects in superconducting $\text{YBa}_2\text{Cu}_3\text{O}_x$. *Physical Review B*, 61(1):741, 2000.
- [96] C. Murayama, Y. Iye, T. Enomoto, N. Mori, Y. Yamada, T. Matsumoto, Y. Kubo, Y. Shimakawa, and T. Manako. Correlation between the pressure-induced changes in the Hall coefficient and T_c in superconducting cuprates. *Physica C: Superconductivity*, 183(4-6):277–285, 1991.
- [97] M. Jurkutat, D. Rybicki, O.P. Sushkov, G.V.M. Williams, A. Erb, and J. Haase. Distribution of electrons and holes in cuprate superconductors as determined from ^{17}O and ^{63}Cu nuclear magnetic resonance. *Phys. Rev. B*, 90:140504, Oct 2014.
- [98] D. Rybicki, M. Jurkutat, S. Reichardt, C. Kapusta, and J. Haase. Perspective on the phase diagram of cuprate high-temperature superconductors. *Nature Communications*, 7(1):11413, May 2016.
- [99] N. Kowalski, S.S. Dash, P. Sémon, D. Sénéchal, and A.-M. Tremblay. Oxygen hole content, charge-transfer gap, covalency, and cuprate superconductivity. *Proceedings of the National Academy of Sciences*, 118(40), 2021.

- [100] Thomas Meißner. *Dissertation: Exploring Nuclear Magnetic Resonance at the Highest Pressures*. Universität Leipzig, Leipzig, 2013.
- [101] I. Vinograd, R. Zhou, H. Mayaffre, S. Krämer, R. Liang, W.N. Hardy, D.A. Bonn, and M.-H. Julien. Nuclear magnetic resonance study of charge density waves under hydrostatic pressure in $\text{YBa}_2\text{Cu}_3\text{O}_y$. *Phys. Rev. B*, 100:094502, Sep 2019.
- [102] T. Schröder, T. Rosenthal, D. Souchay, C. Petermayer, S. Grott, E.-W. Scheidt, C. Gold, W. Scherer, and O. Oeckler. 2.4 Å high-pressure route to thermoelectrics with low thermal conductivity: the solid solution series $\text{AgIn}_x\text{Sb}_{1-x}\text{Te}_2$. *Synthesis, thermal behavior and thermoelectric properties of disordered tellurides with structures derived from the rocksalt type*, 206:20–26, 2014.
- [103] M.N. Schneider, T. Rosenthal, C. Stiewe, and O. Oeckler. From phase-change materials to thermoelectrics? *Oldenbourg Wissenschaftsverlag*, 2010.
- [104] Y. Aikebaier, K. Kurosaki, T. Sugahara, Y. Ohishi, H. Muta, and S. Yamanaka. High-temperature thermoelectric properties of non-stoichiometric $\text{Ag}_{1-x}\text{InTe}_2$ with chalcopyrite structure. *Materials Science and Engineering: B*, 177(12):999–1002, 2012.
- [105] S. Welzmler, F. Hennersdorf, A. Fitch, and O. Oeckler. Solid Solution Series between CdIn_2Te_4 and AgInTe_2 Investigated by Resonant X-ray Scattering. *Zeitschrift für anorganische und allgemeine Chemie*, 640(15):3135–3142, 2014.
- [106] S. Welzmler, F. Hennersdorf, R. Schlegel, A. Fitch, G. Wagner, and O. Oeckler. Silver Indium Telluride Semiconductors and Their Solid Solutions with Cadmium Indium Telluride: Structure and Physical Properties. *Inorganic chemistry*, 54(12):5745–5756, 2015.
- [107] T. Bovornratanaraks, K. Kotmool, K. Yoodee, M.I. McMahon, and D. Ruffolo. High pressure structural studies of AgInTe_2 . In *Journal of Physics: Conference Series*, volume 215, page 012008. IOP Publishing, 2010.
- [108] K. Kotmool, T. Bovornratanaraks, and K. Yoodee. Ab initio study of structural phase transformations and band gap of chalcopyrite phase in AgInTe_2 under high pressure. *Solid State Communications*, 220:25–30, 2015.

- [109] C. Kattinger, R. Guehne, S. Tsankov, M. Jurkutat, A. Erb, and J. Haase. Moissanite anvil cell single crystal nmr at pressures of up to 4.4 gpa. *Review of Scientific Instruments*, 92(11):113901, 2021.
- [110] Y.A. Timofeev and A.N. Utyuzh. Measuring the thickness of a metal gasket squeezed between the anvils of a high-pressure cell while preparing it for an experiment. *Instruments and Experimental Techniques*, 46(5):721–723, 2003.
- [111] M. Li, C. Gao, G. Peng, C. He, A. Hao, X. Huang, D. Zhang, C. Yu, Y. Ma, and G. Zou. Thickness measurement of sample in diamond anvil cell. *Review of Scientific Instruments*, 78(7):075106, 2007.
- [112] L.N. Dzhavadov and F.S. Elkin. Determination of the thickness of a gasket in a diamond anvil high-pressure cell. *Instruments and Experimental Techniques*, 55(1):116–119, 2012.
- [113] B. Li, C. Ji, W. Yang, J. Wang, K. Yang, R. Xu, W. Liu, Z. Cai, J. Chen, and H. Mao. Diamond anvil cell behavior up to 4 Mbar. *Proceedings of the National Academy of Sciences*, 115(8):1713–1717, 2018.
- [114] M. Jurkutat, C. Kattinger, S. Tsankov, R. Reznicek, A. Erb, and J. Haase. How pressure enhances the critical temperature for high temperature superconductivity in $\text{YBa}_2\text{Cu}_3\text{O}_{6+y}$. *arXiv cond-mat.supr-con*, 2021.
- [115] T.Z. Nakano, K. Miura, and A. Ohnishi. Chiral and deconfinement transitions in strong coupling lattice QCD with finite coupling and Polyakov loop effects. *Physical Review D*, 83(1):016014, 2011.
- [116] T. Machi, M. Kosuge, N. Koshizuka, and H. Yasuoka. NQR study in $\text{YBa}_2\text{Cu}_4\text{O}_8$ under high pressure. *Journal of Magnetism and Magnetic Materials*, 177, 1998.
- [117] K. Kitagawa, N. Katayama, H. Gotou, T. Yagi, K. Ohgushi, T. Matsumoto, Y. Uwatoko, and M. Takigawa. Spontaneous formation of a superconducting and antiferromagnetic hybrid state in SrFe_2As_2 under high pressure. *Physical review letters*, 103(25):257002, 2009.
- [118] D. Brinkmann. Comparing Y- Ba- Cu- O superconductors by Cu, O and Ba NMR/NQR. *Applied Magnetic Resonance*, 3(3):483–494, 1992.
- [119] J.R. Schrieffer. *Handbook of High-Temperature Superconductivity*. Springer, 2007.

- [120] I. Vinograd, R. Zhou, H. Mayaffre, S. Krämer, R. Liang, W.N. Hardy, D.A. Bonn, and M.H. Julien. Nuclear magnetic resonance study of charge density waves under hydrostatic pressure in $\text{YBa}_2\text{Cu}_3\text{O}_y$. *Physical Review B*, 100(9):094502, 2019.
- [121] R.J. Wijngaarden, D.T. Jover, and R. Griessen. Intrinsic and carrier density effects on the pressure dependence of T_c of high-temperature superconductors. *Physica B: Condensed Matter*, 265(1-4):128–135, 1999.
- [122] C. Ambrosch-Draxl, E.Y. Sherman, H. Auer, and T. Thonhauser. Pressure-induced hole doping of the Hg-based cuprate superconductors. *Physical review letters*, 92(18):187004, 2004.
- [123] P.L. Alireza, G.H. Zhang, W. Guo, J. Porras, T. Loew, Y.-T. Hsu, G.G. Lonzarich, M. Le Tacon, B. Keimer, and S.E. Suchitra. Accessing the entire overdoped regime in pristine $\text{YBa}_2\text{Cu}_3\text{O}_{6+x}$ by application of pressure. *Physical Review B*, 95(10):100505, 2017.
- [124] O. Cyr-Choinière, D. LeBoeuf, S. Badoux, S. Dufour-Beauséjour, D.A. Bonn, W.N. Hardy, R. Liang, D. Graf, N. Doiron-Leyraud, and L. Taillefer. Sensitivity of T_c to pressure and magnetic field in the cuprate superconductor $\text{YBa}_2\text{Cu}_3\text{O}_y$: Evidence of charge-order suppression by pressure. *Physical Review B*, 98(6):064513, 2018.
- [125] L. Deng, Y. Zheng, Z. Wu, S. Huyan, H.-C. Wu, Y. Nie, K. Cho, and C.-W. Chu. Higher superconducting transition temperature by breaking the universal pressure relation. *Proceedings of the National Academy of Sciences*, 116(6):2004–2008, 2019.
- [126] C. Weber, C. Yee, K. Haule, and G. Kotliar. Scaling of the transition temperature of hole-doped cuprate superconductors with the charge-transfer energy. *EPL (Europhysics Letters)*, 100(3):37001, 2012.
- [127] C. Weber. What controls the critical temperature of high temperature copper oxide superconductors: insights from scanning tunnelling microscopy. *Science Bulletin*, 62(2):102–104, 2017.
- [128] W. Ruan, C. Hu, J. Zhao, P. Cai, Y. Peng, C. Ye, R. Yu, X. Li, Z. Hao, C. Jin, et al. Relationship between the parent charge transfer gap and maximum transition temperature in cuprates. *Science bulletin*, 61(23):1826–1832, 2016.

- [129] S. Sadewasser, J.S. Schilling, J.L. Wagner, O. Chmaissem, J.D. Jorgensen, D.G. Hinks, and B. Dabrowski. Relaxation effects in the transition temperature of superconducting $\text{HgBa}_2\text{CuO}_{4+\delta}$. *Physical Review B*, 60(13):9827, 1999.
- [130] I. Bozovic, G. Logvenov, I. Belca, B. Narimbetov, and I. Sveklo. Epitaxial strain and superconductivity in $\text{La}_2\text{SrCuO}_4$ thin films. *Physical review letters*, 89(10):107001, 2002.
- [131] R. Guehne, C. Kattinger, M. Bertmer, S. Welzmler, O. Oeckler, and J. Haase. Nmr study of AgInTe_2 at normal and high pressures. *The Journal of Physical Chemistry C*, 2022.
- [132] C. Goupil. *Continuum theory and Modeling of Thermoelectric Elements*. John Wiley & Sons, 2015.
- [133] R. Guehne, C. Kattinger, M. Bertmer, S. Welzmler, O Oeckler, and J. Haase. NMR study of AgInTe_2 at normal and high pressure. *arXiv cond-mat.*, 2022.
- [134] O.H. Han, H.K.C. Timken, and E. Oldfield. Solid-state "magic-angle" sample-spinning nuclear magnetic resonance spectroscopic study of group III–V (13–15) semiconductors. *The Journal of chemical physics*, 89(10):6046–6052, 1988.



INFORMATIONS ABOUT THE DOCUMENT :
this PhD thesis was written by
Carsten Kattinger at the University
of Leipzig in Saxony, Germany in the
time from the 01.08.2018 - 31.10.21